ABSTRACT

Title of dissertation: MULTIVARIATE ERROR COVARIANCE ESTIMATES BY MONTE-CARLO SIMULATION FOR OCEANOGRAPHIC ASSIMILATION STUDIES

Anna Borovikov, Doctor of Philosophy, 2005

Dissertation directed by: Dr. Michele Rienecker
NASA/Goddard

Professor James Carton
Department of Meteorology

One of the most difficult aspects of ocean state estimation is the prescription of the model forecast error covariances. Simple covariances are usually prescribed, rarely are cross-covariances between different model variables used. A multivariate model of the forecast error covariance is developed for an Optimal Interpolation (OI) assimilation scheme (MvOI) and compared to simpler Gaussian univariate model (UOI).

For the MvOI an estimate of the forecast error statistics is made by Monte Carlo techniques from an ensemble of model forecasts. An important advantage of using an ensemble of ocean states is that it provides a natural way to estimate cross-covariances between the fields of different physical variables constituting the model state vector, at the same time incorporating the model's dynamical and thermodynamical constraints. The robustness of the error covariance estimates as well as the analyses has been established by comparing multiple populations of the ensemble.

Temperature observations from the Tropical Atmosphere-Ocean (TAO) array have been assimilated in this study. Data assimilation experiments are validated with a large independent set of subsurface observations of salinity, zonal velocity and temperature. The performance of the UOI and MvOI is similar in temperature. The salinity and velocity fields are greatly improved in the MvOI, as evident from the analyses of the rms differences between these fields and independent observations. The MvOI assimilation is found to improve upon the control (no assimilation) run in generating water masses with properties close to those observed, while the UOI fails to maintain

the temperature-salinity relationship.

The feasibility of representing a reduced error subspace through empirical orthogonal functions (EOFs) is discussed and a method proposed to substitute the local noise-like variability by a simple model. While computationally efficient, this method produces results only slightly inferior to the MvOI with the full set of EOFs.

An assimilation scheme with a multivariate forecast error model has the capability to simultaneously process observations of different types. This was tested using temperature data and synthetic salinity observations. The resulting subsurface structures both in temperature and salinity are the closest to the observed, while the currents structure is maintained in dynamically consistent manner.

MULTIVARIATE ERROR COVARIANCE ESTIMATES BY MONTE CARLO SIMULATION FOR OCEANOGRAPHIC ASSIMILATION STUDIES

by

Anna Borovikov

Dissertation submitted to the Faculty of the Graduate School of the
University of Maryland, College Park in partial fulfillment
of the requirements for the degree of
Doctor of Philosophy
2005

Advisory Committee:

Professor James Carton, Chair
Dr. Michele M. Rienecker, Advisor
Professor Eugenia Kalnay
Professor Paul Smith
Professor Viktor Yakovenko

© Copyright by
Anna Borovikov
2005

ACKNOWLEDGMENTS

I owe my gratitude to all the people who have made this thesis possible and because of whom my graduate experience has been one that I will cherish forever.

First and foremost I'd like to thank my advisor, Doctor Michele Rienecker for giving me an invaluable opportunity to work on challenging and extremely interesting projects over the past several years. Without her extraordinary theoretical ideas and computational expertise, this thesis would have been a distant dream. It has been a pleasure to work with and learn from such an extraordinary individual.

Thanks are due to Professor James Carton, Professor Eugenia Kalnay, Professor Paul Smith and Professor Viktor Yakovenko for agreeing to serve on my thesis committee and for sparing their invaluable time reviewing the manuscript.

I would also like to acknowledge help and support from some of the staff members. Alverda McCoy's administrative help and cheerful attitude is highly appreciated.

I owe my deepest thanks to my patient and understanding family for all their support during my graduate work.

I would like to acknowledge financial and technical support from NASA, for all the projects discussed herein.

TABLE OF CONTENTS

LIST OF TABLES

LIST OF FIGURES

Chapter 1

Introduction

1.1 Background

Data assimilation provides a framework for the combination of the information about the state of the ocean contained in an incomplete data stream with our knowledge of the ocean dynamics included in a model. The problem of data assimilation may be formulated in statistical terms where, because of uncertainty in both observations and models, an estimate of the state of the ocean at any given time is considered to be a realization of a random variable. An estimate of the state of the ocean is produced as a blend of estimates from observations and model forecast based on prior knowledge of the error statistics of each, with some measure of the uncertainty in the estimate. The differences among assimilation methods lie primarily in the approaches taken to estimate the error statistics associated with the forward (dynamical) model, the so-called background or forecast error statistics. Since an accurate representation of the observation and forecast error statistics is crucial to a successful data assimilation, a lot of effort has been expended in this direction.

1.2 Forecast error covariance models

One simplifying assumption that is often made is that the forecast error statistics do not change significantly with time and thus can be approximated by a constant probability distribution. This is the basis of the Optimal Interpolation (OI) data assimilation scheme, also known as statistical interpolation (e.g., Daley 1991, Chapters 4 and 5). An alternative to this assumption is to allow for time evolution of the probability distribution. An example of such a data assimilation scheme is the Kalman Filter (Kalman 1960), in which the model and data errors are assumed to be normally distributed and the forecast error covariance matrix is evolved prognostically. The

Kalman Filter can be shown to give an optimal estimate in the case of linear dynamics and linear observation operator. To account for nonlinear processes a generalization of the Kalman Filter, the Extended Kalman Filter uses instantaneous linearization (and often a truncation) of the model equations during the update of the error covariance matrix and the full equations to update the model forecast (e.g., Daley 1991; Ghil and Malanotte-Rizzoli 1991). However, time stepping the forecast error covariance matrix is computationally expensive, rendering this method impractical when used with high-resolution general circulation models. Under certain conditions it is possible to use an asymptotic Kalman Filter (e.g., Fukumori et al. 1993), where a steady-state covariance matrix replaces the time-evolving one. An Ensemble Kalman Filter (EnKF) was introduced by Evensen (1994) based on a Monte Carlo technique in which the forecast error statistics are computed from an ensemble of model states evolving simultaneously. The methodology of the EnKF was further refined by adding perturbations to the observations (e.g., Burgers et al. 1998) to maintain consistent variance in the ensemble analysis. An application of this method with the Poseidon ocean model used in this study has been developed by Keppenne and Rienecker (2002, 2003). Zhang and Anderson (2003) describe an ensemble adjustment Kalman filter (EAKF) which is another modification of the Kalman filter based on a Monte Carlo approach, and compare it to an ensemble OI scheme (time-invariant forecast error, but spatial structure is derived from a collection of state vectors) as well as an OI with functionally prescribed covariances. Their conclusion is that when applied to a simple atmospheric model an ensemble OI can produce reasonably good assimilation results if the covariance matrix is chosen appropriately.

1.3 Multivariate aspect of the forecast error covariance matrix

This study focuses on the importance of the multivariate aspect of the forecast error covariance in the context of data assimilation using OI. Provided with a fairly good observing network, the background error structure can be estimated using analysis of spatial and temporal decorrelation scales, as done in numerous meteorological applications (Ghil and Malanotte-Rizzoli 1991; Derber et al. 1991). However, even for atmospheric data assimilation, the observing system is not

adequate to support a full calculation of the background error covariance statistics, hence model forecasts are often used for error estimation, as, for example, done in the "NMC method" (Derber et al. 1991).

1.4 Monte Carlo approach

The vastness and complexity of the domain and relative scarcity of oceanographic observations would require additional simplifying assumptions in similar calculations. To avoid imposing severe restrictions on the error covariance calculation due to limited data availability, this study explores the efficacy of estimating the forecast error from an ensemble of model integrations. Several studies used a Monte Carlo approach to estimate forecast error covariance structure from an ensemble of assimilation integrations with randomly perturbed observations (Fisher and Andersson 2001) or randomly perturbed background states and observations (Buehner 2005). Houtekamer et al. (1996) use an ensemble in which the uncertain elements of the forecast system are perturbed in different ways for different ensemble members, including perturbations to observations, perturbations to the model's parameters and perturbations to the surface fields. A Monte Carlo technique similar to the EnKF is used here. An important advantage of using an ensemble of ocean states is that it provides a natural way to estimate cross-covariances between the fields of different physical variables constituting the model state vector while incorporating model balance relations and the influence of boundaries. The idea of a multivariate forecast error covariance matrix has been implemented in the oceanographic context, for example, to relate the tide gauge data (Cane et al. 1996) and surface velocity data (Oke at al. 2002) to the dynamically varying quantities in the water column below.

There are many questions that arise with the multivariate approach. For example, how large should the ensemble be, and more generally, how should it be generated? Other questions are related to the underlying assumption of the stationarity and the unbiased nature of error statistics in the OI algorithm. Will a one-time estimate of the forecast error, derived from a Monte Carlo ensemble, be a good representation of this error at another time, at any time during

assimilation? Or, in other words, what is the variability of the forecast error covariance structure? What are the dominant time scales? Can this information be acquired and, if so, used to improve the assimilation scheme?

1.5 Oceanographic context

The primary interest of this study is ocean phenomena taking place on seasonal-to-interannual time scales. One example of such phenomena is the quasi-regular occurrence of El Niño - a large scale warming of near-surface temperature in the eastern equatorial Pacific Ocean accompanied by a basin wide perturbation in the tilt of the thermocline across the equatorial ocean (e.g., Philander 1990). The Poseidon ocean model used in this study is shown to provide a good simulation of the tropical and equatorial dynamics. The data available from the Tropical Ocean Atmosphere (TAO) array provides daily subsurface temperature measurements across the region of interest with the buoys permanently placed 10-15 degrees apart in the zonal direction between 140°E and 95°W and 1-3 degrees apart in meridional direction between 8°S and 8°N. The array resolves much of the large spatial scales relevant to the variability on seasonal to interannual time scales and has provided a wealth of information for El Niño forecasting since its inception. The estimate of error statistics derived below attempts to capture errors associated with seasonal-to-interannual variability for which the array is well suited.

1.6 Outline of the thesis

The logical organization of the rest of the thesis is as follows. First the OI assimilation algorithm, model and data are described (Chapter 2). Then the forecast error covariance model, a traditional Gaussian model of the forecast error covariance and the empirical multivariate model of interest, are detailed (Chapter 3). Then the multivariate error covariance model properties are explored (Chapter 4). After the experimental setup is described, the results of multivariate assimilation are compared with univariate assimilation and the univariate assimilation improved by a salinity adjustment scheme (Chapter 5). The robustness of multivariate assimilation analyses

is assessed by comparing results with different realizations of the forecast error covariance matrix (Chapter 6). Then the roles of leading and trailing eigenvectors are discussed (Chapter 7). The approximation of the local errors described by the trailing empirical orthogonal functions (EOFs) with a simple functional model for computational efficiency is presented next (Chapter 8). This is followed by a discussion of simultaneous inversion of the two different types of observations: temperature and salinity, which is only possible in a multivariate context (Chapter 9). Thesis concludes with a summary (Chapter 10).

Chapter 2

OI framework

2.1 Introduction

A detailed discussion of sequential data assimilation algorithms can be found in earlier literature (see for example, Lorenc 1986, Daley 1991 or Cohn 1997). Here, only a brief outline is given to introduce necessary terminology and notation.

The aim of a data assimilation algorithm is to determine the best estimate of the state vector based on the estimates available from both model and observations. A dynamic (prediction) model can be represented in terms of a nonlinear operator $\Psi(\mathbf{x})$, where $\mathbf{x}$ is a state vector of length n_x. Let $\mathbf{d}$ denote a vector of observations which has dimension $n_d \ll n_x$ (typical for ocean applications) and an element of $\mathbf{d}$ is not necessarily an element of the state vector $\mathbf{x}$. Formally, an optimal estimate of the state would minimize a "cost" functional, which can be defined, for example, to represent the total mean squared error of the system - a measure of the misfit between the estimate and observations and other desired constraints, each with their own "cost" or "risk". For example, written as

$$\mathcal{J}(\mathbf{x}) = (\mathbf{x} - \mathbf{x}^f)^T \mathbf{P} (\mathbf{x} - \mathbf{x}^f) + (\mathbf{d} - \mathcal{H}(\mathbf{x}))^T \mathbf{R} (\mathbf{d} - \mathcal{H}(\mathbf{x})), \tag{2.1}$$

the cost functional $\mathcal{J}(\mathbf{x})$ contains a model error term and a data misfit term. Here $\mathbf{x}^f$ denotes the model simulated state, and $\mathcal{H}(x)$ denotes the observation transformation operator, which relates the observed quantities and the model variables. Other terms, such as boundary condition error or smoothness constraints, may be explicitly included in $\mathcal{J}(\mathbf{x})$. The matrix $\mathbf{P}$ and $\mathbf{R}$ are weights representing our confidence in the model and the data respectively. Specification of these weight matrices requires some prior knowledge of the model and data error statistics.

A discrete form of the model can be written as $\mathbf{x}_k = \Psi_{k-1}(\mathbf{x}_{k-1})$, where $\mathbf{x}_k$ is the forecast state vector at time level k and Ψ_{k-1} is the numerical approximation to the set of model equations

describing the evolution of the state forward from time $k-1$ to k. Similarly, observations available at time k can be denoted as $\mathbf{d}_k$ and the observation transformation operator, the transformation from model variable to observation, as $\mathcal{H}_k(\mathbf{x}_k)$.

2.2 Sequential assimilation scheme

A sequential, unbiased assimilation scheme for the time-varying $\mathbf{x}_k$ is given by:

$$\mathbf{x}_k^f = \Psi_{k-1}(\mathbf{x}_{k-1}^a) \tag{2.2}$$

$$\mathbf{x}_k^a = \mathbf{x}_k^f + \mathbf{K}_k \left(\mathbf{d}_k - \mathcal{H}_k(\mathbf{x}_k^f) \right) \tag{2.3}$$

Here superscript f stands for the forecast and a for the analysis. The sequential data assimilation schemes that have the form of equation (2.3) differ from each other by the weight matrix $\mathbf{K}_k$ often called the *gain matrix*.

The optimality of $\mathbf{K}_k$ can be defined under certain assumptions about the error statistics. Most sequential data assimilation algorithms are based on assumptions that the observational and model errors have zero mean, are white in time and spatially uncorrelated with each other, and have known spatial covariances (usually it is assumed that at least initially the errors are Gaussian).

Suppose the true evolution of the system is governed by

$$\mathbf{x}_k^t = \Psi_{k-1}(\mathbf{x}_{k-1}^t) + \epsilon_{k-1}^t, \tag{2.4}$$

where ϵ_k^t, called *system noise* or model error, is a (Gaussian) white-noise sequence:

$$E\epsilon_k^t = 0, \; E\epsilon_k^t \left(\epsilon_l^t\right)^T = \mathbf{Q}_k \delta_{kl}.$$

The observations may be described by

$$\mathbf{d}_k = \mathcal{H}_k(\mathbf{x}_k^t) + \epsilon_k^o, \tag{2.5}$$

where ϵ_k^o, the *observational noise* or measurement error, is also a (Gaussian) white-noise sequence,

$$E\epsilon_k^o = 0, \; E\epsilon_k^o \left(\epsilon_l^o\right)^T = \mathbf{R}_k \delta_{kl}.$$

The observational error ϵ_k^o may also include any error of representation of the processes of interest, although such errors will not in general satisfy the assumption of a white, Gaussian sequence. Without any loss of generality, it is also assumed that the system noise and the observational noise are uncorrelated with each other. For the Gaussian form of the covariance function, the minimum variance estimate for the least squares minimizing functional is the maximum likelihood estimate, and the analysis error covariance function is also Gaussian. Under these assumptions, for a linear model and a linear observation transformation operator, $\mathcal{H}_k \equiv \mathbf{H}_k$, the optimal $\mathbf{K}_k$ is given by

$$\mathbf{K}_k = \mathbf{P}_k^f \mathbf{H}_k^T (\mathbf{H}_k \mathbf{P}_k^f \mathbf{H}_k^T + \mathbf{R}_k)^{-1}. \tag{2.6}$$

Here $\mathbf{P}_k^f$ is the forecast error covariance matrix, which, in general, is time-dependent:

$$\mathbf{P}_k^f = \mathbf{\Psi}_{k-1} \mathbf{P}_{k-1}^a \mathbf{\Psi}_{k-1}^T + \mathbf{Q}_{k-1}, \text{ where } \mathbf{P}_k^a = (\mathbf{I} - \mathbf{K}_k \mathbf{H}_k) \mathbf{P}_k^f. \tag{2.7}$$

Here $\mathbf{P}_k^a$ is the analysis error covariance matrix. The accuracy of the estimation of $\mathbf{P_k^f}$ relies on our knowledge of $\mathbf{Q}_k$ and $\mathbf{R}_k$. For a high resolution ocean model with the number of state variables on the order of 10^6, $\mathbf{P}_k^f$ is extremely expensive to store and evaluate in full. Thus, numerous approaches have been suggested to simplify the computation of $\mathbf{P}_k^f$. The traditional OI method assumes that $\mathbf{P}_k^f \equiv \mathbf{P}$ is approximately constant in time and simple functional forms are often used as an approximation. In the case of observational errors, the matrix $\mathbf{R}$ is often assumed to be diagonal and to contain only information about the level of variance in the measurement error due to instrumental imperfection and unresolved small-scale signals. There are means of allowing for simple time evolution of the forecast error variance (see, for example, Ghil and Malanotte-Rizzoli 1991; Rienecker and Miller 1991), but they are not considered here. A full evolution of $\mathbf{P}_k^f$ would be a Kalman filter.

The effects of non-linear dynamics and inhomogeneities associated with ocean boundaries are implicitly taken into account when the empirical forecast error covariance matrix $\mathbf{P}$ is constructed from model integrations as presented in the next section.

2.3 Model and forcing

Assimilation system consists of model, analyses system and data. The model used for this study is the Poseidon reduced-gravity, quasi-isopycnal ocean model introduced by Schopf and Loughe (1995) and used by Keppenne and Rienecker (2002, 2003) for testing the Ensemble Kalman Filter. The model described by Schopf and Loughe (1995) has been updated to include the effects of salinity (e.g., Yang et al. 1999). The model was shown to provide realistic simulations of tropical Pacific climatology and variability (Borovikov et al. 2001). Explicit details about the model are provided in Schopf and Loughe (1995). The prognostic variables are layer thickness, temperature, salinity and the zonal and meridional current components. The generalized vertical coordinate of the model includes a turbulent well-mixed surface layer with entrainment parameterized according to a Kraus-Turner (1967) bulk mixed layer model. The model equations are:

$$
\begin{aligned}
\frac{\partial h}{\partial t} + \nabla \cdot (\mathbf{v}h) + \frac{\partial w_e}{\partial \zeta} &= 0, \\
\frac{\partial hT}{\partial t} + \nabla \cdot (\mathbf{v}hT) + \frac{\partial w_e T}{\partial \zeta} &= \frac{\partial}{\partial \zeta}\left(\frac{\kappa}{h}\frac{\partial T}{\partial \zeta}\right) + \frac{\partial Q}{\partial \zeta} + h\mathcal{F}_H(T), \\
\frac{\partial hS}{\partial t} + \nabla \cdot (\mathbf{v}hS) + \frac{\partial w_e S}{\partial \zeta} &= \frac{\partial}{\partial \zeta}\left(\frac{\kappa}{h}\frac{\partial S}{\partial \zeta}\right) + h\mathcal{F}_H(S), \\
\frac{\partial P}{\partial \zeta} &= -g\rho h, \\
P'(0) &= g\rho_0\eta, \\
\frac{\partial P'}{\partial \zeta} &= \rho_0 b h, \\
\eta &= \frac{1}{g}\int b h d\zeta, \\
\frac{\partial (\mathbf{v}h)}{\partial t} + \nabla \cdot (\mathbf{v}h\mathbf{v}) + \frac{\partial w_e \mathbf{v}}{\partial \zeta} &= -\frac{h}{\rho_0}\nabla P' - bh\nabla z - fh\mathbf{k}\times\mathbf{v} + \frac{\partial}{\partial \zeta}\left(\frac{\nu}{h}\frac{\partial \mathbf{v}}{\partial \zeta}\right) + \frac{1}{\rho_0}\frac{\partial \tau}{\partial \zeta} + h\mathcal{F}'_v(\mathbf{v}).
\end{aligned}
\tag{2.8}
$$

Here ζ is the generalized vertical coordinate, h is layer thickness, $\mathbf{v}$ is the 2D horizontal velocity vector, w_e is mass flux across ζ surfaces, T is potential temperature, S is salinity, Q is external heat flux, P is pressure, ρ is density, η is dynamic height, b is buoyancy, τ is wind stress, κ and ν are vertical diffusivities and friction, and $\mathcal{F}_H$ is a horizontal smoothing operator, $\mathcal{F}'_v$ is a friction term.

For this study, the domain is restricted to the Pacific Ocean (45°S to 65°N) with realistic

land boundaries. At the southern boundary the model temperature and salinity are relaxed to the Levitus and Boyer (1994) climatology. The horizontal resolution of the model is 1° in longitude; and in the meridional direction a stretched grid is used, varying from 1/3° at the equator to 1° poleward of 10°S and 10°N. The calculation of the effects of vertical diffusion, implemented at three-hour intervals through an implicit scheme, is parameterized using a Richardson number-dependent vertical mixing following Pacanowski and Philander (1981). The diffusion coefficients are enhanced when needed to simulate convective overturning in cases of gravitationally unstable density profiles. Horizontal diffusion is also applied daily using an 8th-order Shapiro (1970) filter.

One of the primary sources of error in ocean analyses is the atmospheric forcing, i.e. the boundary conditions at the surface. Here, surface wind stress forcing is obtained from the Special Sensor Microwave Imager (SSM/I) surface wind analysis (Atlas et al. 1991) based on the combination of the Defense Meteorological Satellite Program (DMSP) SSM/I data with other conventional data and the European Centre for Medium-Range Weather Forecasts (ECMWF) 10m surface wind analysis. The surface stress was produced from this analysis using the drag coefficient of Large and Pond (1982). Monthly averaged wind stress forcing was applied to the model. The precipitation is given by monthly averaged analyses of Xie and Arkin (1997). The net surface heat flux is estimated using the atmospheric mixed layer model of Seager et al. (1994) with monthly averaged time-varying air temperature and specific humidity from the NCEP-NCAR reanalysis (e.g., Kalnay et al. 1996) and climatological shortwave radiation from the Earth Radiation Budget Experiment (ERBE) (e.g., Harrison et al. 1993), and climatological cloudiness from the International Satellite Cloud Climatology Project (ISCCP) (e.g., Rossow and Schiffer 1991).

Model mean (1988-1997) temperature, salinity and zonal velocity sections along the equator in general compare very well with estimates made from observations (Johnson et al. 2002) taken during an overlapping period (Figure 2.1). The temperature structure has a slightly more diffuse thermocline in the eastern equatorial Pacific compared with the observed; salinity is too fresh (by < 0.1) in the east near 100 m. In zonal velocity the model structure of the undercurrent is slightly thicker that observed and is slightly too strong near the western boundary.

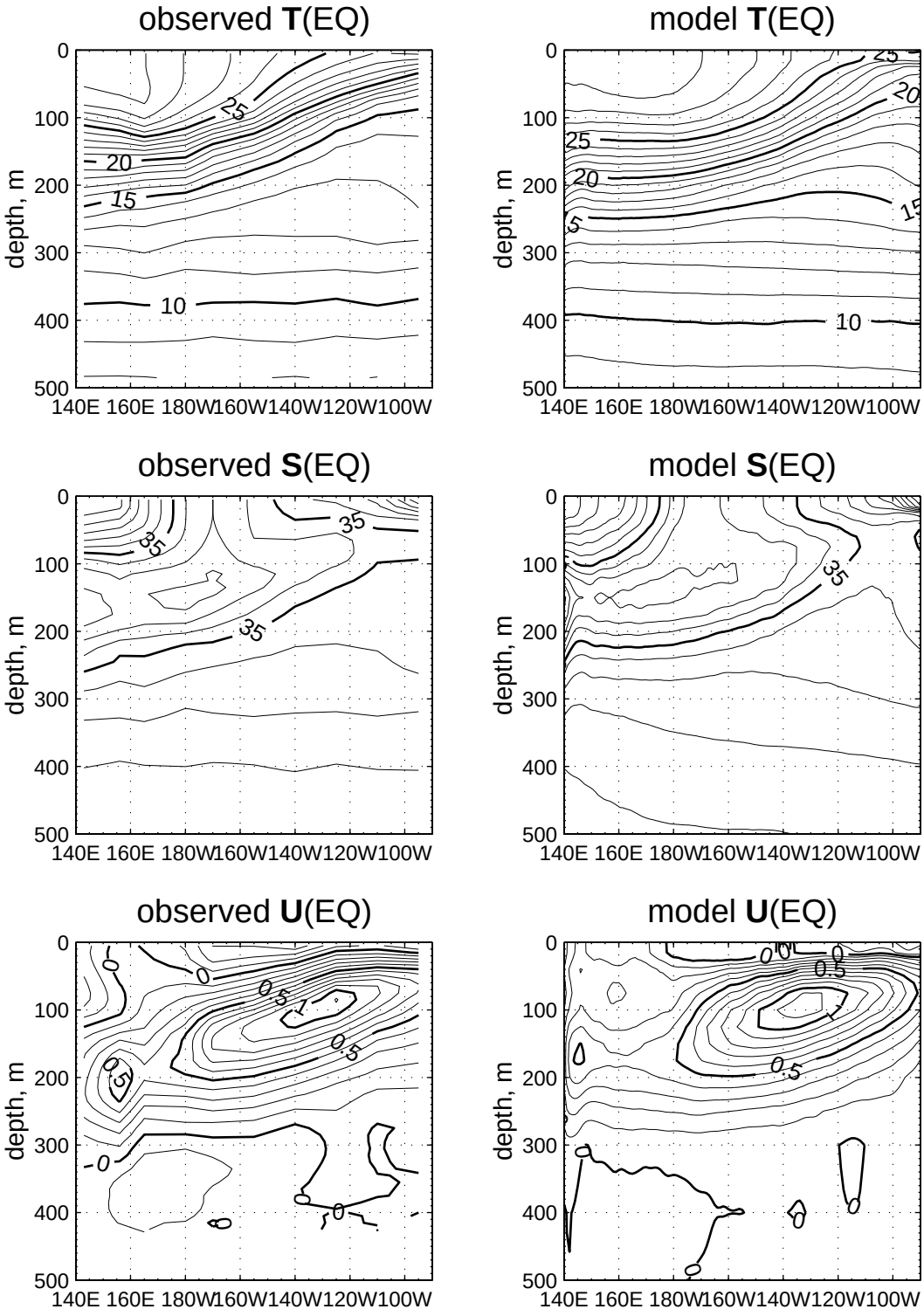

Figure 2.1: Equatorial cross-section of the Poseidon model means (1988-1997) of temperature, salinity and zonal velocity (right panels) and corresponding data-based estimates (left panels) from Johnson et al.(2002). The contour interval in temperature is 1°C, in salinity 0.1 and in zonal velocity 0.1 ms^{-1}.

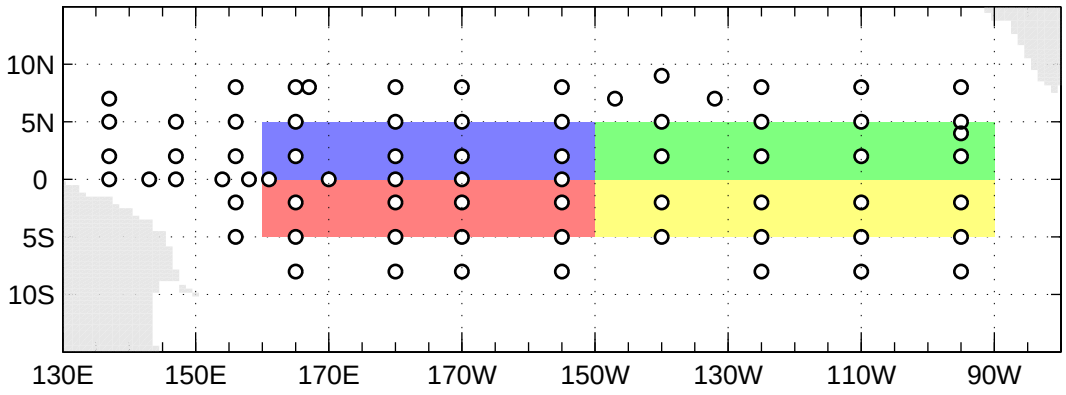

Figure 2.2: Map of the TAO array, consisting of approximately 70 moored ocean buoys in the Tropical Pacific Ocean. The shading shows Niño 4 (red-blue) and Niño 3 (yellow-green) regions.

2.4 Data

The TAO/Triton Array (Figure 2.2), consisting of more than 70 moored buoys spanning the equatorial Pacific (http://www.pmel.noaa.gov/toga-tao/home.html and McPhaden et al. 1998), measures oceanographic and surface meteorological variables: air temperature, relative humidity, surface winds, sea surface temperatures and subsurface temperatures down to a depth of 500 meters. By 1994 these measurements became available daily approximately uniformly spaced at 10-15° longitude and 2-3° latitude degrees across the equatorial Pacific Ocean.

The temperature observations from the TAO/Triton array were the only data type used in these assimilation experiments since the focus is on well-known deleterious effects of temperature assimilation in the equatorial waveguide, as discussed, for example, in Troccoli et al. (2002) and in Troccoli et al. (2003). The standard deviation of the observational error, denoted σ_{TAO}, is set to 0.5°C and the errors are assumed to be uncorrelated in space and time. This value is high compared to the instrumental error of 0.1°C (Freitag et al. 1994) since it also has to reflect the representativeness error - i.e., the data contains a mixture of signals of various scales including frequencies much higher than the target scales of assimilation. By tuning σ_{TAO} we effectively control the ratio of the data error variance to the forecast error variance.

Chapter 3

Forecast Error Covariance Modeling

3.1 Introduction and notation: UOI, UOI+S, MvOI

In error covariance structure modeling, one is striving for an accurate representation of the error statistics as well as for simple and efficient implementation for computational viability. With little knowledge of the true nature of the forecast error covariances, one often has to make assumptions and settle for simple methods that usually have the advantage of being easy to implement. This chapter describes two different models for the forecast error covariance structure, a simpler and less computationally intense and a more elaborate and more accurate model. For both, an OI framework is used wherein the forecast error covariance matrix, $\mathbf{P}^f$, is assumed to be time-invariant. The first model is based on a functional form of the forecast error covariance for a single observed variable (temperature) and thus the assimilation scheme using it is called univariate Optimal Interpolation (UOI). Since UOI is known to have a detrimental impact on the salinity structure (this will be illustrated later), a variation of the UOI scheme, which aims to improve the basic UOI by explicitly correcting the salinity field in a manner consistent with the temperature correction, is considered also. This assimilation scheme is referred to as UOI+S. It will provide a measure for performance of the OI with the multivariate forecast error covariance model (MvOI).

3.2 Univariate functional model

A commonly used analytical error covariance function (e.g., Carton and Hackert 1990, Ji et al. 1995) has been employed for the tropical Pacific Ocean region: the spatial structure of the model temperature (T) forecast error is assumed to be Gaussian in all three dimensions, i.e. $\exp(-\Delta d^2/L_d^2)$. Here Δd stands for distance between two points in the d (x, y or z) direction.

The scales used in this study, $L_x = 15°$, $L_y = 4°$ and $L_z = 50m$ in zonal, meridional and vertical directions, respectively, were estimated from the ensemble of model integrations described in the next subsection. These spatial scales are also (marginally) resolved by the equatorial moorings which are nominally separated by 10° to 15° in the zonal direction and by 2° to 3° in the meridional direction. Horizontal scales are comparable to scales used in similar assimilation schemes (e.g., Ji et al. 1995 and Rosati et al. 1996). There are several advantages to this error covariance model. It is relatively easy to implement and adapt to parallel computing architecture. The study by Rosati et al. (1997) also shows that use of such empirical covariance scales, though simplified, are nevertheless effective for improving seasonal forecasts.

In the univariate implementation the temperature observations have been processed and the correction was made only to the model temperature field during each assimilation cycle, while other variables adjusted according to the model's dynamic response to the temperature correction.

3.2.1 Salinity increments to preserve water-mass distribution

Troccoli and Haines (1999) proposed a scheme to preserve the water-mass distribution of the model prior to assimilation. The idea stems from the fact that vertical displacements of the water column, because of internal wave motion or the passage of mesoscale features, can occur without significant changes in the water mass properties. Even for the case of non-monotonic $S = S(T)$, two (or more) isothermic parcels can be distinguished according to their depth and the salinity correction scheme recovers salinity from the nearest $T(z)$ in the background field.

The scheme is presented fully in Troccoli and Haines (1999) and only briefly here. The procedure is applied at each grid point in two steps. First, a vertical displacement of the model T background profile to match the deepest analysis $T$is made. The same displacement is applied to the S profile, too. Second, the scheme computes an S increment using the $T - S$ relationships from the model T- and S-background profiles and the analyzed T, at each grid point, according

to the following formulation:

$$S(z_{an}) = S_{bg}(z_{bg}) \text{ if } |z_{an} - z_{bg}| \leq \Delta z$$
$$S(z_{an}) = S_{bg}(z_{an}) \text{ if there is no } z_{bg} \text{ such that } T_{bg}(z_{bg}) = T_{an}(z_{an}), \text{ or } |z_{an} - z_{bg}| > \Delta z. \tag{3.1}$$

Here Δz is a specified depth tolerance, which could be a function of location. In the case presented Δz is chosen to be fixed at 100m. Subscripts an and bg stand for analysis and background, respectively, and $z_{bg} = z(T_{bg} = T_{an})$ is the depth at which the background temperature is the same as the analysis temperature. In case of multiple $z(T_{bg} = T_{an})$ solutions, the nearest depth to z_{an} is considered. Also, the T-S preservation assumption generally does not hold near the surface, so the salinity is not updated in the surface isothermal layer.

3.3 Monte Carlo method for estimating the multivariate forecast error covariance

A more realistic covariance structure that is consistent with model dynamics and the presence of ocean boundaries was sought through an application of the Monte Carlo method. The variability across an ensemble of ocean state estimates was used for a one-time estimate of the forecast error statistics. This approach is similar in spirit to the Ensemble Kalman Filter except that the error covariance does not evolve with time and does not feel the impact of prior data assimilation, although it could.

The design of this forecast error covariance model was influenced by the need to assimilate TAO mooring observations for seasonal forecasts. While the Poseidon model has a layered configuration, the TAO observations are taken at approximately constant depth levels. In the implementation for this study, the covariances are calculated on pre-defined depth levels. At each assimilation cycle the model fields are interpolated to these depths, the assimilation increments are computed on these pre-specified levels, and are then interpolated back to the temperature grid points at the center of the model layers. The discussion below deals with the three-dimensional forecast error covariance matrix whose horizontal structure coincides with the model grid, and in the vertical is arranged at depths coincident with the nominal TAO instrument depths.

Consider the non-dimensionalized model state vector

$$\mathbf{x} = \begin{bmatrix} T/\sigma_T \\ S/\sigma_S \\ U/\sigma_U \\ V/\sigma_V \\ ssh/\sigma_{ssh} \end{bmatrix}, \tag{3.2}$$

where T, S, U, V and ssh are model variables: temperature, salinity, zonal and meridional velocities and dynamic height respectively, and $\sigma_{[T,S,U,V,ssh]}$ are non-dimensionalizing factors. For the latter we took the global standard deviation within each of the model fields at a depth of 100 m (the depth of highest variability, around the thermocline): σ_T=0.65°C, σ_S=0.08, σ_U=0.09 ms^{-1}, σ_V=0.08 ms^{-1} and σ_{ssh}=0.08 m. The multivariate covariance matrix is

$$\mathbf{P} = \begin{bmatrix} \mathbf{P}^{T,T} & \mathbf{P}^{T,S} & \mathbf{P}^{T,U} & \mathbf{P}^{T,V} & \mathbf{P}^{T,ssh} \\ \mathbf{P}^{T,S} & \mathbf{P}^{S,S} & \mathbf{P}^{S,U} & \mathbf{P}^{S,V} & \mathbf{P}^{S,ssh} \\ \mathbf{P}^{U,T} & \mathbf{P}^{U,S} & \mathbf{P}^{U,U} & \mathbf{P}^{U,V} & \mathbf{P}^{U,ssh} \\ \mathbf{P}^{V,T} & \mathbf{P}^{V,S} & \mathbf{P}^{V,U} & \mathbf{P}^{V,V} & \mathbf{P}^{V,ssh} \\ \mathbf{P}^{ssh,T} & \mathbf{P}^{ssh,S} & \mathbf{P}^{ssh,U} & \mathbf{P}^{ssh,V} & \mathbf{P}^{ssh,ssh} \end{bmatrix}. \tag{3.3}$$

If the matrix $\mathbf{A}^{m \times n_x}$ contains the m-member ensemble of (anomalous) ocean states as columns, then $\mathbf{P}$ can be computed as

$$\mathbf{P}^{n_x \times n_x} = \frac{\mathbf{A}\mathbf{A}^T}{m-1}, \text{with } rank(\mathbf{P}) \leq \min\{m, n_x\}. \tag{3.4}$$

The size of $\mathbf{P}$ is of the order of $n_x \approx 10^6$ (the dimension of the state vector), while its rank is no larger than the size of the ensemble, m (on the order of 10^2 in the case of this study). Since the rank of the error covariance matrix $\mathbf{P}$ estimated using this method is so small, it can be conveniently represented using a basis of empirical-orthogonal functions (EOFs), $\mathbf{E}$. EOFs have been widely employed in oceanographic contexts (e.g., Cane et al. 1996, Kaplan et al. 1997), and the relevant theoretical background can be found, for example, in Preisendorfer (1988). The necessary linear algebra concepts may be reviewed by using Golub and Van Loan (1996).

To compute the EOF representation of $\mathbf{P}$, observe that $\mathbf{A}\mathbf{A}^T$ has the same eigenvalues as $\mathbf{A}^T\mathbf{A}$, which is only $m \times m$ and the eigenvectors of $\mathbf{A}\mathbf{A}^T$ are related to those of $\mathbf{A}^T\mathbf{A}$ as

$$\mathbf{E} = \mathbf{A}\mathbf{U}(\mathbf{\Lambda})^{-1/2}, \tag{3.5}$$

where $\mathbf{E}^{n_x \times m}$ contains the eigenvectors of $\mathbf{A}\mathbf{A}^T$, $\mathbf{U}^{m \times m}$ contains the eigenvectors of $\mathbf{A}^T\mathbf{A}$ and $\mathbf{\Lambda}^{m \times m} = diag(\lambda_1^2, ..., \lambda_m^2)$ has the eigenvalues of $\mathbf{A}^T\mathbf{A}$. Then, since $\mathbf{U}$ is orthogonal (Golub and Van Loan 1996, p. 393),

$$\mathbf{P} = \frac{\mathbf{A}\mathbf{A}^T}{m-1} = \frac{\mathbf{E}\mathbf{\Lambda}\mathbf{E}^T}{m-1} = \mathbf{L}\mathbf{L}^T, \text{ with } \mathbf{L} = \mathbf{E}\mathbf{\Lambda}^{1/2}(m-1)^{-1/2}. \tag{3.6}$$

The columns of $\mathbf{E}$ are orthonormal and the eigenvalues, λ_i^2, $i = 1, ..., m$, are the variances explained by each eigenvector. Equation 2.6 can thus be rewritten as

$$\mathbf{K} = \mathbf{L}\mathbf{L}^T\mathbf{H}^T(\mathbf{H}\mathbf{L}\mathbf{L}^T\mathbf{H}^T + \mathbf{R})^{-1}. \tag{3.7}$$

3.3.1 Ensemble generation

As the first test of this methodology, the ensemble of states was generated by forcing the ocean model with an ensemble of air-sea fluxes:

$$\mathbf{F}_n = \mathbf{F} + \delta\mathbf{F}_n. \tag{3.8}$$

$\mathbf{F}$ is the forcing used for the control run, $\delta\mathbf{F}_n$ are interannual anomalies - in phase with respect to the annual cycle and interannual SST anomalies but with different internal atmospheric chaotic variations. Surface forcing is used for the ensemble generation because this is probably the dominant source of error in the upper ocean in the equatorial Pacific. Our approach is similar to Cane et al. (1996) in the sense that all the ensemble variability is a result of the perturbations to the atmospheric forcing, although the implementation details differ. Although errors in the synoptic forcing will be large, the focus here is on the longer time scales of interest for seasonal prediction. The fluxes were obtained from a series of integrations of the Aries atmospheric model (e.g., Suarez and Takacs 1995) forced by the same interannually varying sea surface temperatures (SST) and differing only in slight perturbations to the initial atmospheric state. The interannual anomalies

in surface stress and heat flux components were added to the seasonal forcing estimated from the sources described in section 2.3. This approach attributes all of the ocean model forecast error to uncertainties in the surface flux anomalies, since differences between the ensemble members were due to atmospheric internal variability. No perturbations were added to the SSTs used for the atmospheric integrations and so the long-term means of the heat fluxes are strongly constrained.

In all, 32 runs were conducted, each 15 years long, corresponding to the 1979-1993 period of the SST data used to force the atmospheric model. Five-day averages (pentads) of the model fields were archived. These were subsequently interpolated to the 11 depth levels, coincident with the depths of the TAO observations. All the covariance estimates have been made using these fields. Selecting at random a pentad from a 15-year period, a computation of the EOFs of the matrix $\mathbf{P}$ was carried out using the ensemble of 32 ocean state realizations. The first EOF explained only about 3% of the total error variance, and this result was similar for many one-time estimates of $\mathbf{P}$ attempted at other randomly selected dates. All eigenvalues of $\mathbf{A}\mathbf{A}^T$ appear to be so close to each other as to be virtually indistinguishable. Apparently, this ensemble was not sufficient to reliably define the subspace containing the leading directions of the forecast error variability. A possible reason for this result is that the small size of the ensemble was not adequate to resolve the dominant modes of variability of such a complex system. Thus, the question arose: how to enlarge the ensemble given the accumulated model output? A natural solution would be to include in the computation fields from the same model run, but selected in such a way as to prevent contamination of the internal model error variability by the temporal variability, such as lag correlation or interannual variations.

Thus, a matrix of ensemble members, $\mathbf{A}$, was formed by selecting at random five years from the 15 year period, then choosing a pentad from each year corresponding to the same date, say, the first of January. Such a choice ensured that the states were sufficiently separated in time to be considered independent. This allowed for the collection of an ensemble of 160 members. This limit was set by practical considerations. The mean was removed separately for each of the 5 years to remove the influence of interannual variability. The EOFs of the matrix $\mathbf{P}$ were then computed.

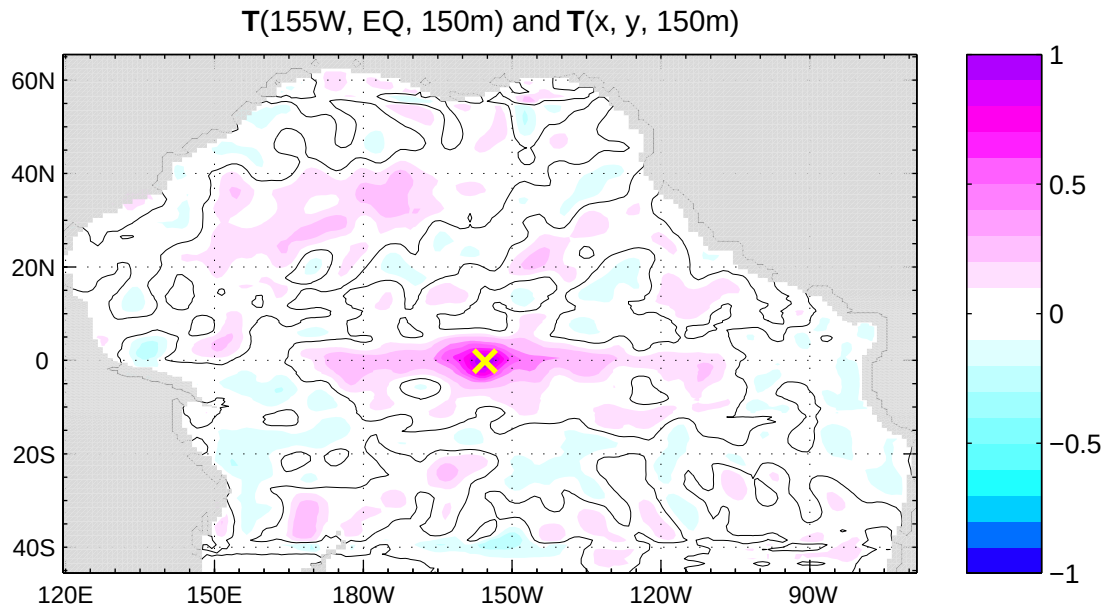

Figure 3.1: An example of correlation structure derived from a 160 member ensemble for the entire model domain. No compact support is applied. The black line marks the 0.0 contour. A cross marks the position of the simulated observation.

The properties of the error covariance matrix constructed in such a way are discussed below.

3.3.2 Compact support

A persistent problem associated with empirical forecast error covariance estimation is the appearance of unphysical large lag spatial correlations that are an artifact of the limited ensemble size (e.g., Houtekamer and Mitchell 1998, fig. 6). We use an ensemble size of 160, yet the potential number of degrees of freedom is $O(10^6)$. Figure 3.1 shows the assimilation correction over the entire Pacific ocean associated with a single simulated observation approximately in the center of the model domain, that would result from empirical EOFs. This correction reflects the forecast error correlation structure - it corresponds to a section of a single row of the $\mathbf{P}$ matrix. This is also termed the marginal gain since it measures the impacts of processing a single perfect measurement without reference to other data that might be assimilated. Some regions of strong correlation (greater than 0.3) appear as far from the observation as 30° in meridional and zonal directions.

To alleviate this problem, the multivariate, anisotropic, inhomogeneous matrix was modified

by a matrix specified by a covariance function that vanishes at large distances; i.e., a Hadamard product (i.e. $\mathbf{A} \bullet \mathbf{B}$ such that $\{\mathbf{A} \bullet \mathbf{B}\}_{ij} = \mathbf{A}_{ij}\mathbf{B}_{ij}$) of the two matrices was employed, as discussed by Houtekamer and Mitchell (2001). Keppenne and Rienecker (2002) implemented the compact support for the Ensemble Kalman Filter developed by the NASA Seasonal-to-Interannual Prediction Project (NSIPP) for parallel computing architectures, and that implementation is used in the present study. The functional form follows the work by Gaspari and Cohn (1999) who provided a methodology for constructing compactly supported multi-dimensional covariance functions. The covariance martrix is specified by the 5-th order piecewise rational function

$$\begin{aligned} C_0(s) &= -\tfrac{s^5}{4} + \tfrac{s^4}{4} + \tfrac{5s^3}{8} - \tfrac{5s^2}{3} + 1 \text{ for } 0 \le s \le 1, \\ C_0(s) &= \tfrac{s^5}{12} - \tfrac{s^4}{2} + \tfrac{5s^3}{8} + \tfrac{5s^2}{3} - 5s + 4 - \tfrac{2}{3s} \text{ for } 1 \le s \le 2, \\ C_0(s) &= 0 \text{ for } s \ge 2. \end{aligned} \tag{3.9}$$

Here $s = \frac{\Delta d}{L_d}$, Δd is the distance and L_d is the spatial scale. The characteristic scales of this function were selected in such a way that most of the local features of the empirically estimated error covariance structure are preserved, but at large spatial lags the covariance vanishes: $L_x = 30°$, $L_y = 8°$ and $L_z = 100m$ in the zonal, meridional and vertical directions respectively.

To visualize the details of covariance structure and the impact of compact support application, several artificial examples are considered with a single observation different from a background field by one non-dimensional unit. The correlation between temperature observations at several locations across the equatorial Pacific ocean (156°E, 180°W, 155°W and 125°W) at depths roughly corresponding to the position of the thermocline, estimated by the 20°C isotherm depth, and the temperature elsewhere in the Pacific reveals that with compact support the long range correlation is eliminated, but the local structure is intact (compare Figure 3.2 and Figure 3.3).

3.3.3 Multivariate error covariance patterns

The following discussion of the multivariate error covariance model will focus on the thermocline region in the equatorial Pacific Ocean. The shapes of the correlation structure associated with a single point differ between the eastern and western regions (Figure 3.3, top 4 panels). The

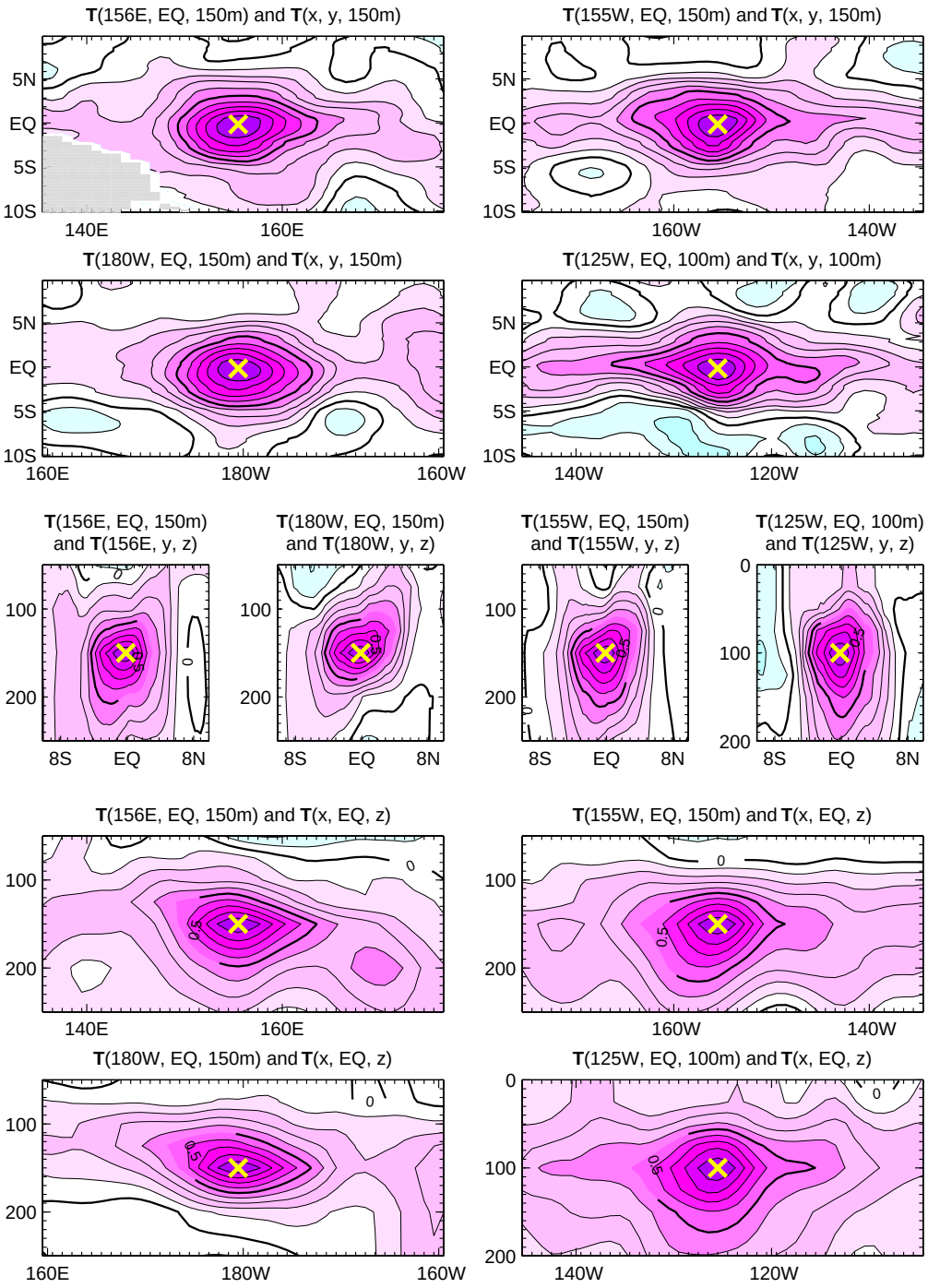

Figure 3.2: Examples of temperature correlation structure derived from a 160-member ensemble. No compact support is applied. Contour interval is 0.1. Crosses mark the position of the simulated observation.

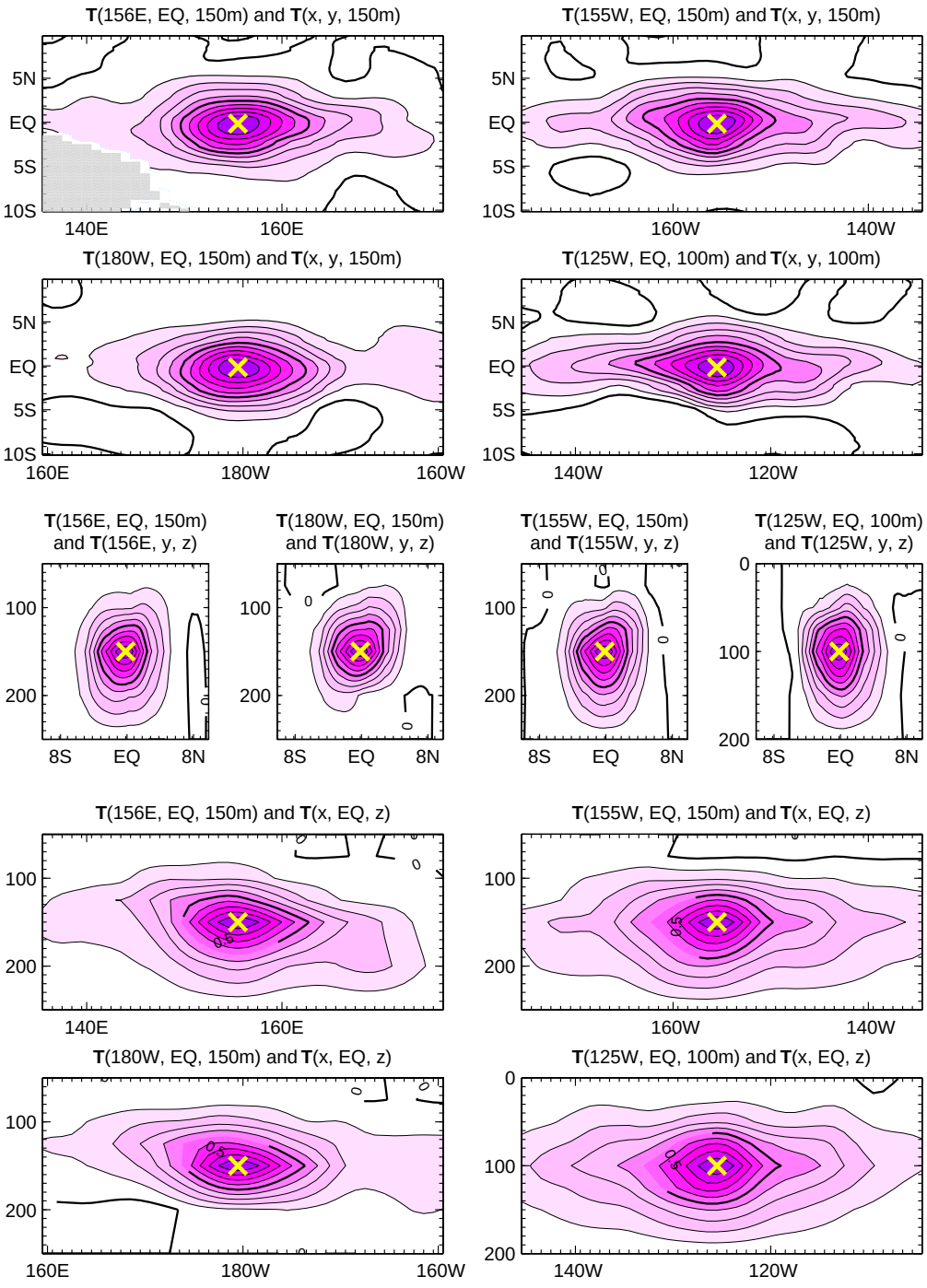

Figure 3.3: Examples of temperature correlation structure derived from a 160-member ensemble. The compact support is applied as described in the text. Contour interval is 0.1. Crosses mark the position of the simulated observation.

zonal scale tends to be shorter in the western and central and longer in the eastern part of the basin. Meridional decay scales are similar along the equator, but the vertical correlation (Figure 3.3, middle 4 panels) varies: shorter and symmetrical in the western part, slightly skewed in the central part and symmetrical but more elongated in the eastern part of the equatorial Pacific basin. Zonal sections (Figure 3.3, bottom 4 panels) illustrate the anisotropy associated with the tilt of the thermocline. This example alone demonstrates that even the error covariance structure of the temperature itself is so complex that a homogeneous error correlation structure is not quite applicable.

Although to date there have been very few salinity observations, this is changing with the Argo program (http://argo.jcommops.org, and Wilson, 2000). Hence, it is of interest to explore corrections associated with salinity observations (Figure 3.4). The decorrelation scales in the western basin are noticeably longer than in the middle and eastern basin, 8 to 10 degrees in zonal and 4 to 6 degrees in meridional direction in the west and 2-4 degrees in zonal and 1-2 degrees in meridional direction in the east. The scales are notably shorter than those for temperature (Figure 3.3) except for the meridional scales in the west.

In a similar fashion one can analyze the temperature-salinity, temperature-velocity and other cross-variable relationships, i.e. the effect of a single unit observation on various fields - components of the ocean state vector. Corrections in S and U fields associated with a T observation and corrections in T and U associated with an S observation are displayed for a single location, 155°W at the equator (figure 3.5).

Examples of the temperature-salinity covariance (Figure 3.5) reveal and reflect the complex and irregular nature of the temperature-salinity relationship. The change in salinity associated with a temperature increment is not necessarily density-compensating. Equatorial temperature and salinity south of the equator in the western region are negatively correlated, while temperature at the equator and salinity immediately to the north are correlated at 150 meters in the western and central Pacific. The scales of influence are short compared with the temperature-temperature relationship. The anticorrelation is consistent with the mean thermohaline (T-S) structure, with

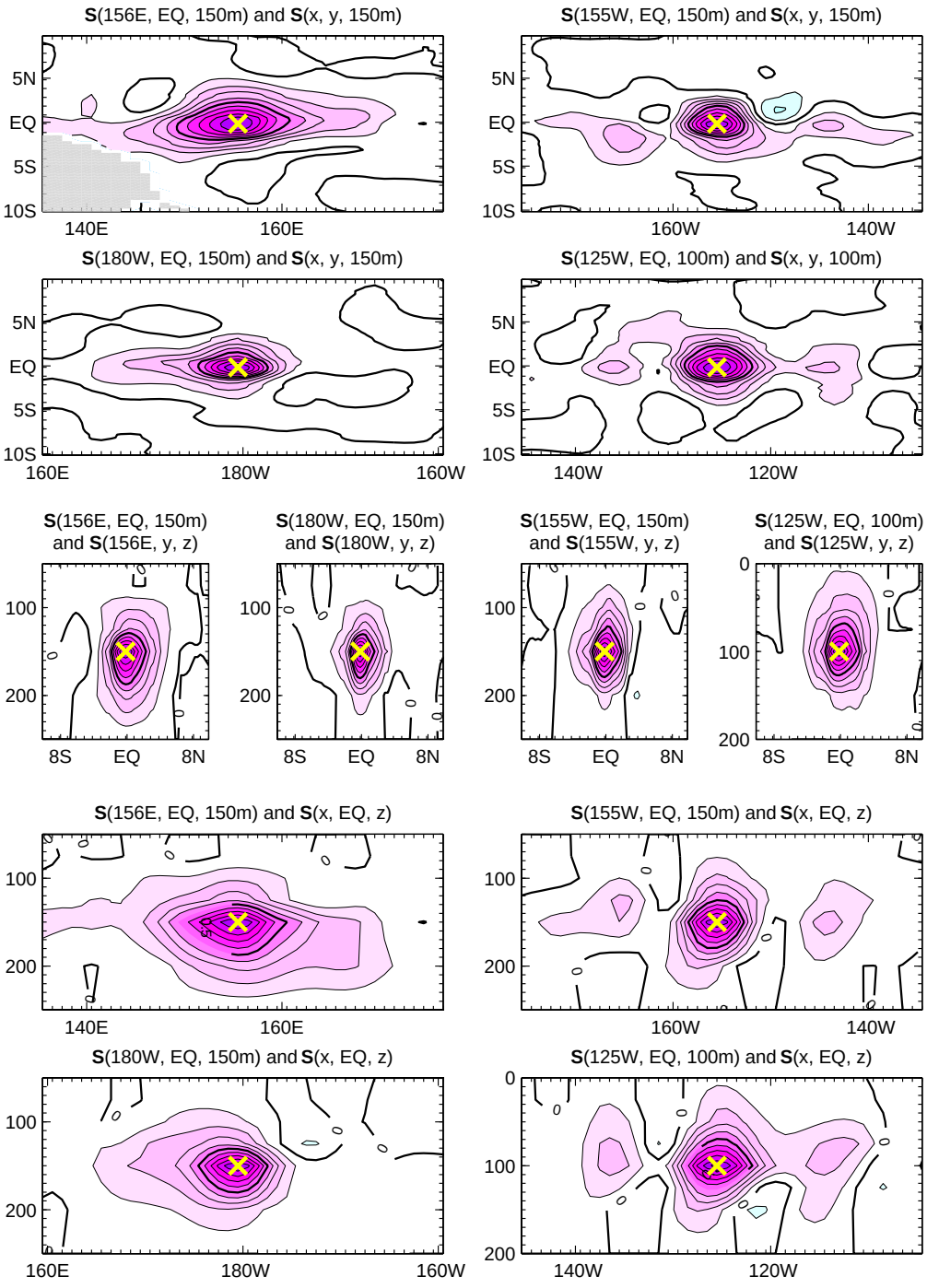

Figure 3.4: Examples of salinity correlation structure derived from a 160-member ensemble. The compact support is applied as described in the text. Contour interval is 0.1. Crosses mark the position of the simulated observation.

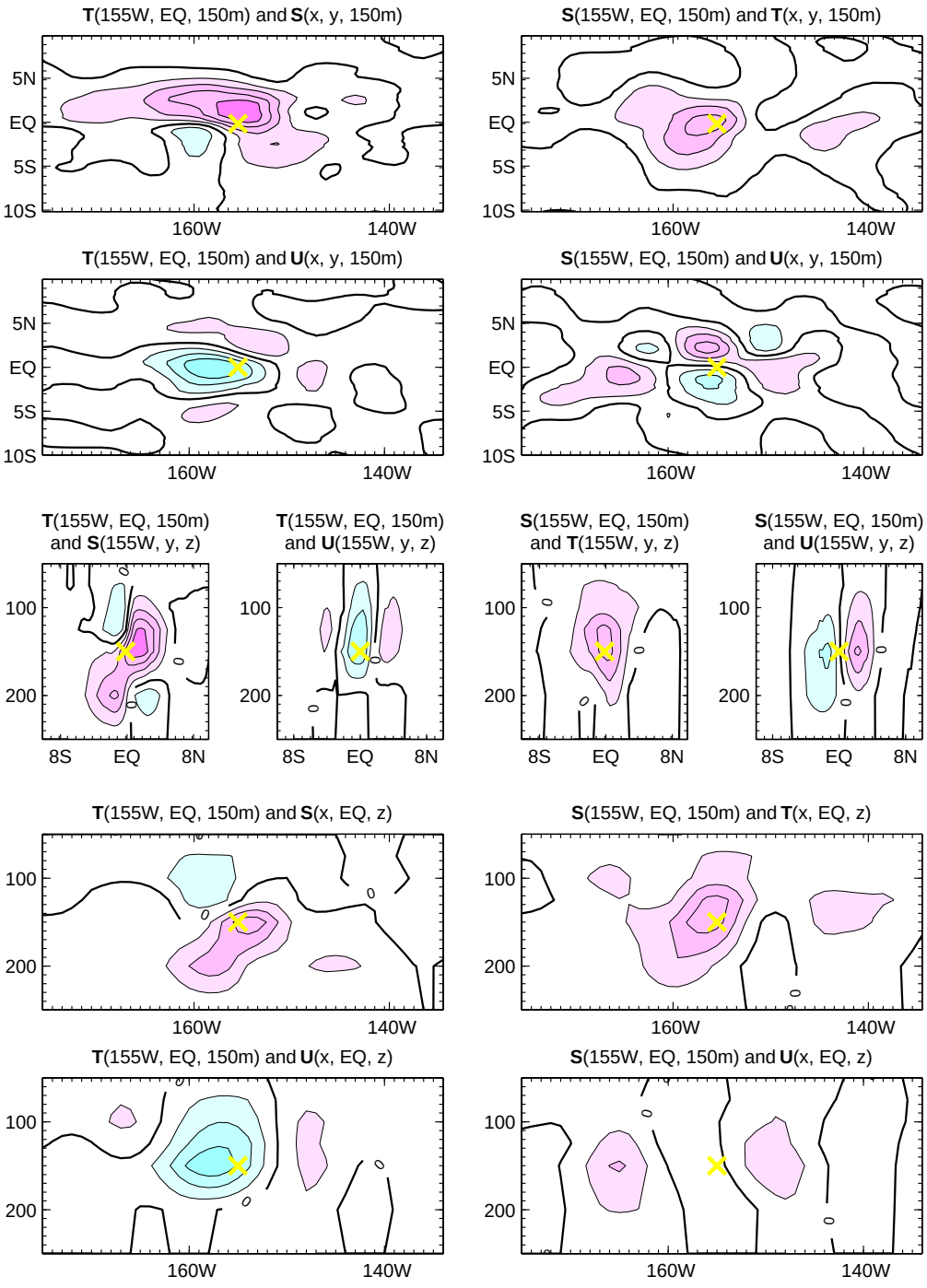

Figure 3.5: Examples of correlation structure derived from a 160-member ensemble. The compact support is applied as described in the text. Various combinations of observed and updated variables are presented. Contour interval is 0.1. Crosses mark the position of the simulated observation.

fresh water overlying a saline core. In the east, the correlation between T and S is primarily vertical; horizontal scales are very short, on the order of 2-4 degrees. The positive correlations on the equator, as seen on the meridional sections of the central basin, are higher towards the northern hemisphere. The negative correlations to the south are consistent with higher temperatures straddling the cold tongue with more saline water south of the equator and fresher water north. Thus the covariances are consistent with vertical and meridional variations.

The relationship between temperature and velocity in the western Pacific reflects temperature changes associated with upstream advection/convergence effects. At 156°E and at the dateline (not shown), the higher temperatures are associated with a weaker equatorial undercurrent in a broad region to the west. At 155°W, the effects are more local and wavelike with increased temperature associated with a stronger equatorial undercurrent. At 125°W (not shown) the scales are shorter and also wavelike, with changes in temperature apparently associated with instability waves.

It is possible to infer from the multivariate analysis the effect a single salinity observation would have on temperature and zonal velocity fields at various locations across the equatorial Pacific ocean. The large positive correlation between salinity and temperature fields in the central and to a lesser degree in the eastern Pacific indicates that the correction of the salinity field may have a significant impact on the temperature. The S-U relationship is weak in the western part of the basin and the correlation patterns are wavelike in the east, strongly pronounced in the north-south direction.

Chapter 4

Robustness of the Forecast Error Covariance Estimate

4.1 Randomly sampled ensembles

In this chapter, the sensitivity of the covariance structure to the choice made in populating the ensemble, i.e., to seasonal or interannual variations in the atmospheric forcing, is explored to evaluate the robustness of the covariance estimates. The robustness is tested by randomly sampling the full suite of integrations. Five years out of 15 (the length of the run) were picked at random, then the same date (e.g., January 1-5 pentad) was taken for each year. As before, the mean across the ensemble was removed for each year. The procedure was repeated ten times allowing us to obtain ten realizations of the covariance matrix $\mathbf{P}$. The pentads were chosen so that realizations from the same season and from different seasons could be compared. From visual assessment of figures similar to Figures 3.3-3.5, the correlation structures represented by the different estimates of $\mathbf{P}$ were very similar.

One comparison of the robustness of covariance estimates is pointwise covariance sections (Figure 4.1) at the same locations as simulated temperature observations as in Figures 3.3-3.4. The tight distribution of the decorrelation curves from the 10 different $\mathbf{P}$ realizations (thin lines) indicates good reproducibility of the covariance structure. No significant interannual variability is apparent within this collection of $\mathbf{P}$ matrices. The overlaid Gaussian curves show that the decorrelation scales vary at the four locations across the equatorial basin and can hardly be fitted by a single parameter (scale estimate) in a functional covariance model. In the UOI covariance model used for comparison below, the temperature decorrelation scales chosen are consistent with the scales of the empirical error covariance model in the western and central equatorial Pacific.

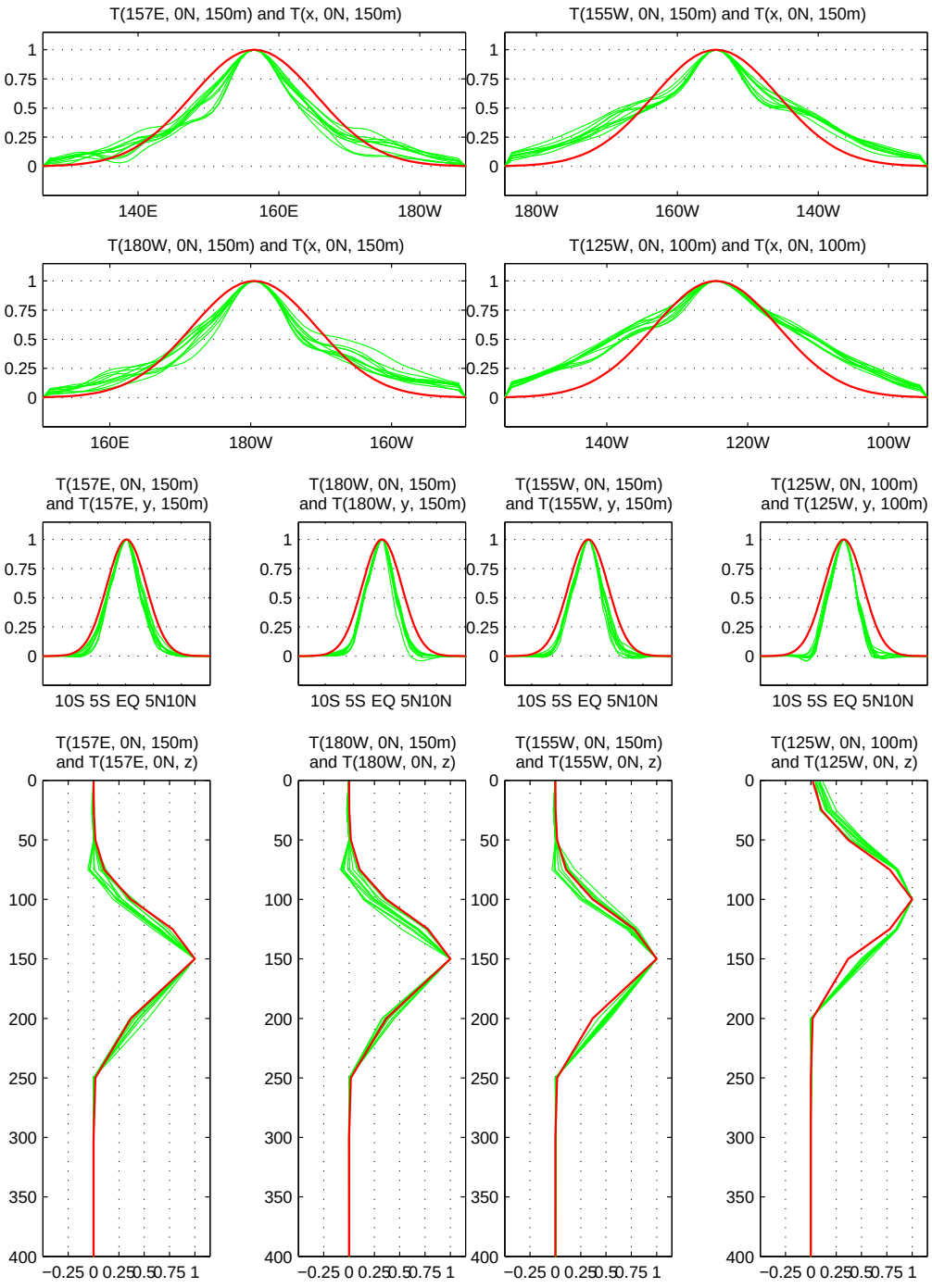

Figure 4.1: One-dimensional decorrelation curves (zonal, meridional and vertical directions) corresponding to simulated observation at the specified locations. Each green line is produced by a different realization of the error covariance matrix. Compact support is applied as described in section 3.3.2. Red lines show the Gaussian functional error covariance model used in UOI.

4.2 Invariance of the error subspace

The difference among the Monte Carlo estimates of $\mathbf{P}$ can also be quantified in terms of the dominant error subspaces spanned by each of the ensemble sets. These subspaces are best described by the orthonormal bases of empirical orthogonal functions (EOFs). The use of eofs allows a spatial filtering of the covariance structures by inclusion of only those EOFs that are non-noise-like, thus defining the dominant error subspace. This procedure also eliminates problems associated with different levels of variance even though the spatial structures (covariances) are similar.

Consider the projection of an ensemble of ocean state anomalies onto a given set of EOFs. An anomalous ocean state vector $\mathbf{a}$ can be expressed in terms of the EOF basis $\{\alpha\}$ as

$$\mathbf{a} = \Sigma_i a_i \alpha_i + \delta^\alpha. \tag{4.1}$$

The set of eofs $\{\alpha\}$ spans the subspace $\mathcal{S}_\alpha$ of the forecast error space $\mathcal{S}$ and δ^α is the residual lying in the complement of $\mathcal{S}_\alpha$, i.e., subspace $\mathcal{S}_\alpha^c$, orthogonal to $\{\alpha\}$. The space $\mathcal{S}_\alpha^c$ may or may not contain significant forecast error covariability information. To assess the information content not included in $\mathcal{S}_\alpha$ we examine covariability through the EOFs of δ^α. If the EOFs of δ^α are noise-like, this would indicate that the EOFs $\{\alpha\}$ captured the significant information regarding the forecast error covariance contained in $\mathbf{a}$. This calculation was repeated for several instances of $\{\alpha\}$ and $\mathcal{S} = \{\mathbf{a}\}$ to assess the invariability of $\mathcal{S}_\alpha$.

The spectra of various ensembles of $\delta^\alpha \subset \mathcal{S}_\alpha^c = \mathcal{S}_\alpha^\perp$ are shown in Figure 4.2, where $\{\alpha\}$ are calculated from January pentads and $\{\mathbf{a}\}$ are pentads from July. In every case, the eigenvalues of $\{\alpha\}$ and $\{\delta\}$ are normalized by the variance of the corresponding ensemble $\{\mathbf{a}\}$. The eigencurves of $\{\delta\}$ are almost flat, characteristic of white noise, and are an order of magnitude less than the dominant eigenvalues of α. Thus the error subspace generated from this Monte Carlo simulation appears to be robust.

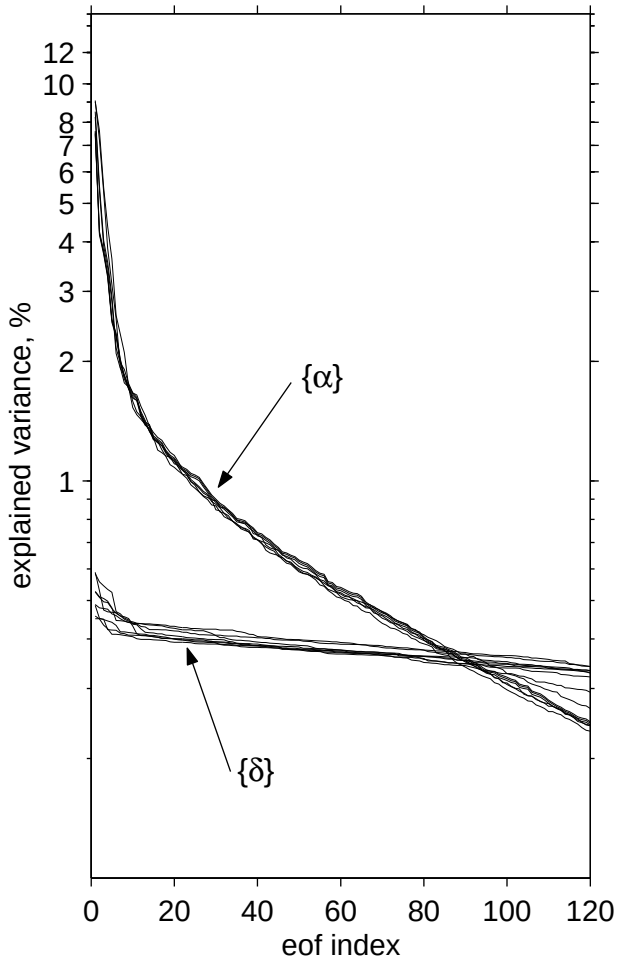

Figure 4.2: Eigenvalues for several realizations of the matrix $\mathbf{P}$ (marked α) and the eigenvalues for ensembles of δ's - the residuals of the projections of an arbitrary collection of anomalous ocean states onto a basis of eofs.

Chapter 5

Assimilation experiments

5.1 Experimental setup

The effectiveness of the empirical multivariate forecast error covariance estimate is assessed by assimilating the temperature observations from the TAO moorings. The evaluation uses a set of independent (i.e., not assimilated) temperature, salinity and zonal velocity observations from the TAO servicing cruises. The temperature and salinity data are based on Conductivity-Temperature-Depth (CTD) profiles and the velocity data from the Acoustic Doppler Current Profiler (ADCP). The comparison uses a gridded analysis of these data, as described by Johnson et al. (2000).

The assimilation experimental setup is as follows. The model was spun-up for 10 years with climatological forcing and then integrated with time dependent forcing for 1988-1998 in all the experiments. The assimilation began in July 1996. The initial conditions and the forcing were identical in all assimilation experiments. In addition to the data assimilation runs, a forced model integration without assimilation (referred to as the control) serves as a baseline for assessing the assimilation performance. The assimilation run with a simple univariate error covariance model is denoted UOI, the assimilation run with univariate error covariance model and salinity adjustment is denoted UOI+S. The run with the empirical multivariate forecast error covariance model is termed MvOI.

In every assimilation experiment, the daily-averaged subsurface temperature data from the TAO moorings were assimilated once a day. To alleviate the effects of the large shock on the model resulting from the intermittent assimilation of imperfectly balanced increments, the incremental update technique was used (Bloom et al. 1996). In this implementation, the assimilation increment is added gradually to the forecast fields at each time step.

5.2 Validation with independent data

The simulation (i.e., the control, with no assimilation) and three assimilation tests are cross-validated against the independent temperature, salinity and zonal velocity sections from Johnson et al. (2002). All of the available observed profiles are used and the statistics are separated corresponding to four regions: Niño 4 (160°E-150°W) and Niño 3 (150°W-90°W), further divided into two halves, north and south of the equator (5°S-0° and 0°-5°N) (Figure 2.2). The instrument error for temperature is 0.002°C, for salinity 0.003 and <0.05 ms^{-1} for zonal velocity.

To put the amplitude of the root-mean-squared difference (rmsd) in perspective, the mean monthly standard deviation (std) of the model is plotted as well. It is calculated using daily values at the same pre-defined depth levels on which the analyses are performed. The standard deviation represents the level of the internal variability in the model for the submonthly temporal scales which could in part be responsible for the errors in the monthly averaged profiles assessed against single synoptic ship observations. Also shown in temperature panels is the standard deviation of the daily TAO data that is used for assimilation. The data variability is substantially higher than that of the model, with standard deviation almost reaching 3°C in the thermocline in the Niño 4 region and exceeding this value in the Niño 3 region.

In general, the rmsd of the control quantities and the data is about twice as large as the model standard deviation and half the data standard deviation. The MvOI experiment shows comparable skill in temperature as the UOI with the greatest reduction in rmsd in the thermocline in the Niño 3 region south of the equator (Figures 5.1 and 5.2). Below 400 meters none of the assimilation schemes shows smaller rmsd than the control run due to the fact that data for assimilation are only available above 500 meters and at this level the observations are sparse, but the MvOI error is smaller north of the equator in both Niño 3 and Niño 4 regions. The transition region between the upper part of the water column where the temperature profile is corrected by the assimilation to the abyss where the data are absent may cause disruptions in the internal dynamic balances. While the model is attempting to reinstate them using available mixing tools, it is not able to fully preserve the temperature structure below the transition region, which is reflected in the larger rmsd

(top panels on Figures 5.1 and 5.2). Apparently the error covariance should have been calculated deeper to take care of this situation. The MvOI is able, however, to preserve the salinity structure very well in every region except south of the equator in the Niño 3 region. The MvOI current structure is also improved compared with the UOI everywhere, especially south of the equator. The UOI+S scheme, although quite successfully correcting the salinity, fails to estimate the current structure as well as the MvOI algorithm, indicating that the MvOI generates corrections that are more dynamically consistent than does either UOI implementation.

The two data sets discussed above describe the same quantity - temperature - yet they are based on different instruments and thus may not provide identical estimates of it. Part of the rmsd shown in Figures 5.1 and 5.2 is due to the mismatch of the measurements taken by TAO buoys and the CTDs of the TAO servicing cruises. To get a sense of how large this mismatch may be, the two data sets were scanned to identify co-located concurrent measurements and the mean difference and standard deviation of the difference were calculated. There are about 150 profiles that satisfy the colocation requirement (Figure 5.3). Mean and standard deviation of temperature differences, $T_{CTD} - T_{TAO}$ (subscripts identify the datasets), were calculated in the same regions as rmsd for the assimilation experiments and CTD data (Figure 5.4). The TAO temperature has a warm bias with respect to CTD data in the Niño 4 region north and south of the equator with a maximum of 0.4°C just above 200 m. The mean difference of the two datasets in Niño 3 region is smaller, TAO being warmer by about 0.1°C below 150 m north of the equator. The std of $T_{CTD} - T_{TAO}$ reaches 1°C in the thermocline which is about half as large as the rmsd between any of the assimilation schemes and the CTD data (Figures 5.1 and 5.2). We can view this difference as providing an indication of the observational error due to the representation error. Since the error std varies with depth, these estimates could be used to modify the simple implementation we chose here: the constant value of 0.5°C, which, as a first guess, is a good estimate of the error amplitude.

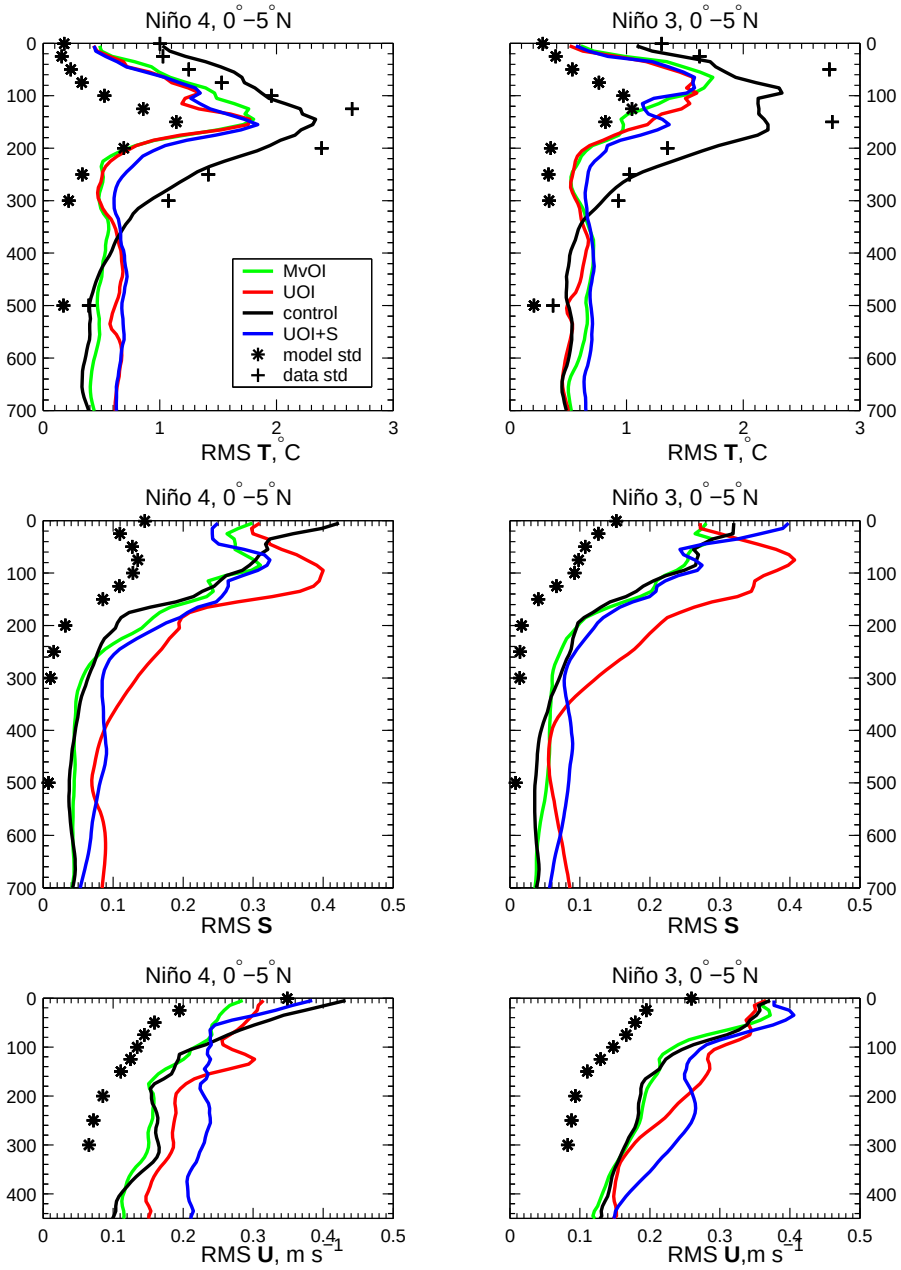

Figure 5.1: Rmsd between the four model runs (UOI, UOI+S, MvOI and control) and the observations as a function of depth (m) for the 35 transects. Statistics are grouped by Niño 4 (160°E-150°W) and Niño 3 (150°W-90°W) regions, and each area is further divided into two halves, south and north of the equator (0°-5°N shown here). Temperature rmsd (a-b), salinity rmsd (c-d) and zonal velocity rmsd (e-f) are shown. Mean monthly standard deviations of the corresponding model fields for the same regions are shown by stars. Data standard deviation is shown by crosses.

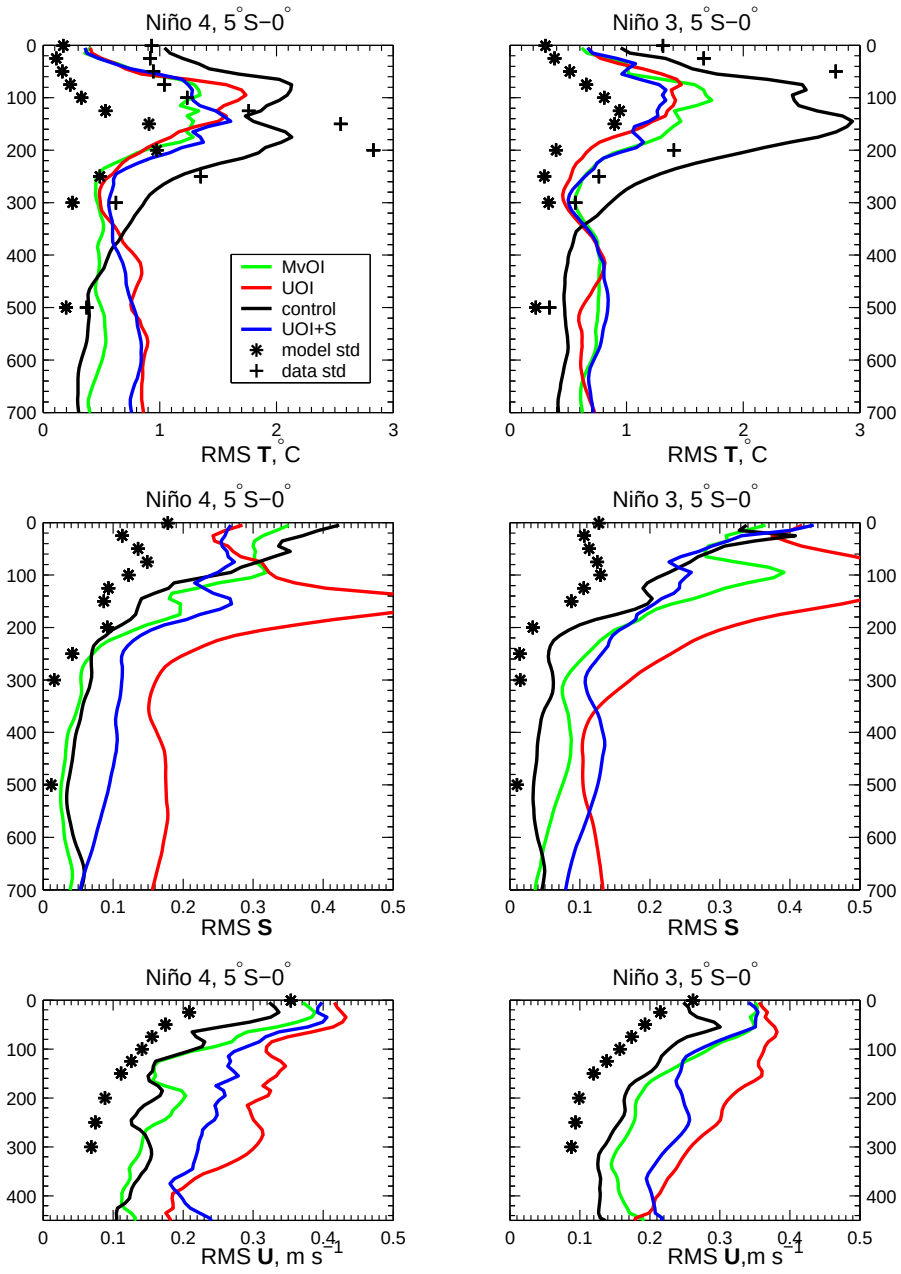

Figure 5.2: Rmsd between the four model runs (UOI, UOI+S, MvOI and control) and the observations as a function of depth (m) for the 35 transects. Statistics are grouped by Niño 4 (160°E-150°W) and Niño 3 (150°W-90°W) regions, and each area is further divided into two halves, south and north of the equator (5°S-° shown here). Temperature rmsd (a-b), salinity rmsd (c-d) and zonal velocity rmsd (e-f) are shown. Mean monthly standard deviations of the corresponding model fields for the same regions are shown by stars. Data standard deviation is shown by crosses.

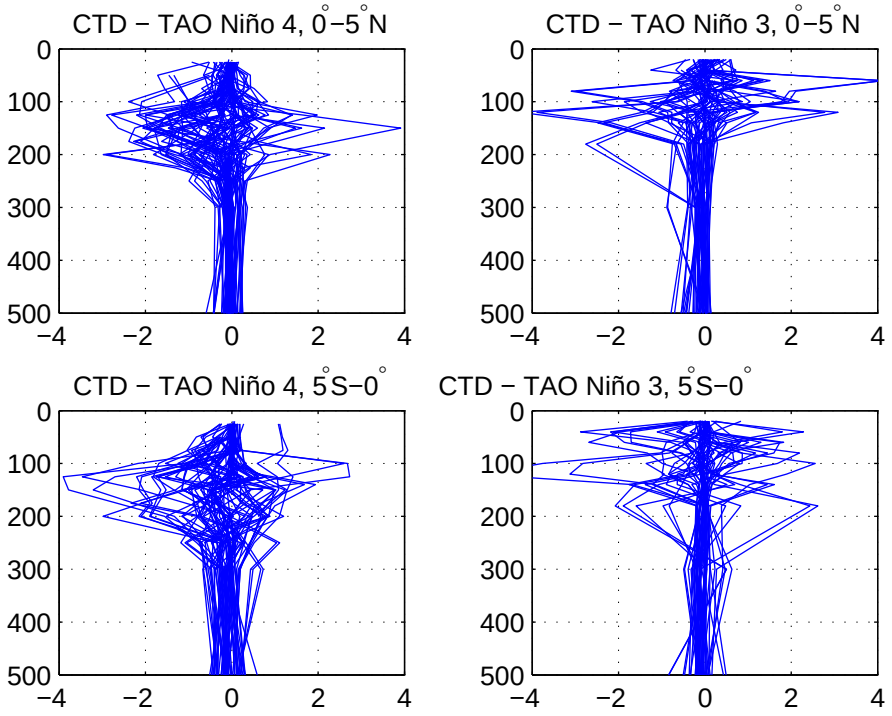

Figure 5.3: Difference profiles, $T_{CTD} - T_{TAO}$, grouped by Niño 4 (160°E-150°W) and Niño 3 (150°W-90°W) regions south and north of the equator.

5.3 Salinity deterioration

The UOI assimilation improves upon the control case in the representation of temperature, yet the investigation of other model fields, such as salinity, reveals potential problems in a long-term integration. To illustrate this, consider time series of the equatorial salinity, averaged between 2°S and 2°N at the thermocline depth compared to the observed salinity (Figure 5.5). In the UOI experiment, within 3-4 months the salinity structure deteriorates significantly. Poor performance of UOI is due to the fact that correcting the temperature field alone introduces artificial and potentially unstable water mass anomalies whose propagation and eventual strengthening destroys model dynamical balances. The UOI+S and MvOI schemes track salinity almost as well as the control experiment, which does remarkably well in this limited comparison.

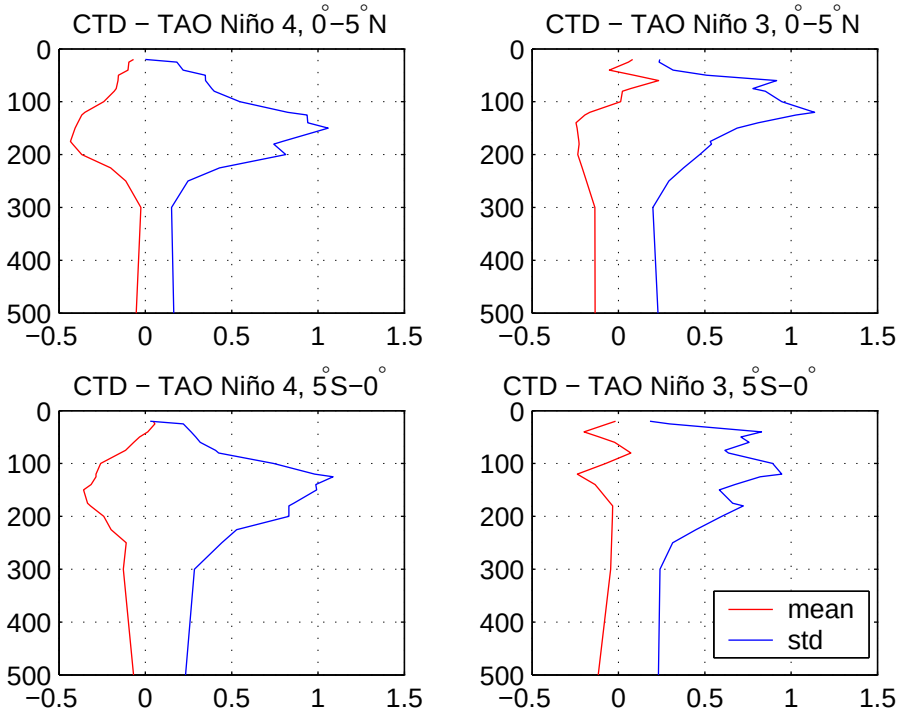

Figure 5.4: Mean difference and standard deviation of $T_{CTD} - T_{TAO}$ grouped by Niño 4 (160°E-150°W) and Niño 3 (150°W-90°W) regions south and north of the equator.

5.4 Water properties analysis

To test how well the assimilation schemes preserve the water mass properties - the basis of the Troccoli and Haines scheme, we consider the temperature-salinity (T-S) relationships in the same subregions as used above. T-S pairs at each observation are compared with model values interpolated to the same locations using a T-S grid of granularity 0.25°C by 0.1 (Figures 5.6-5.9). At least 5 T-S pairs must be found for a colored circle to be plotted to make sure that the features in the figures are robust. For a black dot to appear all of these values must be from a model simulation, for a cyan dot to be plotted all 5 must be observations, and for a red dot to appear there must be a total of at least 5 of either kind.

North and south of the equator in both Niño 3 and Niño 4 regions the model without assimilation (top panels) shows good representation of T-S except in the area of warmest water (cyan circles near the top of the plot) and somewhat in the representation of the dense cool saline water (few cyan circles below the main body of red color). The first deficiency is successfully

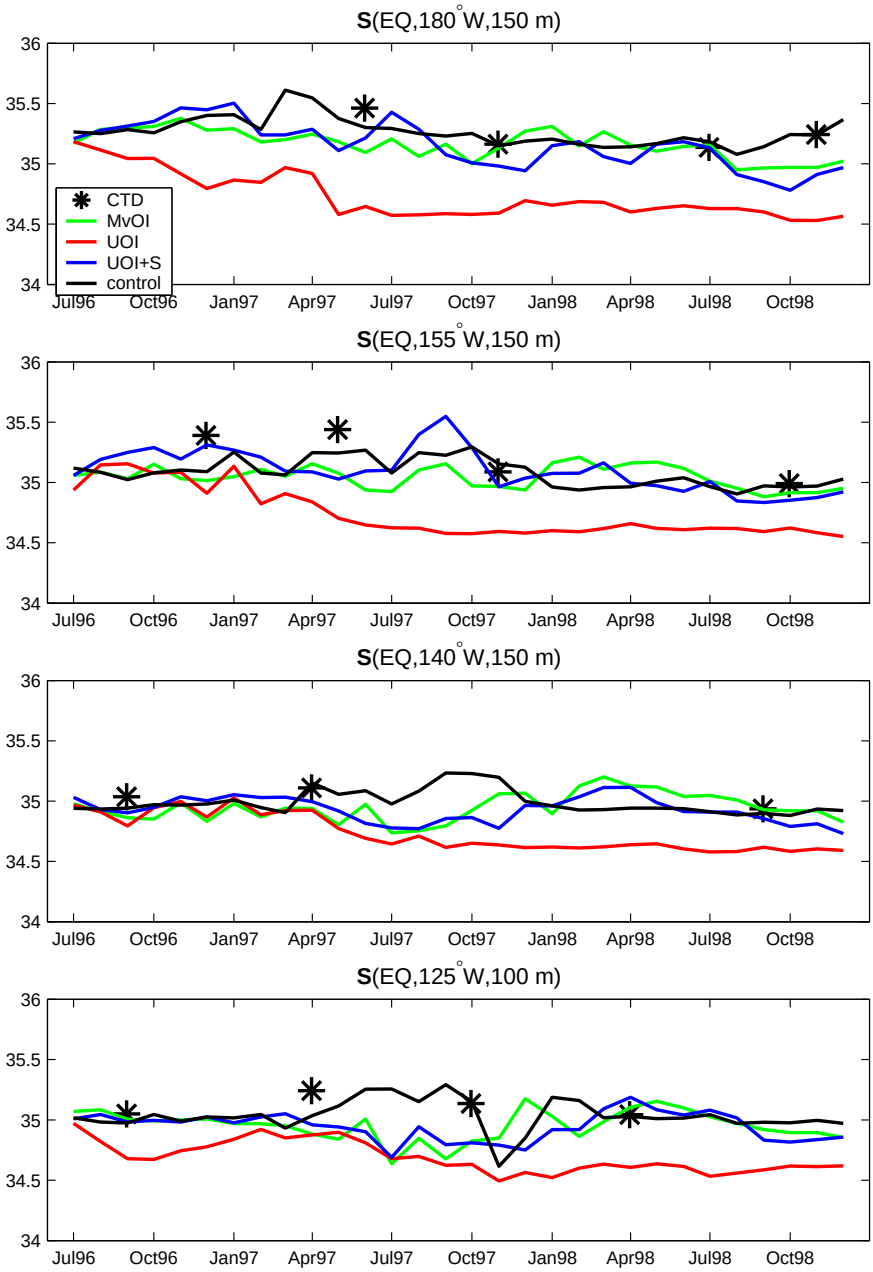

Figure 5.5: Salinity time series for the control, UOI, UOI+S and MvOI integrations. Values are averaged between 2°S-2°N at the specified longitudes. CTD observations are shown by stars where available.

corrected by the MvOI and to a lesser degree by the UOI. Some observed surface warm saline waters in the Niño 3 region north of the equator are not included in any of the model analyses, probably due to errors in surface forcing that the assimilation is not able to rectify. The problem of the lack of dense saline water in the model is slightly overcorrected by MvOI: all cyan circles change to red and some black circles appear in the Niño 3 region north and south of the equator and in the Niño 4 region south of the equator. The UOI scheme shows gross over-production of this type of water south of the equator and to a lesser degree in the north and it misses the more saline side of the distribution from anomalous density σ_θ of 22 to 26 kg m^{-3}, north of the equator as well as in the south. Thus, significant problems are apparent in the UOI scheme, while MvOI is able to improve upon the control over almost the entire range of the T-S diagram.

UOI+S relies on the model-derived water mass properties to correct the model salinity commensurate with the temperature corrections made by assimilating temperature observations. The salinity increments are calculated according to the temperature analysis by preserving the model's local column T-S relationship. Thus it is able to a certain degree to correct problems introduced by the UOI assimilation. This is evident from the appearance of red dots in place of cyan on the warm saline part of the T-S distribution. However it cannot completely alleviate the overproduction of the dense saline water by UOI (black dots on the lower right side of the T-S plots), since the limitation of UOI+S scheme is that it is designed solely for temperature observations and relies on the assimilation system maintaining a good T-S relationship and once this relationship altered, UOI+S algorithm cannot restore it. The scheme also assumes that the dominant source of variability (and error) is vertical movement of the water column.

5.5 Meridional cross-sections

Meridional cross-sections of the temperature, salinity and zonal velocity (Figures A.1-A.4, A.5-A.8 and A.9-A.12 for convenience shown in the appendix) are compared to a selection of sections prepared and presented in Johnson et al. (2000). The sections are chosen so that approximately simultaneous sections across the Pacific basin can be shown after a long period of

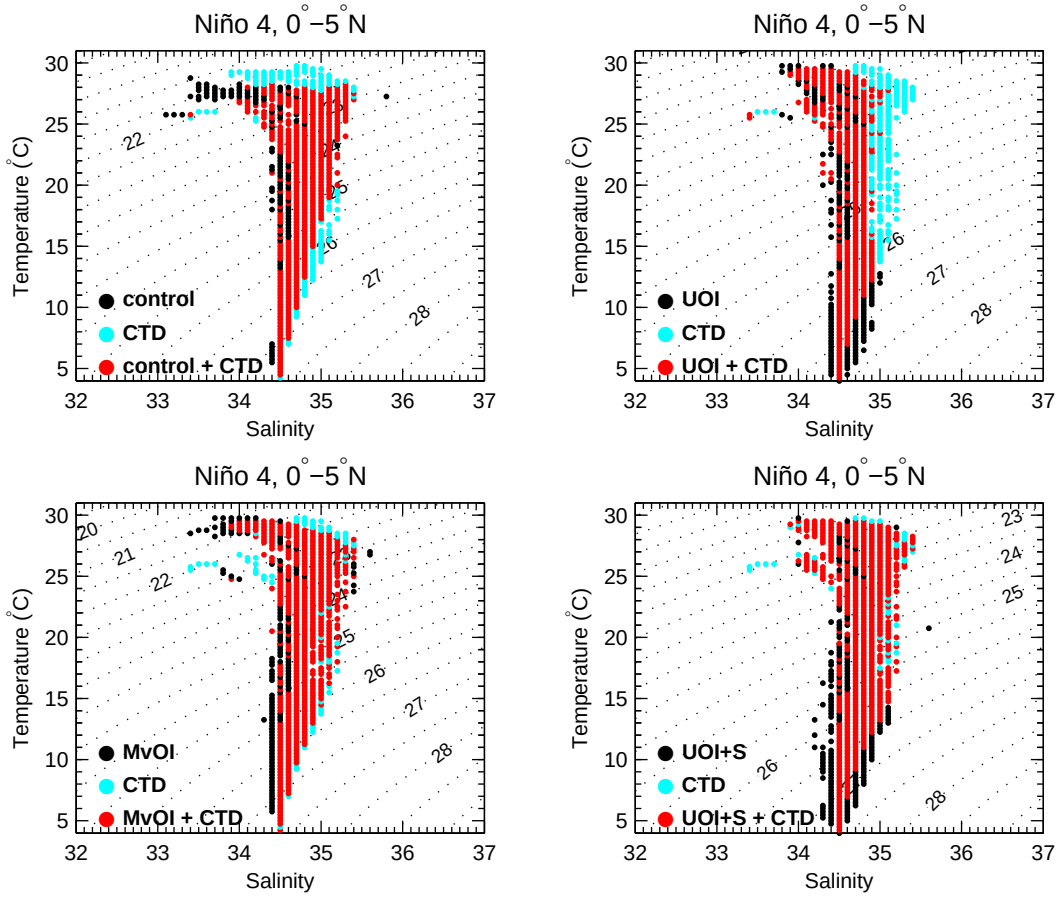

Figure 5.6: Temperature-Salinity diagram for UOI, UOI+S, MvOI and control experiments for the Niño 4 region north of the equator. The thin dashed lines show constant potential density for reference. Black dots are plotted for values present only in the model, cyan - only in observations and points where the model and observations agree are shown in red.

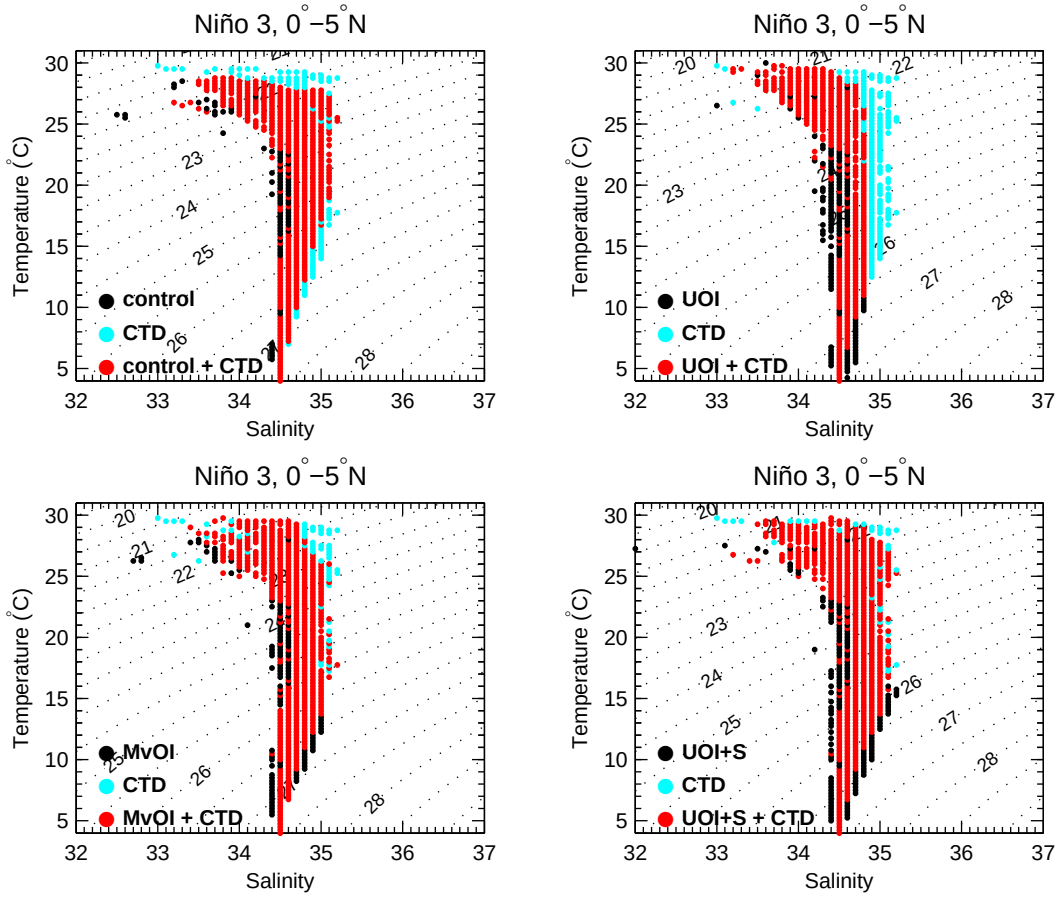

Figure 5.7: Temperature-Salinity diagram for UOI, UOI+S, MvOI and control experiments for the Niño 3 region north of the equator. The thin dashed lines show constant potential density for reference. Black dots are plotted for values present only in the model, cyan - only in observations and points where the model and observations agree are shown in red.

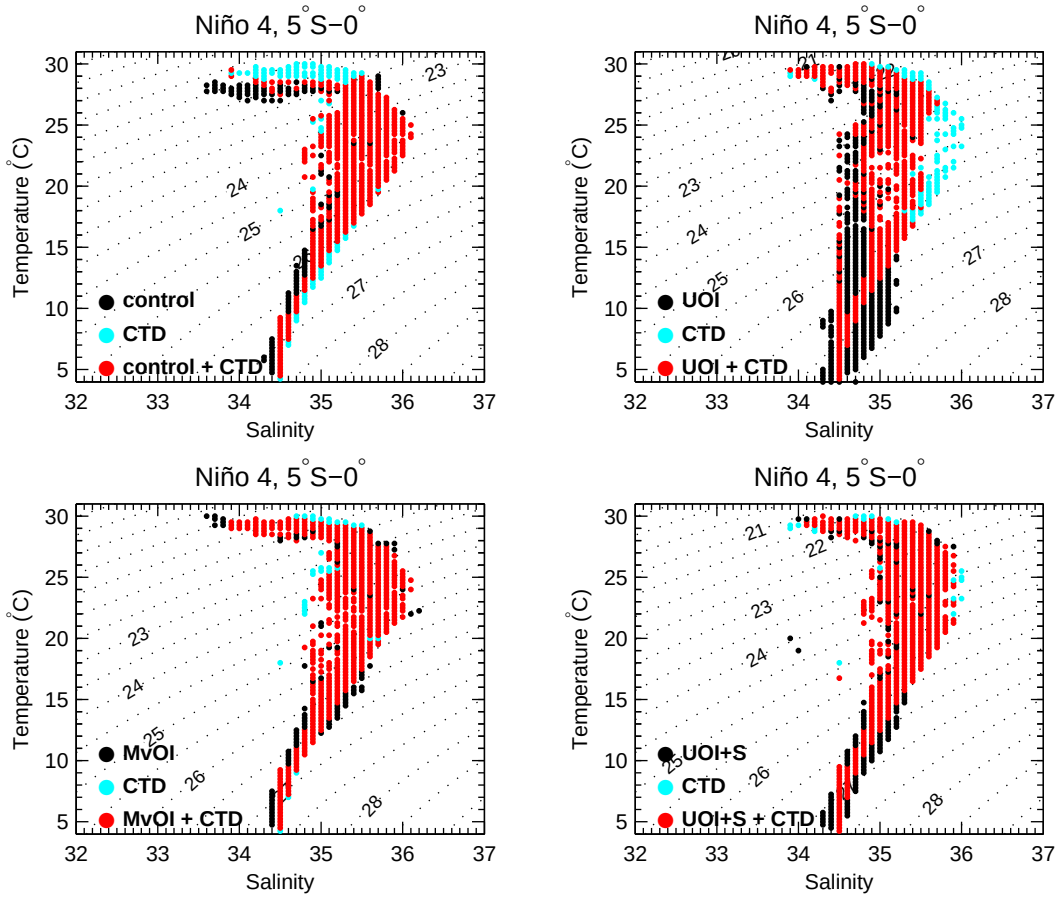

Figure 5.8: Temperature-Salinity diagram for UOI, UOI+S, MvOI and control experiments for the Niño 4 region south of the equator. The thin dashed lines show constant potential density for reference. Black dots are plotted for values present only in the model, cyan - only in observations and points where the model and observations agree are shown in red.

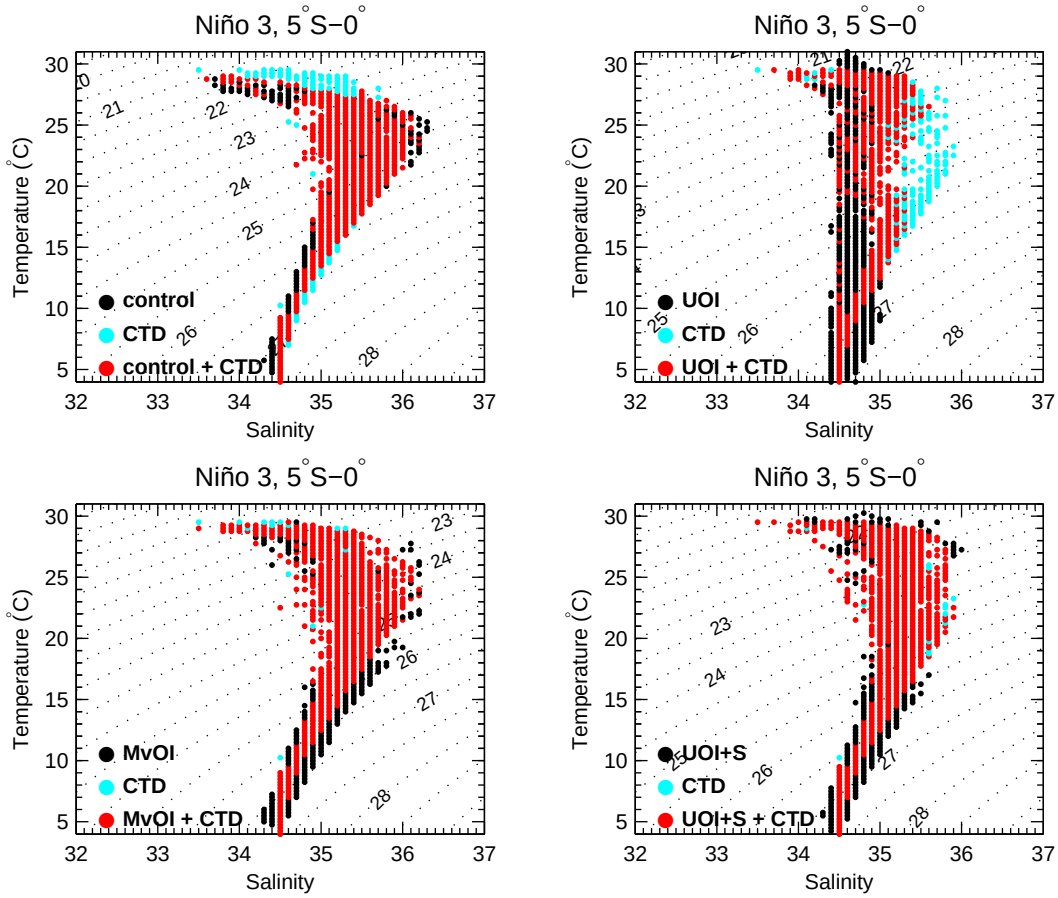

Figure 5.9: Temperature-Salinity diagram for UOI, UOI+S, MvOI and control experiments for the Niño 3 region south of the equator. The thin dashed lines show constant potential density for reference. Black dots are plotted for values present only in the model, cyan - only in observations and points where the model and observations agree are shown in red.

integration (about 2 years). These sections are included in the rmsd statistics of Figures 5.1 and 5.2. The MvOI experiment discussed in the previous sections is labeled MvOI$_T$ in these figures to distinguish it from the two additional MvOI experiments which will be discussed later.

The temperature in the UOI experiment is an improvement over the control, while the salinity structure in the UOI has little resemblance to data. The UOI+S temperature, while in general better than the control exaggerates off-equatorial features: the upward penetration of the cold waters is too sharp and too shallow. The model by itself is capable of producing good salinity and current fields. The UOI salinity cross sections display no penetration of the saline waters from the south across the equator. The salinity close to the equator is too low and there is an erroneous deep extension of high salinity around 8°S in the eastern basin. The UOI+S is able to take advantage of the model's good salinity reproducibility and its salinity field is a marked improvement over the UOI, especially at 180°W. At 125°W the near surface structure is good but there is also an unrealistic deep extension of high salinity south of the equator. The MvOI$_T$ salinity cross-sections are closer to the observations, although the salinity near the surface at 165°E north of the equator is somewhat low and the region of high salinity values at 180°W south of the equator is too wide. The MvOI$_T$ zonal current is the closest to the observed in the western and eastern Pacific with a better representation of the deeper subsurface maxima and a surfacing of the undercurrent at 165°E. The UOI currents reach too deep. The UOI+S currents are well represented at the maxima but extend too deep along the equator in every profile except 125°W where the maximum is too close to the surface. At the dateline the current structure in MvOI$_T$ is exaggerated compared to observed but the secondary subsurface maximum at about 4°N (the northern subsurface countercurrent) is captured in the assimilation. The UOI currents are again too weak, particularly at the equator and reach too deep south of the equator. It is apparent from these figures that the MvOI$_T$ corrects the current structure on and close to the equator better than the statistics of Figures 5.1 and 5.2 might suggest.

5.6 Equatorial variability

As was seen above from the water properties analysis and from inspection of the meridional cross-sections, the control experiment is capable of producing good salinity and velocity fields. UOI, while correcting the subsurface temperature, destroys the salinity and currents structure. UOI+S, attempting to preserve the T-S relationship, nonetheless cannot make a completely dynamically consistent correction of the entire ocean state vector. MvOI, making the least disruption to the balanced state, brings it closer to the observations. Figures 5.10-5.12 show the mean difference and the standard deviation of UOI, UOI+S and MvOI states with respect to the control, over the length of the integration (2.5 years) along the equator. While the temperature mean difference with the control is comparable in all three experiments and the distribution of std is similar, the picture in salinity is quite different. MvOI differs the least from the control, while the UOI creates a huge (up to 0.6) fresh bias along the equator, especially in the west. UOI+S is in between, closer to MvOI than UOI. In zonal velocity the mean difference between UOI+S and control is similar to that of UOI and control. MvOI again, by making more dynamically consistent correstions at each analysis, makes the least disturbance to balances and preserves the velocity structure.

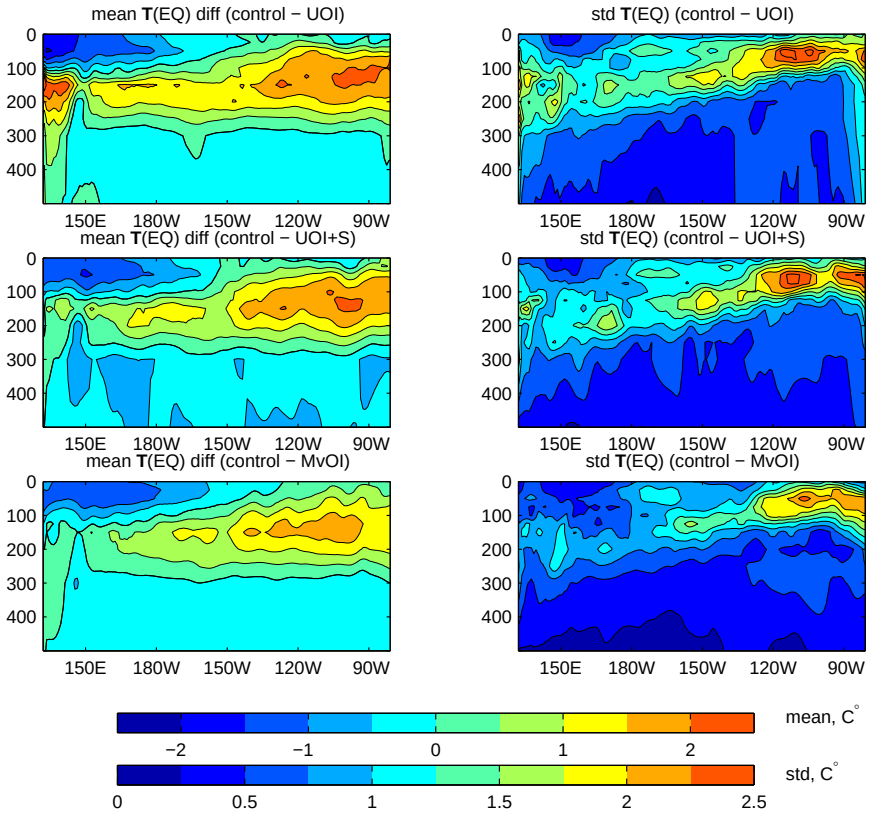

Figure 5.10: Mean difference in temperature between control and assimilation experiments UOI, UOI+S and MvOI averaged over 2.5 years (left) and standard deviation (right) between the same experiments. Equatorial cross sections are shown. The contour interval is 0.5°C for the mean and 0.25°C for standard deviation.

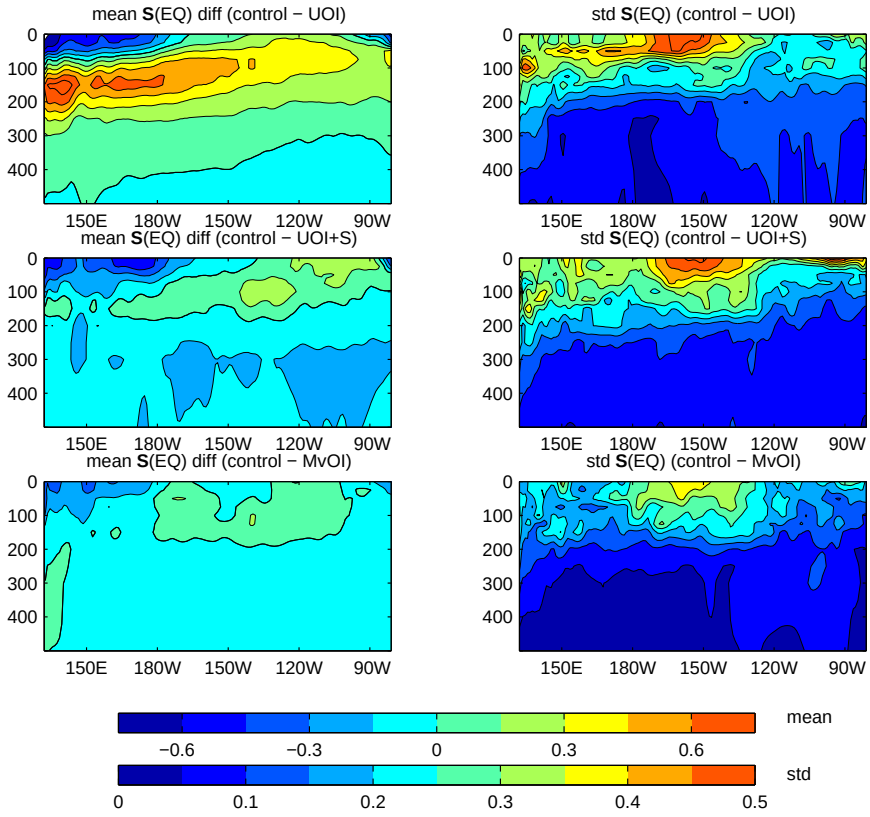

Figure 5.11: Mean difference in salinity between control and assimilation experiments UOI, UOI+S and MvOI averaged over 2.5 years (left) and standard deviation (right) between the same experiments. Equatorial cross sections are shown. The contour interval is 0.15 for the mean and 0.05 for standard deviation.

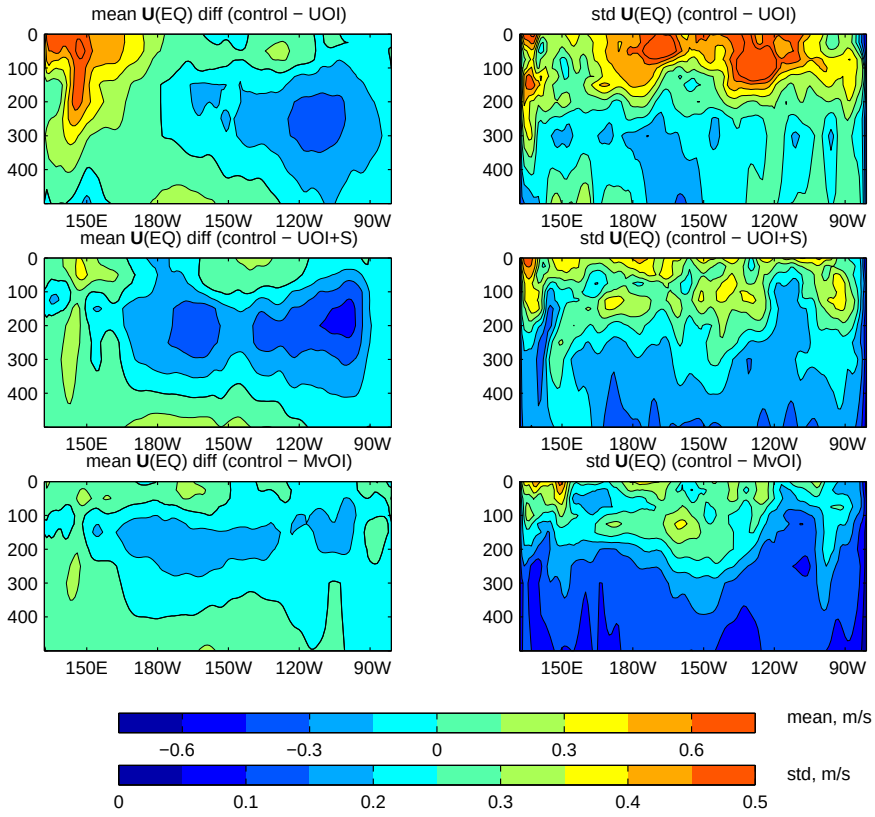

Figure 5.12: Mean difference in zonal velocity between control and assimilation experiments UOI, UOI+S and MvOI averaged over 2.5 years (left) and standard deviation (right) between the same experiments. Equatorial cross sections are shown. The contour interval is 0.15 ms^{-1} for the mean and 0.05 ms^{-1} for standard deviation.

Chapter 6

Analysis Uncertainty

6.1 Ensemble of MvOI experiments

In order to assess the uncertainty and reliability of the MvOI assimilation performance and establish a metric for the evaluation of various modifications to the EOF basis used for the forecast error covariance models, the MvOI experiment was repeated with every one of the 10 available realizations of the forecast error covariance matrix. The procedure to obtain these matrices (sets of EOFs) is described earlier in Section 4.1. The combinations of years for each set of EOFs is listed in table 6.1. The MvOI experiment discussed in Chapter 5 happened to be number 5 on this list.

Table 6.1: List of years included in each realization of the **P** matrix.

exp1	1979	1980	1981	1990	1991
exp2	1979	1982	1985	1988	1991
exp3	1979	1986	1988	1990	1992
exp4	1980	1982	1985	1987	1989
exp5	1980	1983	1986	1989	1992
exp6	1981	1982	1985	1986	1989
exp7	1982	1984	1985	1986	1989
exp8	1982	1984	1986	1989	1991
exp9	1983	1984	1990	1991	1992
exp10	1983	1987	1991	1992	1993

The calculation of rmsd statistics shown in Figures 5.1 and 5.2 has been repeated for each of the 10 MvOI experiments. Figures 6.1 and 6.2 are identical to 5.1 and 5.2, but instead of a

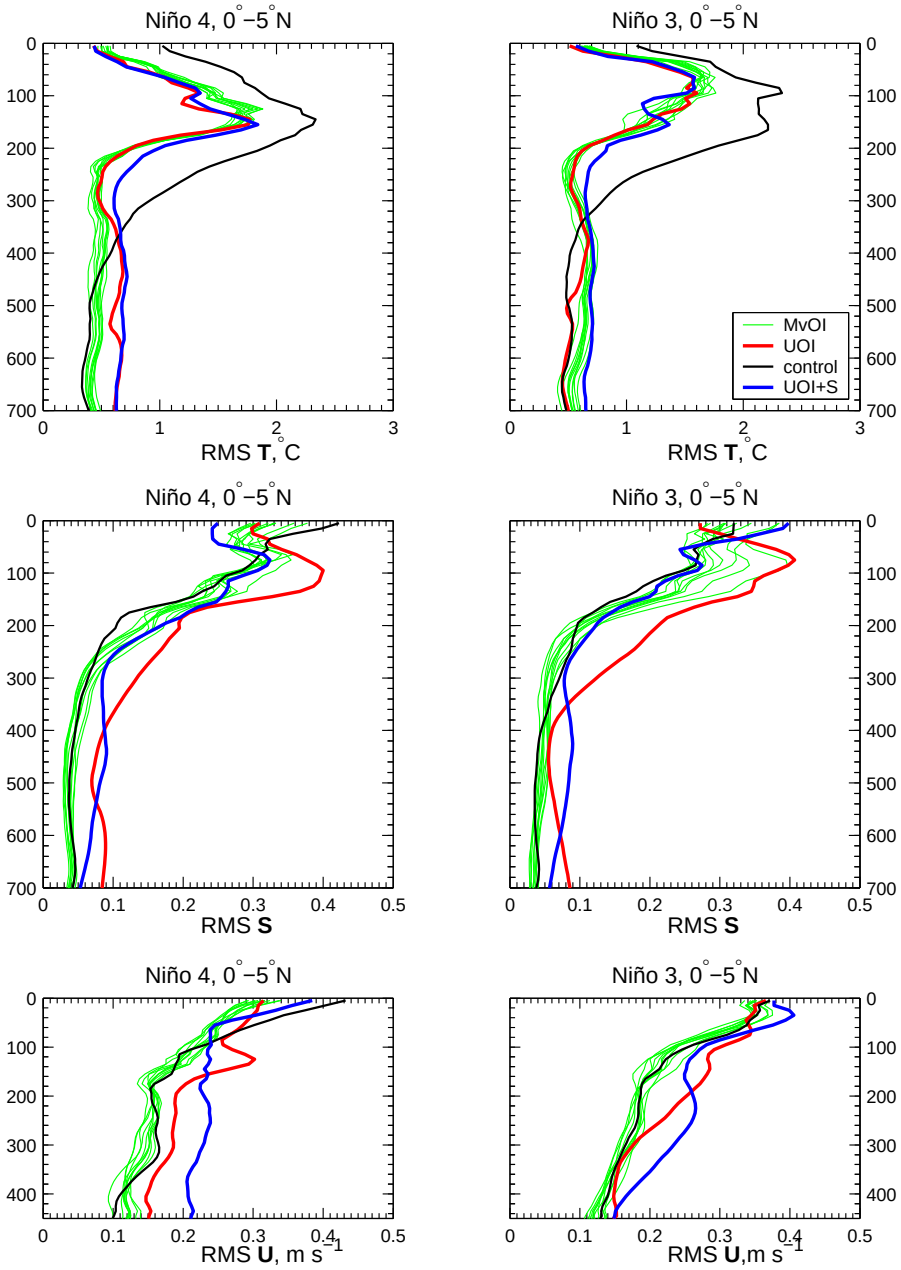

Figure 6.1: Rmsd between 10 MvOI runs differing by the EOF realizations and the observations as a function of depth (m) for the 35 transects. Statistics are grouped by Niño 4 (160°E-150°W) and Niño 3 (150°W-90°W) regions, and each area is further divided into two halves, south and north of the equator (0°-5°N shown here). Temperature rmsd (a-b), salinity rmsd (c-d) and zonal velocity rmsd (e-f) are shown.

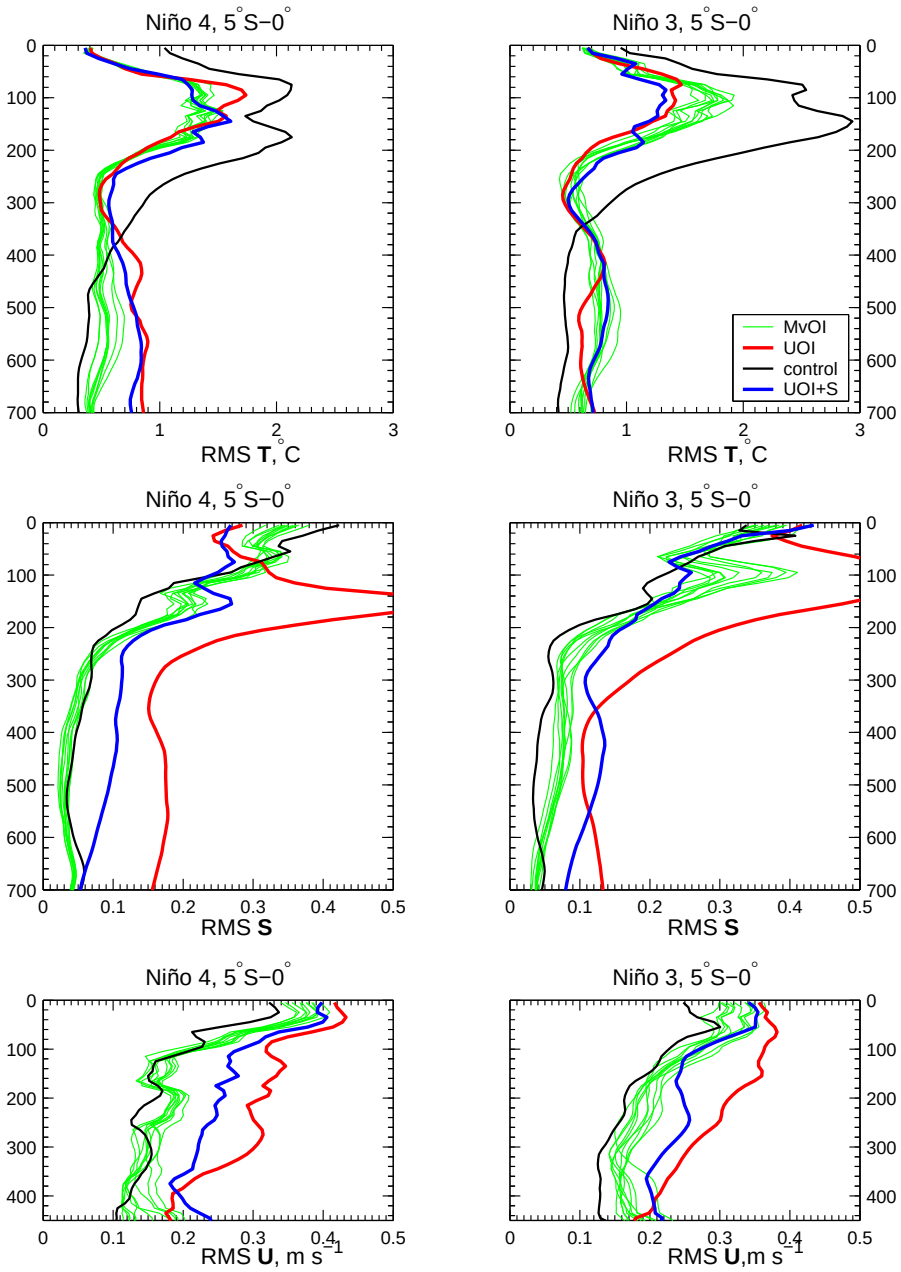

Figure 6.2: Rmsd between 10 MvOI runs differing by the EOF realizations and the observations as a function of depth (m) for the 35 transects. Statistics are grouped by Niño 4 (160°E-150°W) and Niño 3 (150°W-90°W) regions, and each area is further divided into two halves, south and north of the equator (5°S-0° shown here). Temperature rmsd (a-b), salinity rmsd (c-d) and zonal velocity rmsd (e-f) are shown.

single MvOI line there are 10 thin lines for different experiments. The performance of all MvOI assimilations is similar when compared to other assimilation schemes. However there is noticeable spread within this 10-member ensemble of runs, especially manifest in salinity in the Niño 3 region, both north and south of the equator. The rmsd curves in temperature and velocity tend to tightly bunch together north of the equator and a little less so south of the equator in both Niño 3 and Niño 4 regions.

Such uneven distribution of the rmsd statistics between different variables may be related to the differences in the underlying covariance structure, since, as evident from Figures 4.1 and 6.3, the T-T decorrelation curves are much closer to each other than the T-S decorrelation curves. Thus the analyses produced by MvOI with different $\mathbf{P}$ matrices are more similar in temperature than in salinity. The T-U decorrelation curves (not shown) are more similar to each other that T-S curves with the exception of the far eastern equatorial Pacific.

6.2 Variability across the MvOI ensembles

The variability across the ensemble of MvOI experiments is investigated next. Below, each member of this ensemble is compared to the ensemble mean (referred to as mean(10)). Figures 6.4, 6.5, 6.6 show the mean anomalies averaged over 30 months for temperature, salinity and zonal velocity, respectively, and Figure 6.7 shows mean standard deviations with respect to the same mean over the same time period. All calculations are based on the monthly average of model quantities. The labeling of the experiments corresponds to that in table 6.1.

Upon examining Figure 6.4 one can see that exp1 shows the largest deviation from the ensemble mean, the negative anomaly at 150 m near 150°W, reaches 0.5°C and it is the only member that has a positive anomaly in the western Pacific near between 300 m and 200 m. The negative anomaly at 150 m near 150°E is also strong relative to the other members. Exp2 has a relatively strong negative anomaly along the thermocline across the entire equatorial section. Exp3 has a strong positive anomaly up to 0.3°C in the far east between 300 m and 100 m, this feature is unique among the ensemble members. Exp4 shows a weak negative anomaly at the same

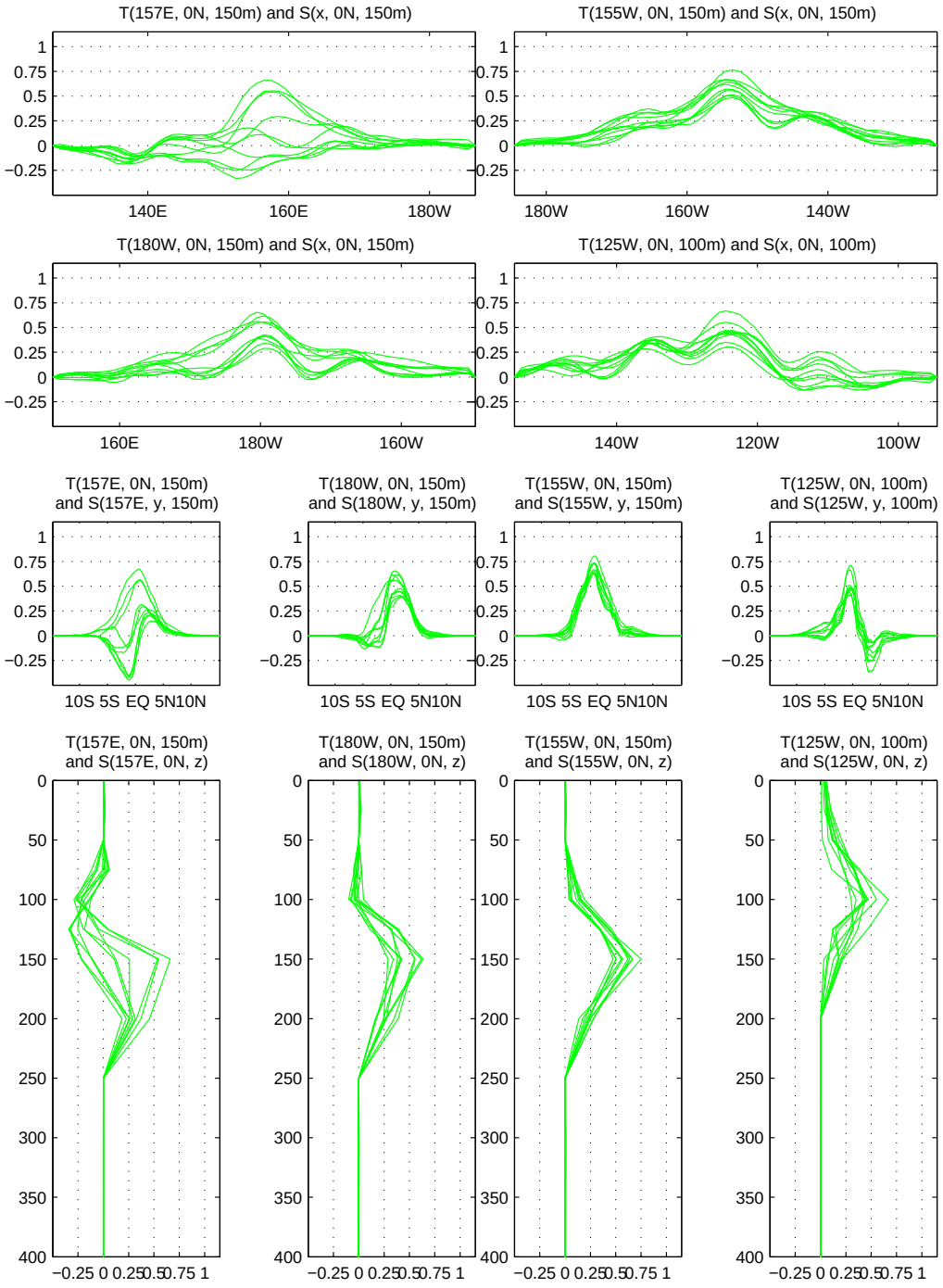

Figure 6.3: One-dimensional temperature-salinity decorrelation curves (zonal, meridional and vertical directions) corresponding to simulated observation at the specified locations. Each thin green line is produced by a different realization of the error covariance matrix. Compact support is applied as described in Section 3.3.2.

location. Exp5, exp9 and exp10 have a negative anomaly in the eastern part of the equatorial section east of 120°W extending from about 100 m to at least 500 m. Exp10 has a positive anomaly extending from the dateline to approximately 90°W along the thermocline. Overall exp4-exp9 differ less from the mean than exp1-exp3 and exp10 and the differences have smaller spatial scales and amplitude. The temperature standard deviation (std) structure (Figure 6.7) is similar for all ensemble members and shows a maximum amplitude of about 0.5°C: the largest variability is usually in the thermocline in the Niño 3 region with a second maximum in the western equatorial Pacific, also in the thermocline.

Salinity intra-ensemble variability is similar to temperature variability in the sense that exp1 clearly stands out from other nine MvOI experiments: it has the largest positive difference from the mean and the highest std values extending from the surface to below 200 m over the entire western and central equatorial section. Exp3 has a positive salinity anomaly in the far eastern part of the equatorial section where the positive temperature anomaly is located and similarly exp5, exp9 and exp10 have negative salinity anomalies in the east approximately co-located with the negative temperature anomaly. Exp2 and exp3 have positive anomalies near the surface in western and central equatorial regions and exp8 has an extensive negative salinity anomaly across most of the equator extending from the surface down to about 300 m in the west and shoaling to less than 100 m in the east. Salinity std patterns are similar across the ensemble (mean std is shown in Figure 6.7): variability is higher in the upper 200 m, with amplitudes rarely exceeding 0.1.

The mean zonal velocity anomaly is also the largest for exp1. Exp3 shows a similar distribution in the positive anomaly with the exception of a positive maximum near the surface around 150°E. Exp5 and exp9 have negative anomalies centered at 120°W extending from the surface to about 100 m. Exp6-exp8 have negative anomalies spread from west to east below 100 m. Standard deviation patterns (Figure 6.7) show the highest levels of variability near the surface. The maxima are located at 150°E and 120°W at the surface. A common feature to most experiments is higher std at 90°W at about 150 m; the amplitude of these maxima range from 0.1 ms^{-1} to 0.2 ms^{-1}.

To put these values in perspective, compare them to temporal mean difference and std

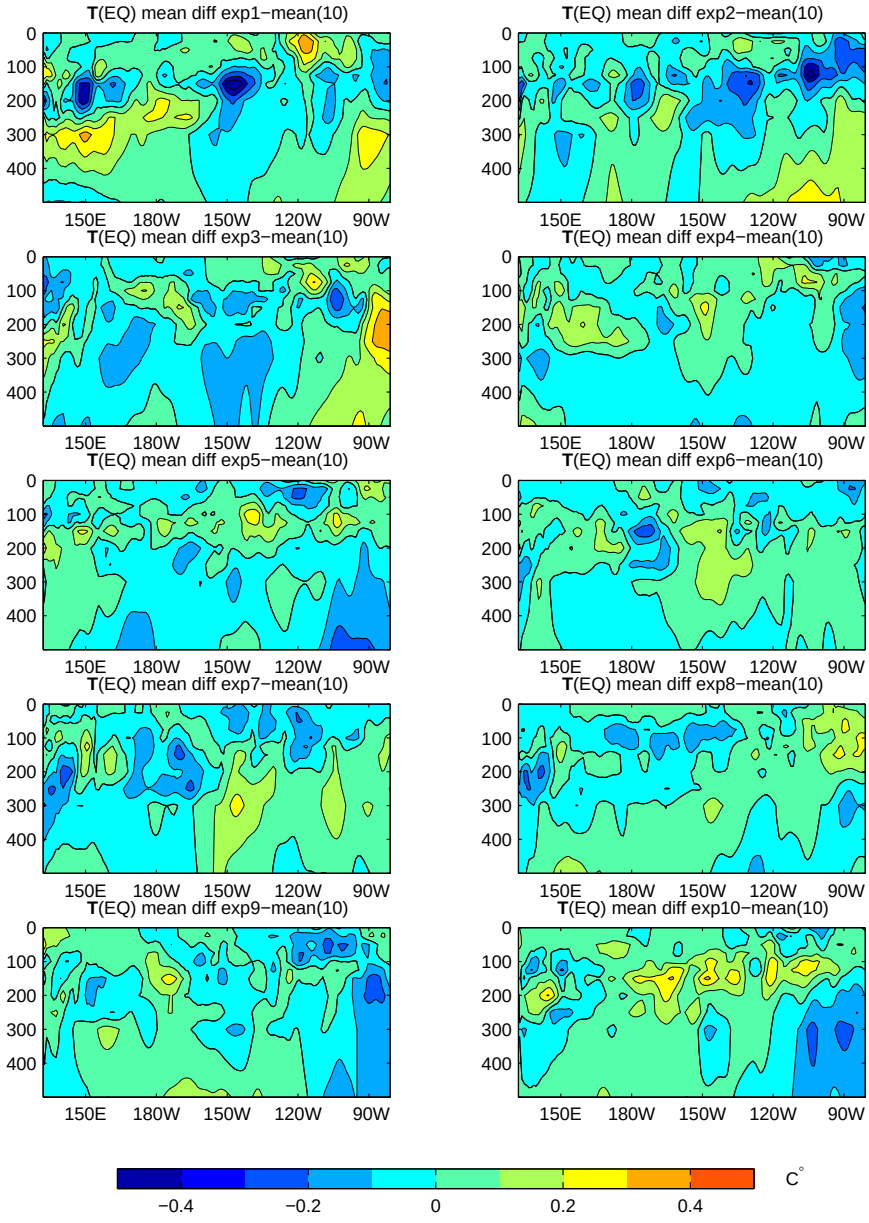

Figure 6.4: Mean temperature anomaly of each of the 10 MvOI experiments with respect to the mean of the ensemble of 10 runs averaged over 2.5 years. Equatorial cross-sections are shown. Contour interval is 0.1°C.

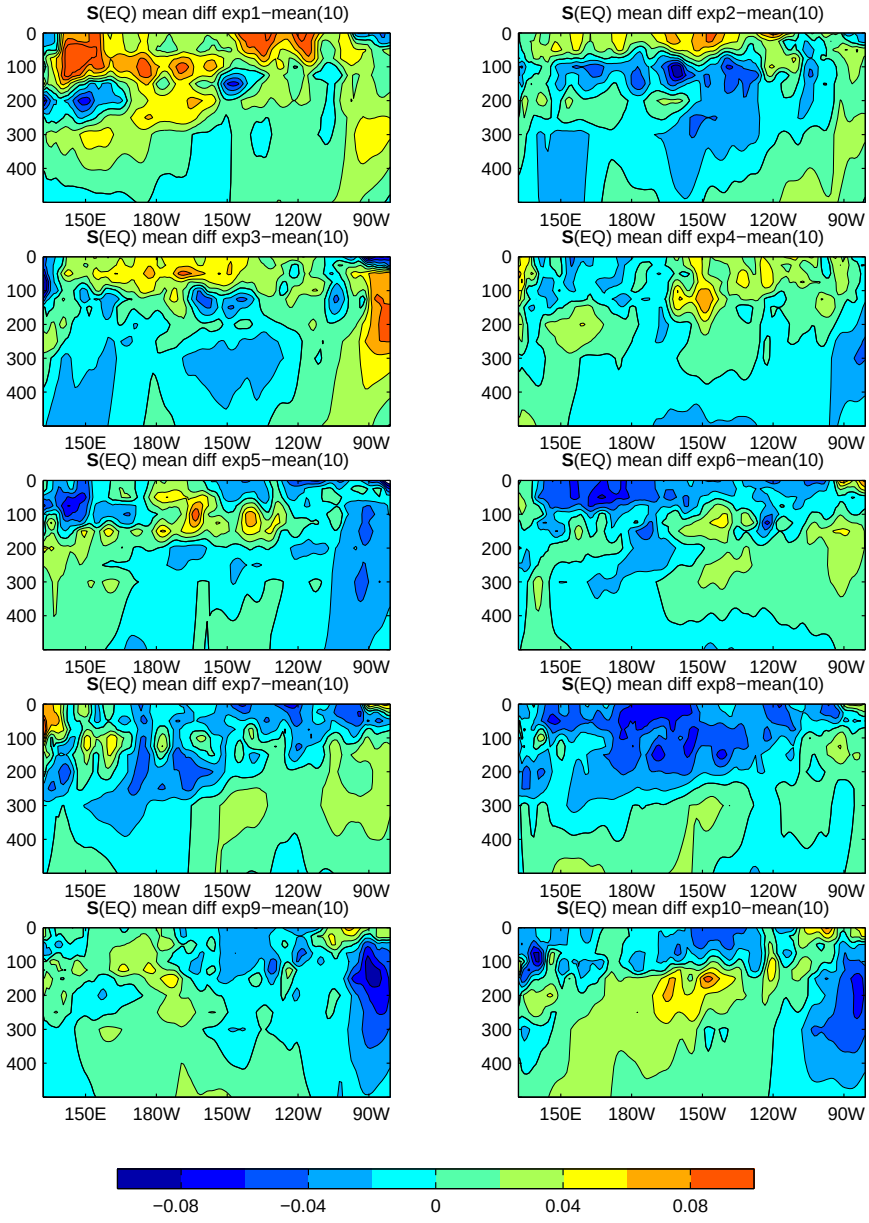

Figure 6.5: Mean salinity anomaly of each of the 10 MvOI experiments with respect to the mean of the ensemble of 10 runs averaged over 2.5 years. Equatorial cross-sections are shown. Contour interval is 0.02.

of the various assimilation analyses with respect to the control run, which are shown in Section 5.6 (Figures 5.10-5.12). In general, the std within the MvOI ensemble is only 20-25% of the std between the different assimilation schemes.

6.3 Probable causes for differences in forecast error structure

An important characteristic of the forecast error matrix **P** is its trace - the sum of the eigenvalues, that is the total variance. The top left panel of Figure 6.8 shows this quantity, converted to mean pointwise standard deviation, for every MvOI experiment listed in the table 6.1 in the same order. The dark solid line indicates the mean of all std's and the shaded region is the 95% confidence interval. Clearly the exp1 has the lowest variability. This is due to the fact that this realization of **P** is derived from the states selected early in the integration (1979, 1980, 1981), which means that the ensemble has smaller spread and the level of variance hasn't yet saturated. It is likely the co-variability patterns haven't approached their asymptotic state either. Since the states assembled into the large ensemble date to the first pentad of January, the year 1979 - the beginning of the integration - should have been left out of the calculation altogether. The **P** matrix of exp10 contains states from the latest three years of ensemble integration, which may partially explain why it has the highest total variance.

Another possible contributor to the differences in the variance and co-variance structures among the 10 MvOI experiments is interannual variability. Although the duration of ensemble integration - 15 years - is not very long, there have been several cold and warm events in the equatorial Pacific ocean during this period that may have influenced the error covariance distribution. Table 6.2 lists cold, neutral and warm phases of the El Niño Southern Oscillation (ENSO) based on the Japan Meteorological Agency (JMA) index, which is a 5-month running mean of the spatially averaged sea surface temperature anomalies over the tropical Pacific: 4°S-4°N, 150°W-90°W. To more directly relate the forecast error variance and ENSO phases the variance is calculated separately for each component (temperature, salinity, zonal and meridional velocities and sea surface height) of the state vector over the same region as JMA index. These values are also shown in

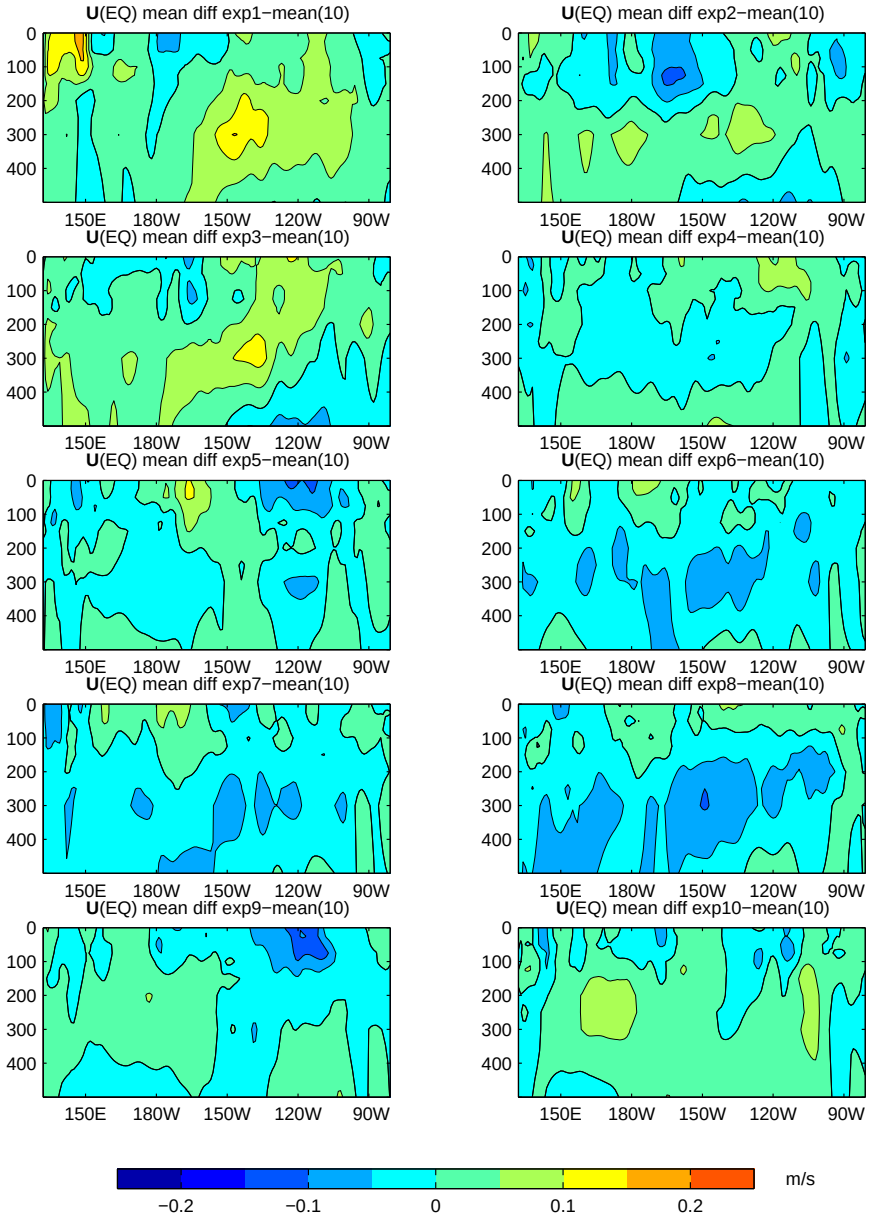

Figure 6.6: Mean zonal velocity anomaly of each of the 10 MvOI experiments with respect to the mean of the ensemble of 10 runs averaged over 2.5 years. Equatorial cross-sections are shown. Contour interval is 0.05ms^{-1}.

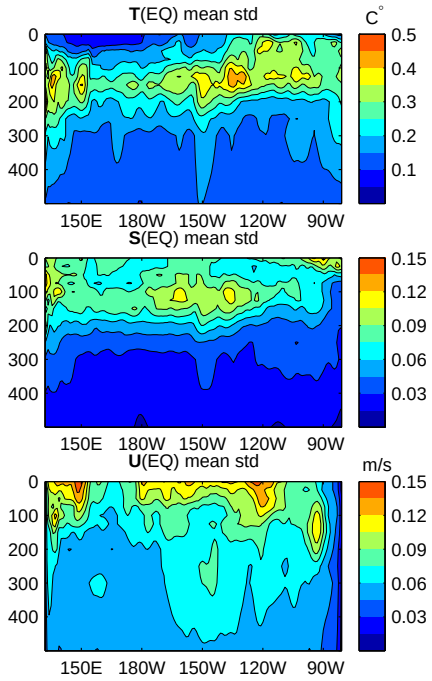

Figure 6.7: Mean temporal standard deviation of anomalies used for Figures 6.4-6.6, averaged over 10 MvOI. Equatorial cross-sections are shown.

Figure 6.8. Interestingly, not only do the levels of total variability differ between experiments but also the relative amplitude of variability varies between different components of the state vector, i.e., one experiment may have low variance in currents and high in temperature and salinity (for example, exp4) while another has relatively low variance in all components except sea surface height (exp5).

Comparing the two tables one can see that exp10 contains three warm years, exp9 and exp3 have two warm years each, as well as exp5, which also has the only cold year (1989, taking into account that the error covariances were computed based on a January date, thus the cold year 1988 from the table 6.2 corresponds to 1989 from the table 6.1). Exp2 and exp4 have one warm year and exp6, exp7 and exp8 have one cold year each.

Exp6 and exp7 exhibit similar levels of variability, and they differ by only one year (1981 in exp6, 1984 in exp7, the other four years coincide). Yet exp7 and exp8, which also have four common years differ significantly in the level of variance, especially in U, V and ssh. Exp7 has year 1985 while exp8 has year 1991. The year 1991 is also contained in exp9 and exp10, which exhibit

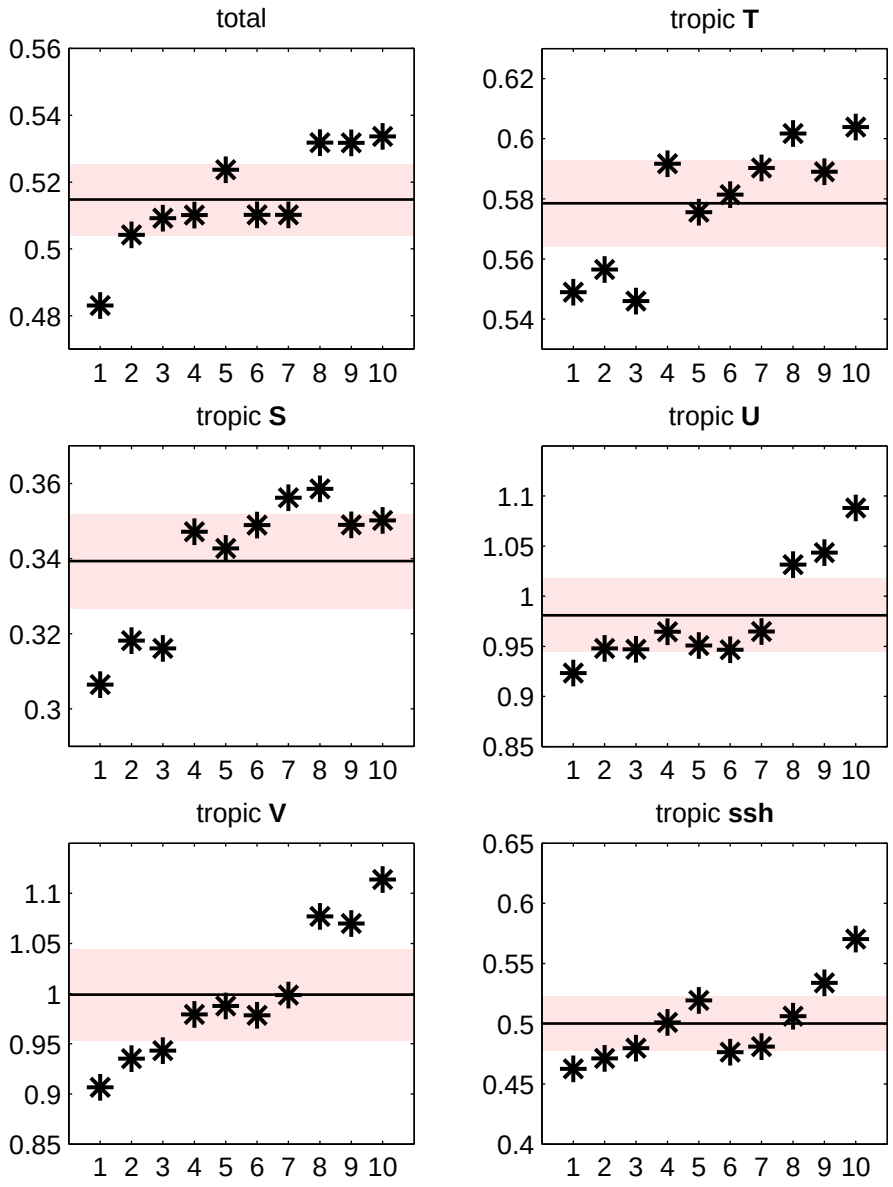

Figure 6.8: Top left panel: standard deviation for each of the 10 realizations of matrix $\mathbf{P}$. Other panels: standard deviation for each variable within the equatorial region (4°S-4°N, 150°W-90°W). The experiments are indexed along the horizontal axis in the same order as in table 6.1. The units along the vertical axis are non-dimensional. The solid black line shows the mean and the shading the 95% confidence intervals on the mean.

high variability in currents and ssh. Exp2, exp4, exp6 and exp7 are similar is that they tend to have higher std in temperature and salinity and lower std in zonal and meridional velocities. All these experiments have a pair (1982, 1985) in their composition, thus it can be suggested that these years have particular signature in the forecast error structure, as well as the year 1991. Exp5 and exp9 both contain warm years 1983, 1992 and they tend to have lower std in temperature and salinity. This is applicable to exp3 also, which contains year 1992.

The highest standard deviation is observed in exp10 in every variable due to several factors: this experiment has the year 1991 which is associated with high level of variability and its states are drawn from the last three years of integration (by this time the ensemble had the largest divergence).

Table 6.2: El Niño, La Niña and neutral years during the period of ensemble integration. The years in each category correspond to the first three months of the ENSO year namely October, November, and December. For example, the ENSO year 1970 starts October 1970 and ends September 1971 (*http://www.coaps.fsu.edu/products/jma_index.php*).

Cold phase	Neutral phase	Warm phase
	1979-1981	1982
	1983	
	1984	
	1985	1986
		1987
1988	1989	
	1990	1991
	1992-1993	

The standard deviations plotted in Figure 6.8 are for large ensembles derived from model ocean states assembled from 5 different years. However it is informative to analyze the standard deviation across an ensemble of states for separate years. Figure 6.9 shows the mean pointwise

standard deviation for each variable within the tropical region across the 32 ensemble members described in section 3.3.1. These standard deviation curves confirm that the ensemble of simultaneously integrated states has saturated the temperature variance of the ensemble in the tropics after about three years of integration. Some of the other variables seem to take slightly longer to saturate. However, this appearance may be artificial because of the slight tendency to lower variability during warm events. There is no clear relationship between the ENSO phases and the level of intra-ensemble variability, although one might observe that out of five warm years three show somewhat lower std than the neutral years. It may be speculated that the El Niño mode dominated during these years so that the suite of atmospheric states used to generate surface boundary conditions for different ocean ensemble members responded in unison to this signal and thus was less random than during neutral years.

In conclusion, the size of the sample doesn't allow us to establish a robust relationship between the ENSO phases and the forecast error variability, however some correlation between the interannual variability and the amplitude of forecast error standard deviation can be detected.

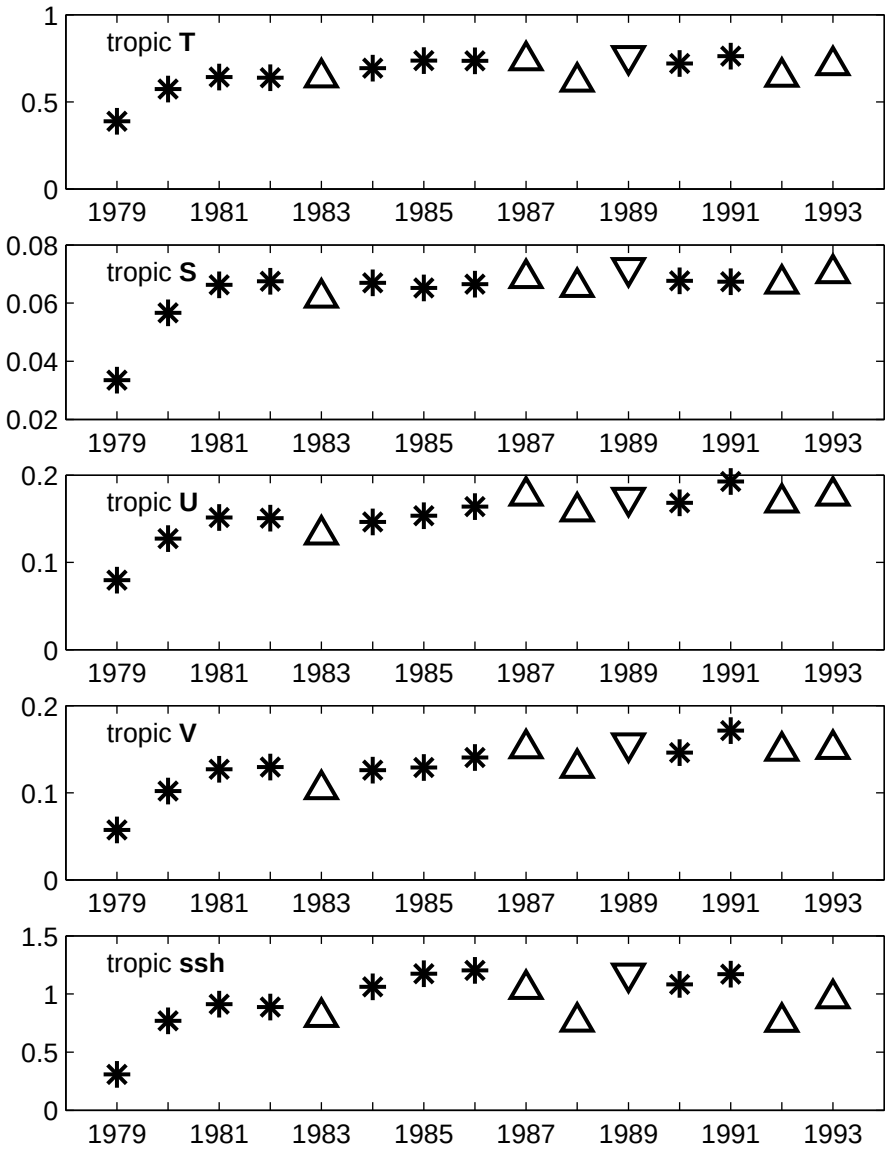

Figure 6.9: Standard deviation across the ensemble of 32 runs as described in Section 3.3.1 for each variable within the tropical region (4°S-4°N, 150°W-90°W). Upward pointing triangles mark the warm ENSO years, the downward pointing triangle marks the cold phase, and black stars are neutral ENSO years. Units are °C for T, none for S, ms^{-1} for U and V, cm for ssh.

Chapter 7

Dominant error subspace

7.1 MvOI experiments with a reduced number of EOFs

It is often suggested that the number of EOFs used to describe an error covariance structure be reduced and various criteria established to justify how many leading EOFs to retain, the rest - trailing EOFs - are discarded. Sometimes the eigencurve itself provides a clue where there is a clear separation between the leading and the trailing modes. Preisendorfer (1988, Chapter 5) suggests that if, for example, the eigenvalues drop abruptly after a certain index and remain relatively small, then the EOFs corresponding to trailing eigenvalues contain the correlation structures that not significant, i.e. not significantly different from white noise, and the leading EOFs describe the "signal" of interest.

However this is not the case in the figure 4.2: there is no obvious separation between "signal" and "noise" and even the largest eigenvalues are close together. Yet the contribution to the total variance of the individual eigenvalues beyond index 30 or so is quite small, less than 1% each, so it may be possible to truncate some EOFs, if only for reasons of computational efficiency. To investigate how truncating the number of EOFs will affect the performance of the assimilation, a series of MvOI experiments was done with decreasing numbers of retained EOFs. The rms difference with CTD/ADCP data was calculated for each experiment as the evaluation metric.

Blunt truncation of the number of EOFs worsens the performance of the multivariate assimilation since effectively more relative weight is given to the model than previously. The deterioration of the results, however, is not uniform for all variables (see Figures 8.5 and 8.6). In temperature the reduction in the number of EOFs leads to larger rmsd, especially in the Niño 3 region and in the Niño 4 region north of the equator within and below the thermocline. The effect of truncating the EOFs is not so uniform in salinity. Near the surface fewer EOFs result in larger rmsd in all re-

gions, however within the halocline the MvOI performance is as good or better with fewer retained EOFs. Below 300 m the reduction of the number of EOFs down to 30 has a detrimental effect, but an experiment with 60 retained EOFs does not significantly differ from the full MvOI. The picture in zonal velocity is also mixed. North of the equator the experiment with 30 retained EOFs performs the worst near the surface in both Niño 4 and Niño 3 regions, while south of the equator it is as good as the full MvOI. Thus it is important to understand how the error covariance matrix is affected when only a certain number of EOFs is retained. Since the nature of the variability and co-variability of various quantities is complex (as illustrated by the figures in Section 3.3.3), it can be anticipated that the effects of EOF truncation would differ for different variables and their cross-relationships.

7.2 Effects of truncating EOF set on forecast error variance and covariance

The analysis of the eigencurves in Section 4.2 indicates that the level of variance explained by a single EOF drops below the level of noise (variance of the residuals) at about 60th EOF. This may be an indication that the information about variability described by the low order EOFs is rather uncertain.

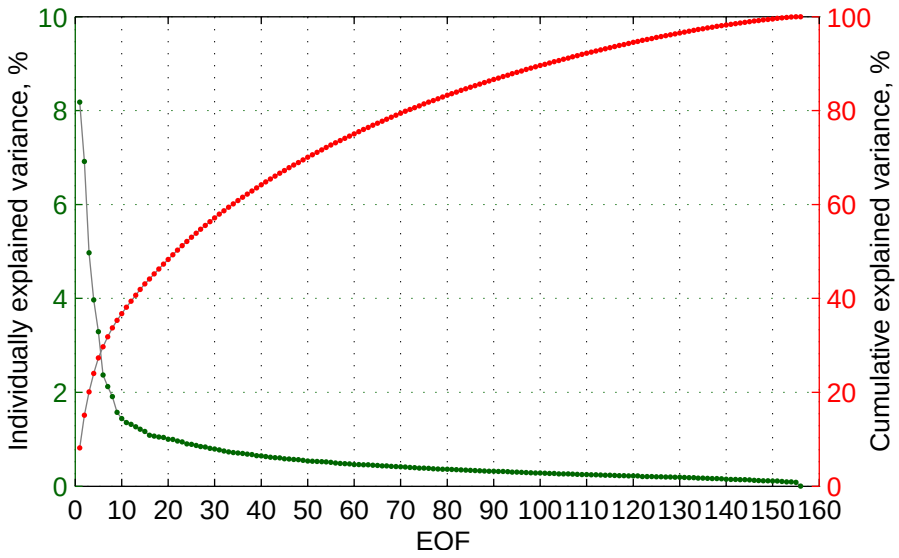

Figure 7.1: Variance explained by each individual EOF (green, scale on the left) and cumulative explained variance (red, scale on the right).

Thus the investigation in this chapter is focused on the case of 60 retained EOFs: this number is about two-fifth of the total number (156) of EOFs and using it leads to significant savings in computational resources.

Truncating the EOF set affects the ratio between the forecast and the observational error variance, thereby altering the relative confidence the assimilation has in model and data. By reducing the forecast error variance more weight is given to the model. The amount of total variance explained by each EOF is shown in Figure 7.1 along with the cumulative explained variance. Sixty EOFs explain about 75% of the total variance. The reduction of variance due to the truncation of EOFs is tabulated for every component of the state vector for every depth level (table 7.1). As can be seen, the variance levels are reduced by about 30-35% in temperature, 35-40% in salinity (with the exception of 25 m level) and by 20-25% in currents.

The reduction of forecast error variance in the observed variable leads to a smaller correction towards data. It is not only the amplitude of the correction is affected when the EOF set is truncated. The correlation scales are also altered, in general becoming broader. This may have a beneficial effect on the assimilation increments by making them smoother, but it also creates artificially high correlations at large spatial lags. It also makes the matrix inversion less well

Table 7.1: Variance retained by the 60 leading EOFs (%), broken down by variable type and depth level. The corresponding value for the sea surface height is 74%. These values are averaged over 10 realizations of the ensemble, as described in Section 4.1.

depth (m) / variable	1	25	50	75	100	125	150	200	250	300	500
T	66	70	66	66	66	68	70	70	66	63	60
S	65	84	63	61	64	60	59	60	61	60	57
U	75	75	75	75	74	74	73	70	67	66	64
V	74	76	77	77	78	78	77	76	74	73	72

conditioned. An example of the progressively changing shape of the zonal relative covariance curve with the reduction in the number of retained EOFs is shown in Figure 7.2. The covariances accumulated for all, 60 or 30 leading EOFs are normalized with the same factor to reflect the relative loss of variance, as given by

$$c_{i,j} = \frac{\sum_{m=1}^{M} l_{i,m} l_{j,m}}{\left(\sum_{n=1}^{N_{total}} l_{i,n} \right)^{1/2} \left(\sum_{n=1}^{N_{total}} l_{j,n} \right)^{1/2}}, \tag{7.1}$$

where $c_{i,j}$ is the normalized covariance value for the state vector elements i and j, $l_{i,m}$ is the i'th element of the m'th EOF, M is the number of leading EOFs, N_{total} is the total number of available EOFs. Compact support controls the very long correlation scales, but the local scales also increase. For example, with all EOFs the correlation between the observation at 155 °W (marked A) and a point B at 165°W is about 0.5, while for 30 retained EOFs, taking into account the loss of variance at the observation location, this value would be about 0.75 and the correlation would drop to 0.5 only if one moves away to 175°W (point C), i.e. 10 more degrees in the zonal direction.

The portion $\mathbf{P}^{T,T}$ of the multivariate error covariance matrix $\mathbf{P}$ (Equation 3.3) can be re-written as

$$\mathbf{P}^{T,T} = \mathbf{P}^{T,T}_{lead} + \mathbf{P}^{T,T}_{trail}, \tag{7.2}$$

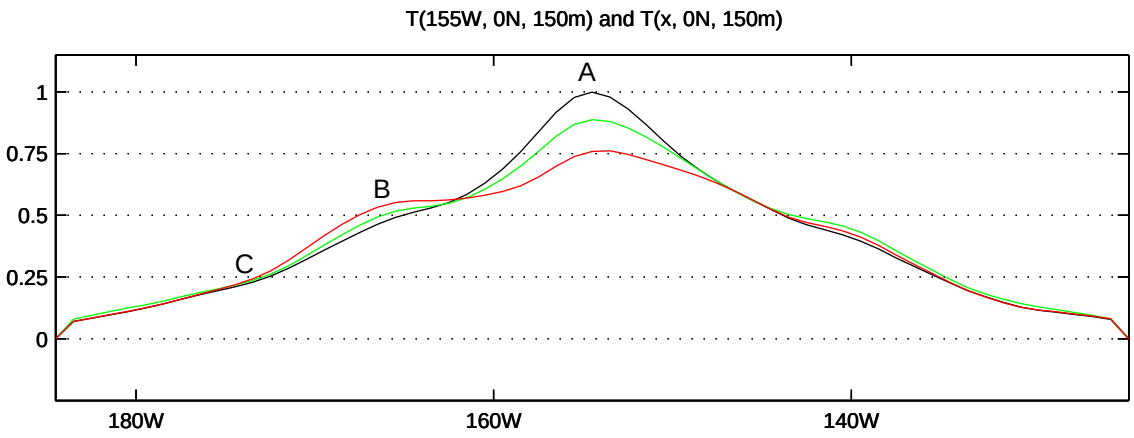

Figure 7.2: Examples of zonal normalized covariance accumulated from all (black), 60 (green) and 30 (red) leading EOFs. The compact support is applied as described in the text.

where $\mathbf{P}^{T,T}_{lead}$ is the part corresponding to the leading EOFs and $\mathbf{P}^{T,T}_{trail}$ is the part corresponding to the trailing EOFs. Such partitioning is possible because of orthogonality of EOFs (Equation 3.6). When only the temperature observations are assimilated, the components of the forecast error covariance matrix $\mathbf{P}$ that enter into the increment calculation are $\mathbf{P}^{T,T}$, $\mathbf{P}^{T,S}$, $\mathbf{P}^{T,U}$ and $\mathbf{P}^{T,V}$.

To see how the shape of the covariance changes as the number of EOFs is reduced, the case presented in Figure 3.5 is revisited. Now the covariance structure between temperature and other variables is calculated based on $\mathbf{P}^{T,T}_{lead}$ and $\mathbf{P}^{T,T}_{trail}$, and similarly partitioned $\mathbf{P}^{T,S}_{lead}$ and $\mathbf{P}^{T,S}_{trail}$, $\mathbf{P}^{T,U}_{lead}$ and $\mathbf{P}^{T,U}_{trail}$, $\mathbf{P}^{T,V}_{lead}$ and $\mathbf{P}^{T,V}_{trail}$ are shown in Figures 7.3 and 7.4. Other locations exhibit similar behavior. The normalized covariance structure $\mathbf{P}^{T,T}_{lead}$ is re-calculated using 60 leading EOFs (Figure 7.3). The remaining trailing EOFs, 61 through 156, are used for $\mathbf{P}^{T,T}_{trail}$ (Figure 7.4). The greatest effect of reducing the number of the EOFs is in $\mathbf{P}^{T,T}$, where the maximum of the remaining covariance exceeds 0.2. The cross-covariance between temperature and currents (zonal and meridional velocities) is the least affected by the EOFs truncation - the covariance structures are very similar in the case of the full EOF set (Figure 3.5) and the 60 leading EOFs. The temperature-zonal velocity covariance remaining in the trailing EOFs (Figure 7.4) is less than 0.1 compared to the maximum amplitude of about 0.4 in the case of a full EOF set. The temperature-meridional velocity covariance is small (just over 0.2) in the case of full EOF set and is less than

0.1 in the trailing EOFs. The temperature-salinity covariance amplitude reaches 0.5 in the case of the full EOF set and about 0.1 is retained in the trailing EOFs.

This example illustrates the fact that truncating EOFs has the most detrimental effect on the temperature covariance structure, while most of the multivariate covariance is still captured by the leading 60 EOFs.

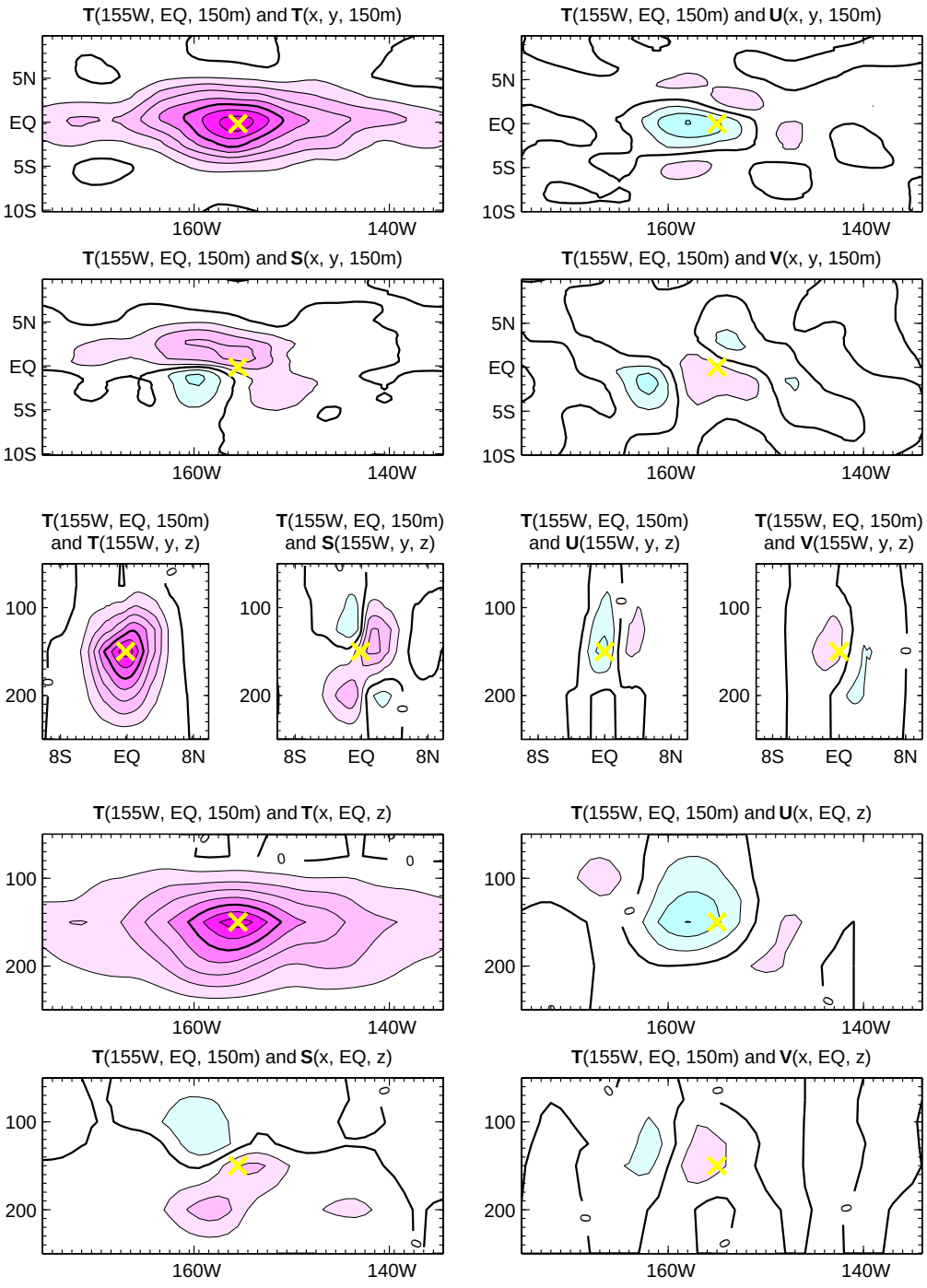

Figure 7.3: Examples of normalized covariance structure accumulated from 60 leading EOFs. The compact support is applied as described in the text. Contour interval is 0.1. Crosses mark the position of the simulated observation.

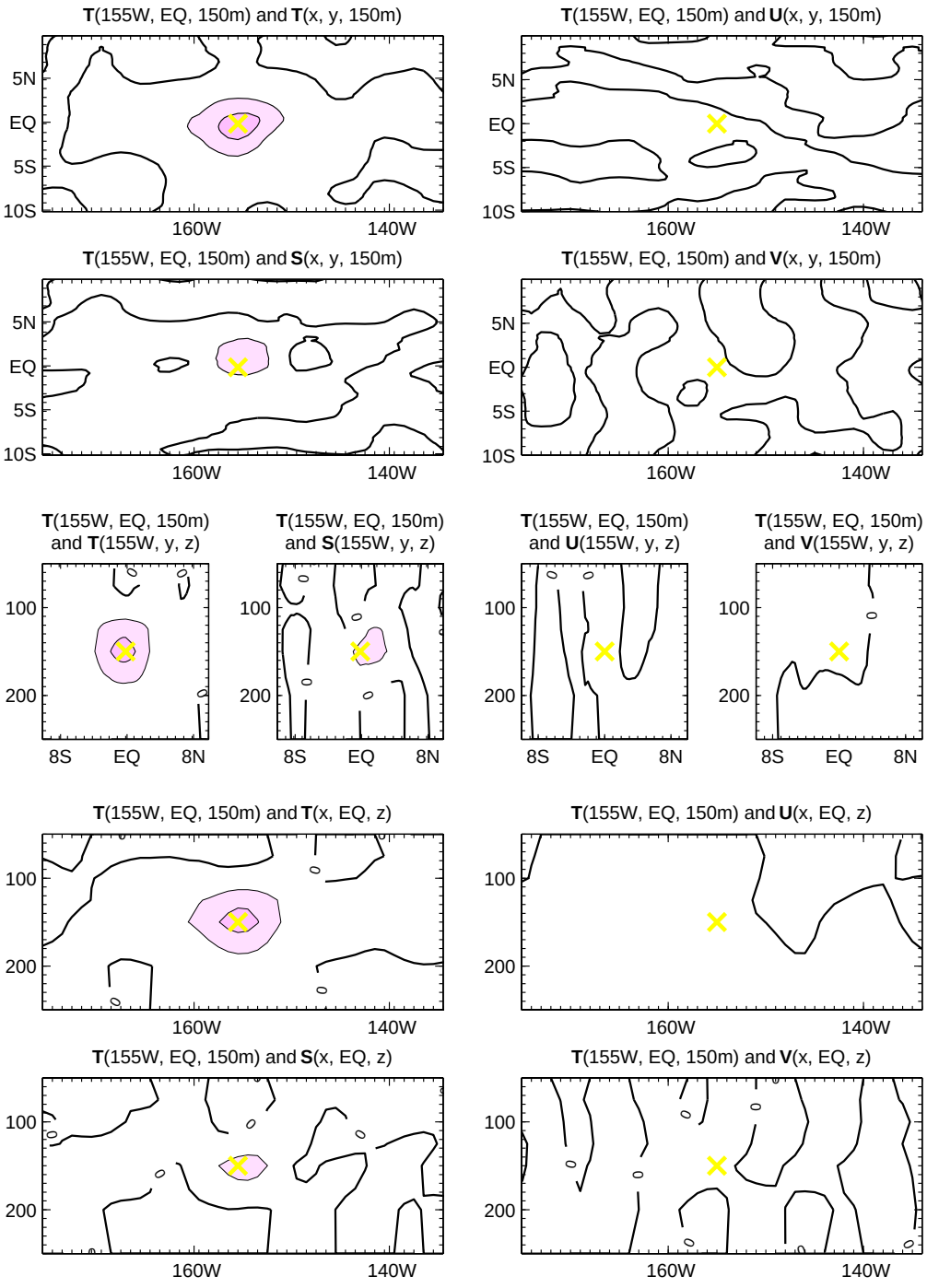

Figure 7.4: Examples of normalized covariance structure derived from trailing (61-156) EOFs. The compact support is applied as described in the text. Contour interval is 0.1. Crosses mark the position of the simulated observation.

Chapter 8

Augmenting a truncated set of EOFs with a Gaussian model

8.1 A simple model of local variability

Since the error cross-covariances between the observed temperature and other components of the state vector (salinity and currents) is relatively well described by the leading 60 EOFs, and only the temperature-temperature covariance structure and error variance amplitude is significantly affected by the EOFs truncation, it may be possible to approximate the local, small-scale and relatively regular (T,T) covariance structure with an efficient functional form, for example, a simple Gaussian model. Thus the Equation 7.2 can be re-written as

$$\mathbf{P}^{T,T} = \mathbf{P}^{T,T}_{lead} + \hat{\mathbf{P}}^{T,T}, \tag{8.1}$$

where $\hat{\mathbf{P}}^{T,T}$ is an approximation to $\mathbf{P}^{T,T}_{trail}$. The approximation of the full matrix $\mathbf{P}$ is then

$$\mathbf{P} \approx \mathbf{P}^* =$$

$$\begin{bmatrix} \mathbf{P}^{T,T} & \mathbf{P}^{T,S} & \mathbf{P}^{T,U} & \mathbf{P}^{T,V} & \mathbf{P}^{T,ssh} \\ \mathbf{P}^{T,S} & \mathbf{P}^{S,S} & \mathbf{P}^{S,U} & \mathbf{P}^{S,V} & \mathbf{P}^{S,ssh} \\ \mathbf{P}^{U,T} & \mathbf{P}^{U,S} & \mathbf{P}^{U,U} & \mathbf{P}^{U,V} & \mathbf{P}^{U,ssh} \\ \mathbf{P}^{V,T} & \mathbf{P}^{V,S} & \mathbf{P}^{V,U} & \mathbf{P}^{V,V} & \mathbf{P}^{V,ssh} \\ \mathbf{P}^{ssh,T} & \mathbf{P}^{ssh,S} & \mathbf{P}^{ssh,U} & \mathbf{P}^{ssh,V} & \mathbf{P}^{ssh,ssh} \end{bmatrix}_{lead} + \begin{bmatrix} \hat{\mathbf{P}}^{T,T} & 0 & 0 & 0 & 0 \\ 0 & 0 & 0 & 0 & 0 \\ 0 & 0 & 0 & 0 & 0 \\ 0 & 0 & 0 & 0 & 0 \\ 0 & 0 & 0 & 0 & 0 \end{bmatrix} = \tag{8.2}$$

$$\mathbf{P}_{lead} + \hat{\mathbf{P}}.$$

Then the gain matrix $\mathbf{K}$ (Equations 2.6 and 3.7) may be approximated as

$$\begin{aligned} \mathbf{K}^* &= \mathbf{P}^*\mathbf{H}^T(\mathbf{H}\mathbf{P}^*\mathbf{H}^T + \mathbf{R})^{-1} \\ &= (\mathbf{P}_{lead} + \hat{\mathbf{P}})\mathbf{H}^T(\mathbf{H}(\mathbf{P}_{lead} + \hat{\mathbf{P}})\mathbf{H}^T + \mathbf{R})^{-1} \\ &= (\mathbf{L}_{lead}\mathbf{L}^T_{lead} + \hat{\mathbf{P}})\mathbf{H}^T(\mathbf{H}(\mathbf{L}_{lead}\mathbf{L}_{lead} + \hat{\mathbf{P}})\mathbf{H}^T + \mathbf{R})^{-1}. \end{aligned} \tag{8.3}$$

Here $\mathbf{L}_{lead}$ corresponds to $\mathbf{P}_{lead}$ as described in Equation 3.6, but with the matrix $\mathbf{A}$ constructed

only from the leading EOFs.

To model $\hat{\mathbf{P}}$ as a Gaussian function, its amplitude and spatial scales need to be specified. The loss of variance documented in table 7.1 does not occur uniformly for all locations and depth levels. This is illustrated in Figure 8.1. It shows a section of the diagonal of $\mathbf{P}^{T,T}$, corresponding to temperature at 150 meters. Here all the grid points are ordered from south to north and from west to east. To show their relative amplitude the total variance, the variance explained by the 60 leading EOFs, and the variance explained by the remaining EOFs are plotted against each other. Looking at the entire basin (top panel) one can see that the levels of greatest variability are observed in the tropical region and in the northern midlatitudes. The largest relative loss of variance as a result of EOF truncation occurs in southern midlatitudes (the area shaded green nearly overlaps with blue). However it is difficult to analyze individual grid points on this plot (there are almost 3×10^5 of them). Thus the second panel shows a zoom onto the tropical region. Here each longitudinal row appears as a "tooth" on a saw-like curve, they have similar patterns of variance distribution, but of varying amplitude. Finally the bottom panel shows in detail one such "tooth" - the equatorial longitudinal row. The highest total variance is observed between 160°W and 140°W, and here the relative loss of variance is the smallest, i.e. the are under the green curve is small compared to either blue or red. Between 140°E and the dateline the total variance is low and the amount of variance accounted for by the leading and trailing EOFs is nearly equal.

Since the loss of variance due to EOFs truncation is not uniform, instead of attempting to approximate it with a single value, the variance explained by the trailing EOFs was calculated at every grid point and at every depth level. These variances were used as the amplitude of the Gaussian function, thus restoring the observed temperature variance to the full value it would have if all EOFs were used.

The spatial scales of the Gaussian function were chosen to be 4° in the zonal, 1° in the meridional and 10 m in the vertical directions. These scales are based on the analysis of the shapes of the correlation structure, an example of which is shown in Figure 7.4. They later were fine-tuned by a series of experiments sweeping the possible values of these parameters. An example

of a Gaussian model of the small scale variability described by the trailing EOFs is shown in Figure 8.2 in the same case of equatorial temperature at 155°W. For easy reference the top panel panel repeats the top right panel from Figure 3.3 with the covariance structure derived from the complete set of EOFs, the second panel shows the covariance structure based on the first 60 EOFs (also top left in Figure 7.3), the third panel shows the covariance structure retained by the trailing EOFs (also top left in Figure 7.4). The fourth panel shows the Gaussian model of the local small scale covariance with the amplitude and scales as described above, and the last panel shows the covariance structure "reconstructed" by adding the second and the fourth panels as described in the Equation 8.2 - it closely resembles the top panel.

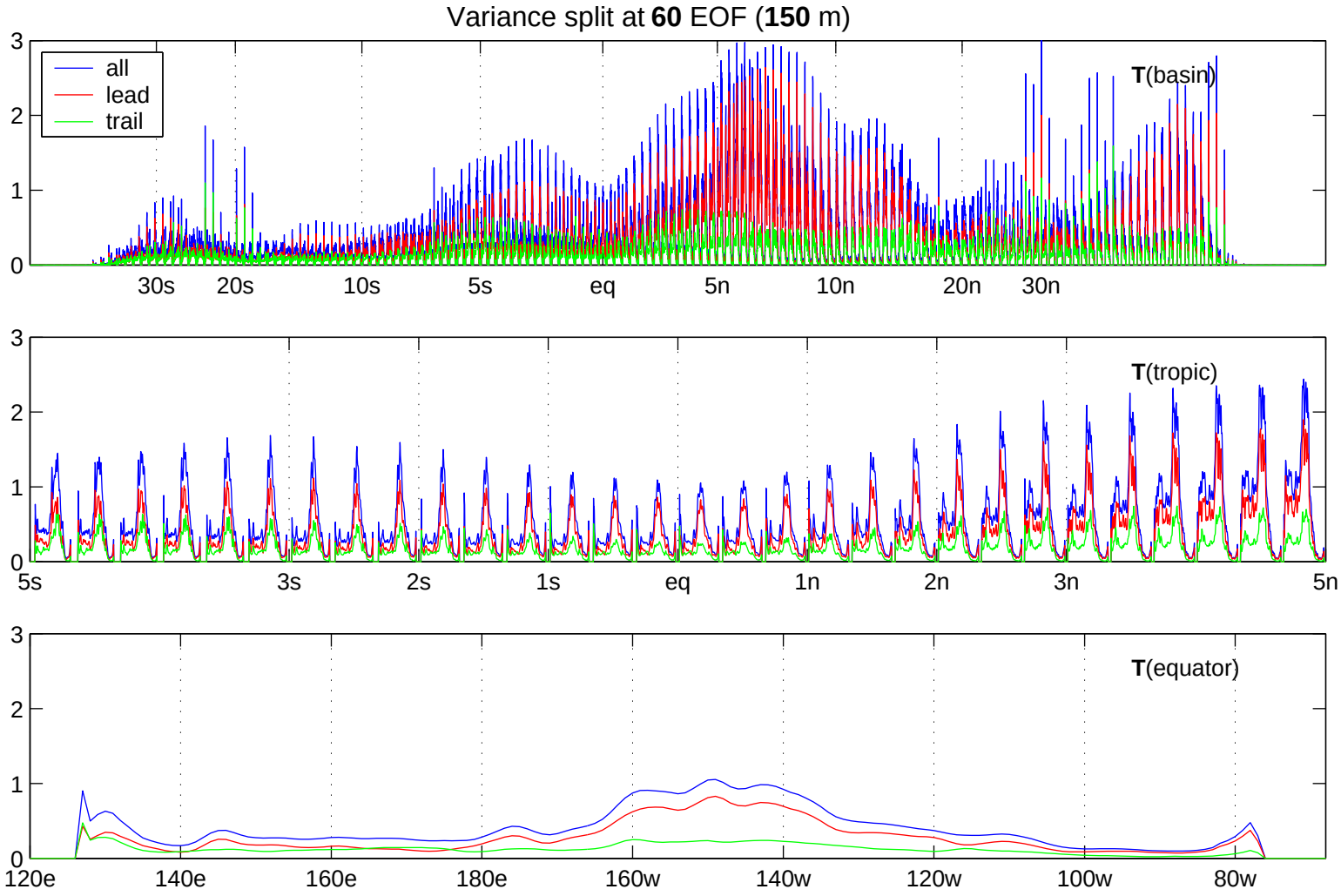

Figure 8.1: A section of the diagonal of $P^{T,T}$, the ordering is west to east, south to north. The top panel shows the entire Pacific basin, the middle panel zooms onto the tropical band ($5°S$-5°N), the bottom panel shows the equator. The blue, red and green curves show the levels of variance for the full set of EOFs, the truncated set and the variance explained by the trailing EOFs respectively.

A one-dimensional plot allows for comparison of all 10 available EOF realizations (Figure 8.3). Here zonal correlation curves at (155°W, EQ) are plotted in a manner similar to Figure 4.1 (top right panel), but with the compact support as described in Section 3.3.2. The order of panels is the same as in Figure 8.2. Here one can clearly see the different drop in variance for different EOF sets. This figure and the previous one show a single point on the diagonal of the error covariance matrix and the immediately adjacent off-diagonal elements. For a more general look at the matrix structure a small section is plotted that includes the same temperature diagonal elements shown in Figure 8.1 (bottom panel) along the equator at 150 meters and the off-diagonal elements in the same longitudinal row. The top left panel shows the section of the error covariance matrix $\mathbf{P}$ as computed from a complete set of EOFs, the middle left panel is the same $\mathbf{P}$ with compact support applied as described in section 3.3.2: the long-range correlations are set exactly to zero. The bottom left and the top right panel show the separation of the error covariance structure associated with the separation of the EOFs into leading (first 60) and trailing (61 through 156). The middle right panel shows the Gaussian model of the local variability designed to replace the lost structure in the panel above. The bottom right panel shows the approximated error covariance structure: leading EOFs plus Gaussian model of local variability.

8.2 Comparison with independent data and full MvOI

The results of the assimilation experiment with the approximated forecast error covariance matrix $\hat{\mathbf{P}}$ are presented next. The rmsd of the model fields and the CTD/ADCP data is shown in Figures 8.5 and 8.6, the MvOI with the full EOF set and MvOI with with only 60 EOFs are shown as well for reference. The shading shows the spread of the ensemble of 10 MvOI experiments, i.e. the green curves in Figures 6.1 and 6.2. It provides a metric for how well the approximate methods perform in the context of forecast error variability due to variations in $\mathbf{P}$.

North of the equator the performance of the MvOI with approximate $\hat{\mathbf{P}}$ (labeled MvOI_{60aug}) is as good as the full MvOI. The exception is for temperature in the Niño 3 region between 50 and 100 m where the MvOI_{60aug} curve is closer to the full MvOI, which is slightly worse than

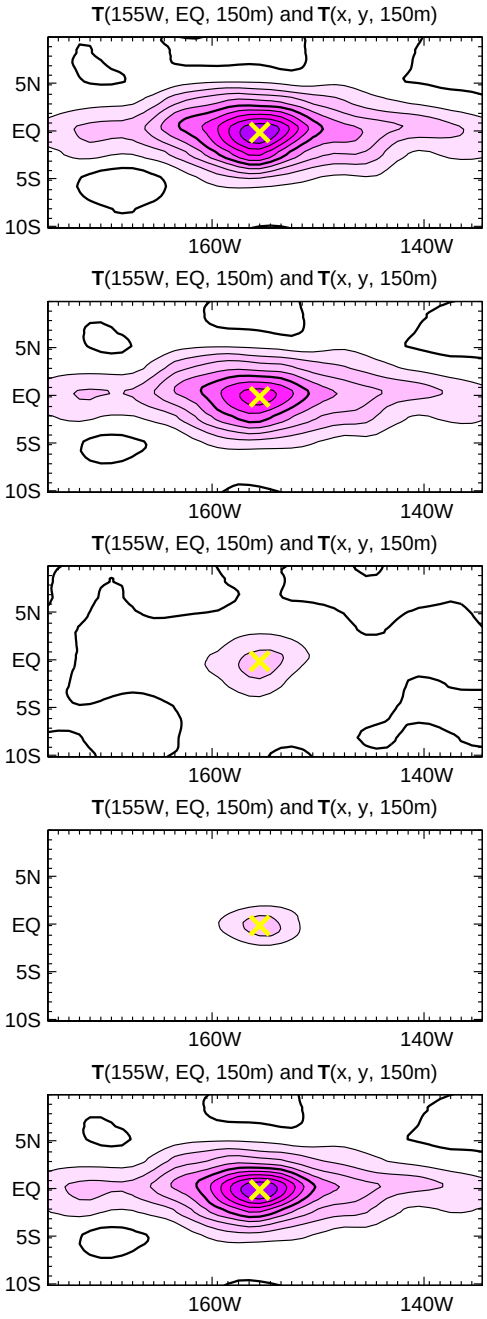

Figure 8.2: Top panel: Covariance structure calculated using a complete set of EOFs. Second panel: covariance structure as a result of retaining 60 leading EOFs. Third panel: covariance structure contained in the trailing EOFs. Fourth panel: a Gaussian model of the covariance structure explained by the trailing EOFs. Fifth panel: covariance structure of 60 EOFs augmented with the Gaussian covariance model.

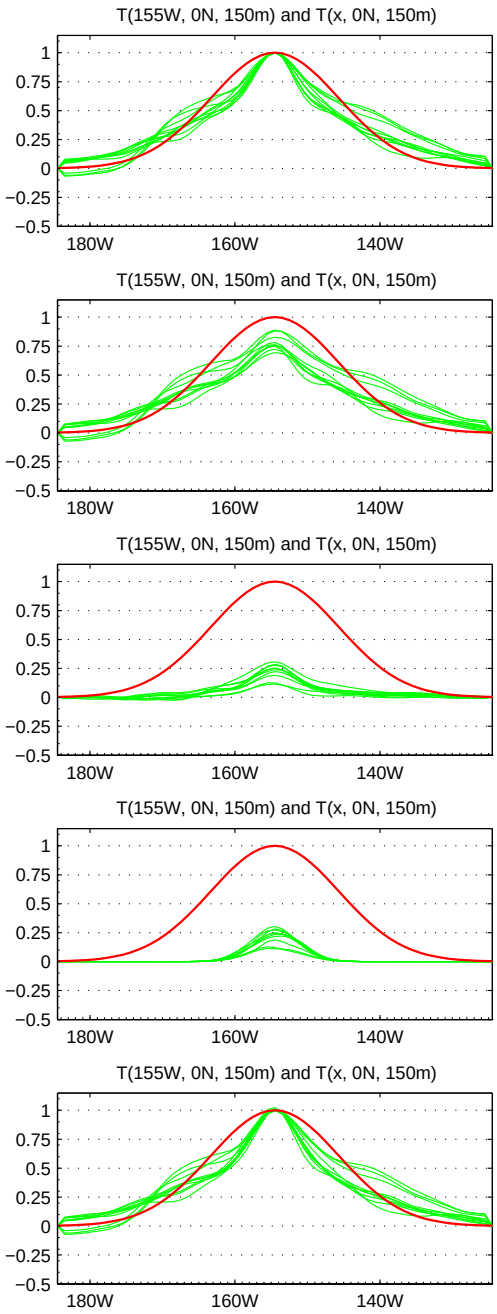

Figure 8.3: The number of EOFs is each panel is the same as in Figure 8.2. Here only one - zonal - dimension of the covariance structure is shown. Each of the thin green curves corresponds to a different set of EOFs, 10 in all. The red curve shows the functional form used in UOI for reference.

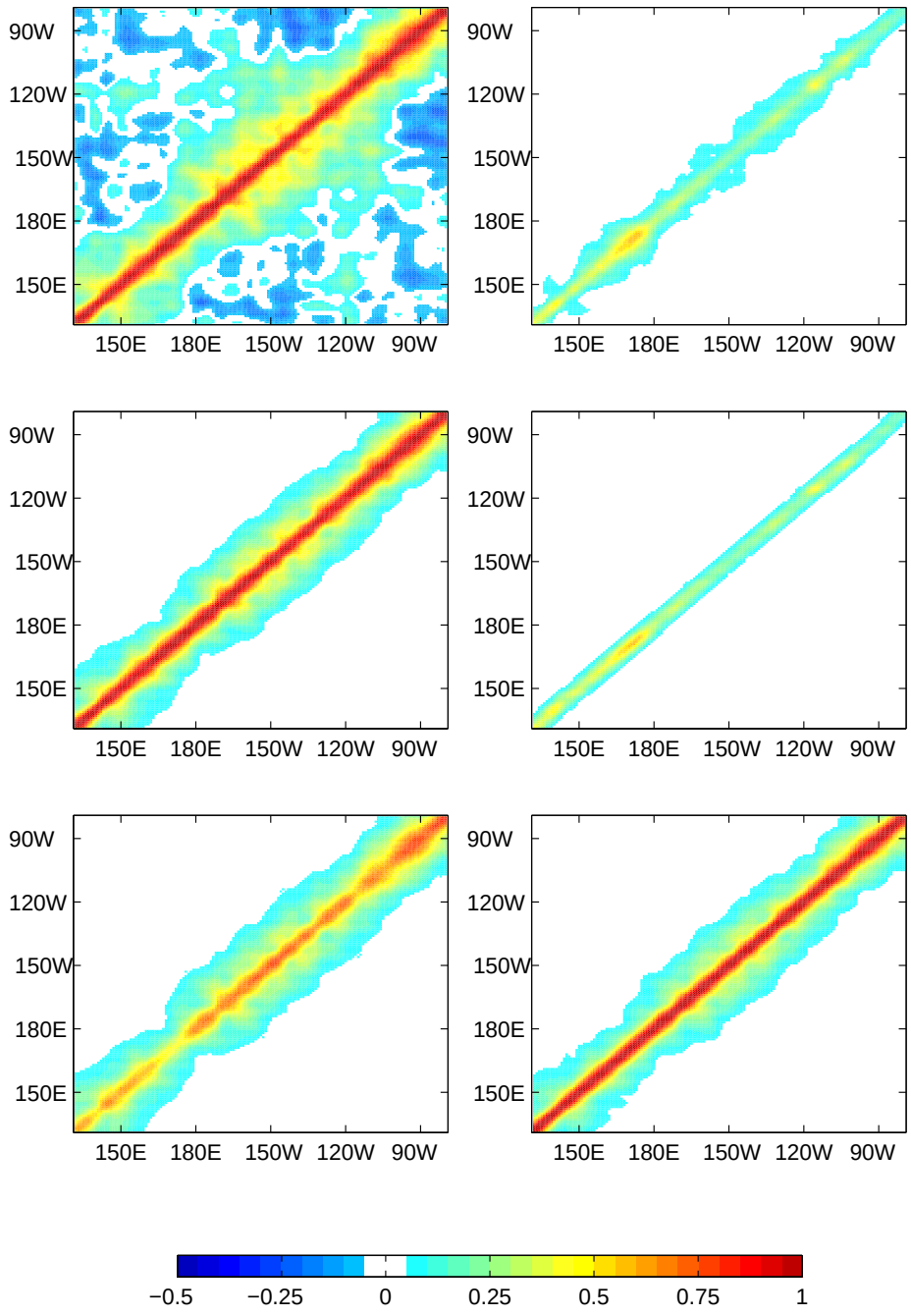

Figure 8.4: A section of matrix P, corresponding to temperature along the equator at 150 meters. Top left panel shows the covariance matrix structure derived from a complete set of EOFs, the middle left panel shows the effect of applying the compact support, the bottom left panel shows the structure based on the truncated set of 60 EOFs, the top right panel shows the structure explained by the trailing EOFs, the middle right panel shows the Gaussian model designed to replace the trailing EOFs, and the bottom right panel is the truncated set augmented with the Gaussian model.

the MvOI with truncated EOFs (labeled MvOI_{60}). In the Niño 4 region the MvOI_{60} curves falls outside the span of the MvOI ensemble between 100 and 500 meters - an indication that the truncated EOF set cannot properly account for the temperature forecast error. Since in salinity and velocity the MvOI_{60} curve is almost everywhere as good as the full MvOI, the goal of the experiment MvOI_{60aug} with the approximated forecast error covariance is to do no worse than the MvOI_{60}. This is in fact the result except in salinity very near the surface in the Niño 3 region, but the curves are within the shaded region. Zonal velocity appears to benefit at depth from the addition of the Gaussian model of local error.

South of the equator the advantage of using $\hat{\mathbf{P}}$ is not as obvious. The salinity rmsd of the MvOI_{60aug} in Niño 4 region is markedly different and worse than either full MvOI or MvOI_{60} which are very close, and is outside the MvOI ensemble span almost everywhere. The ensemble spread is very tight there. Zonal velocity again appears to be the best in the MvOI_{60aug} case, even slightly better than all members of the MvOI ensemble near the surface in the Niño 4 region. Temperature rmsd is worth in the MvOI_{60aug} case in the Niño 4 region just above 200 m, otherwise it is as good or better than the MvOI_{60}. Salinity rmsd of the MvOI_{60aug} in the Niño 3 region is good above 400 m and slightly worse below.

We now to take a closer look at the assimilation increments in the Niño 4 region south of the equator. Figure 8.7 shows the increment during the first cycle of assimilation for full $\mathbf{P}$, truncated $\mathbf{P}_{lead}$ and approximate $\hat{\mathbf{P}}$ for temperature (left), salinity (middle) and zonal velocity (right) and their respective differences. This is one of the worst cases where the MvOI_{60aug} increment differs more from the full MvOI increment than the MvOI_{60} increment. South of the equator the temperature increments in the top two panels are very similar, the scales of the correction are broad and encompass the observations from the equator to 8°S (the TAO buoys are located at the equator, 2°S, 5°S, 8°S and at the same meridian north of the equator) - a sign that the underlying error structure is large scale and is well accounted for by the 60 leading EOFs. Here the Gaussian model with predefined small scales introduces artificial local temperature maxima at the observation locations, which in turn leads to undesirable features in the salinity increment: in

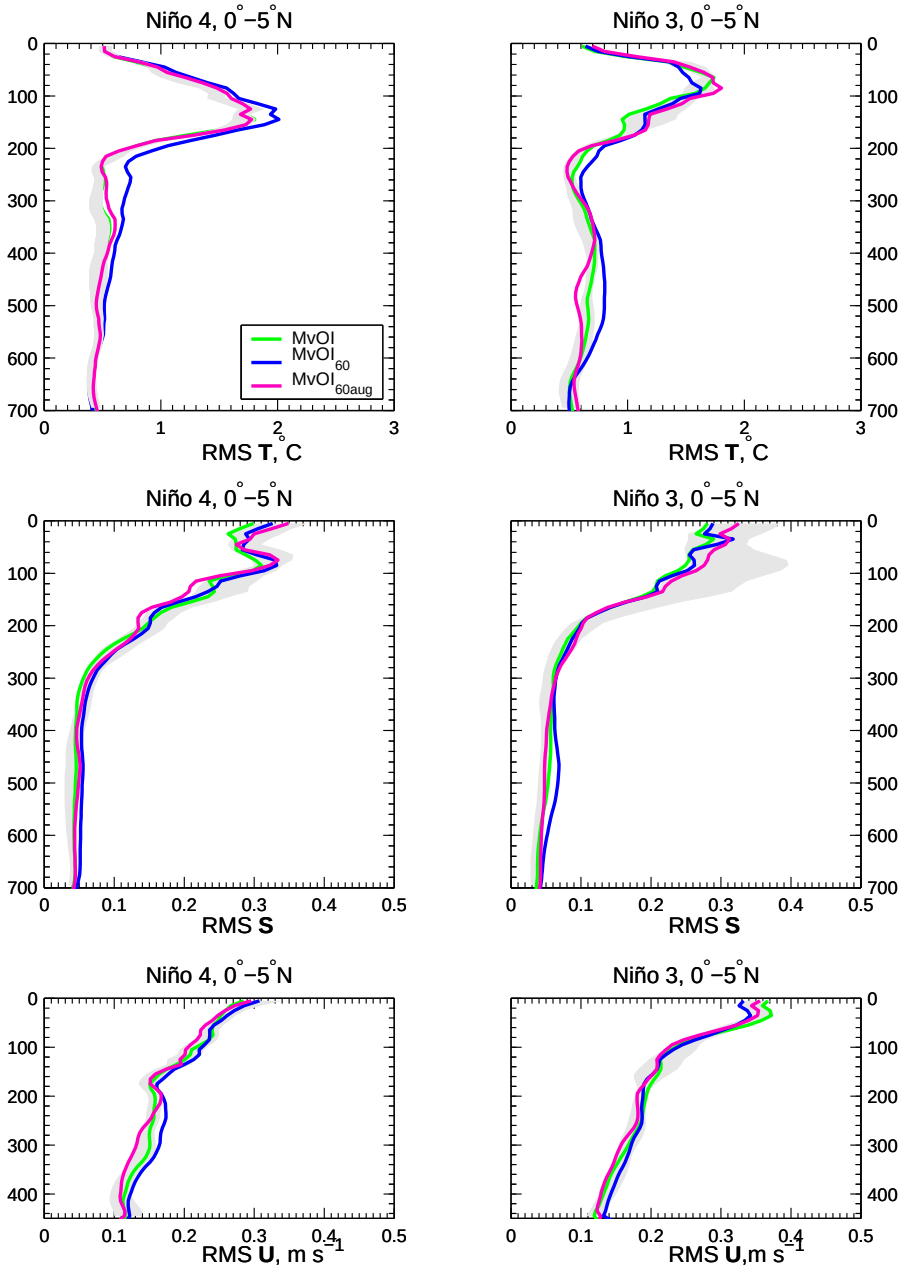

Figure 8.5: Rmsd between MvOI based on leading EOFs augmented with Gaussian local variability model and CTD/ADCP data as a function of depth (m) for the 35 transects. Full MvOI and MvOI based on truncated EOFs set are shown for comparison. The shading shows the spread of the 10 full MvOI experiments with different realizations of the **P** matrix. Statistics are grouped by Niño 4 (160°E-150°W) and Niño 3 (150°W-90°W) regions, and each area is further divided into two halves, south and north of the equator (0°-5°N shown here).

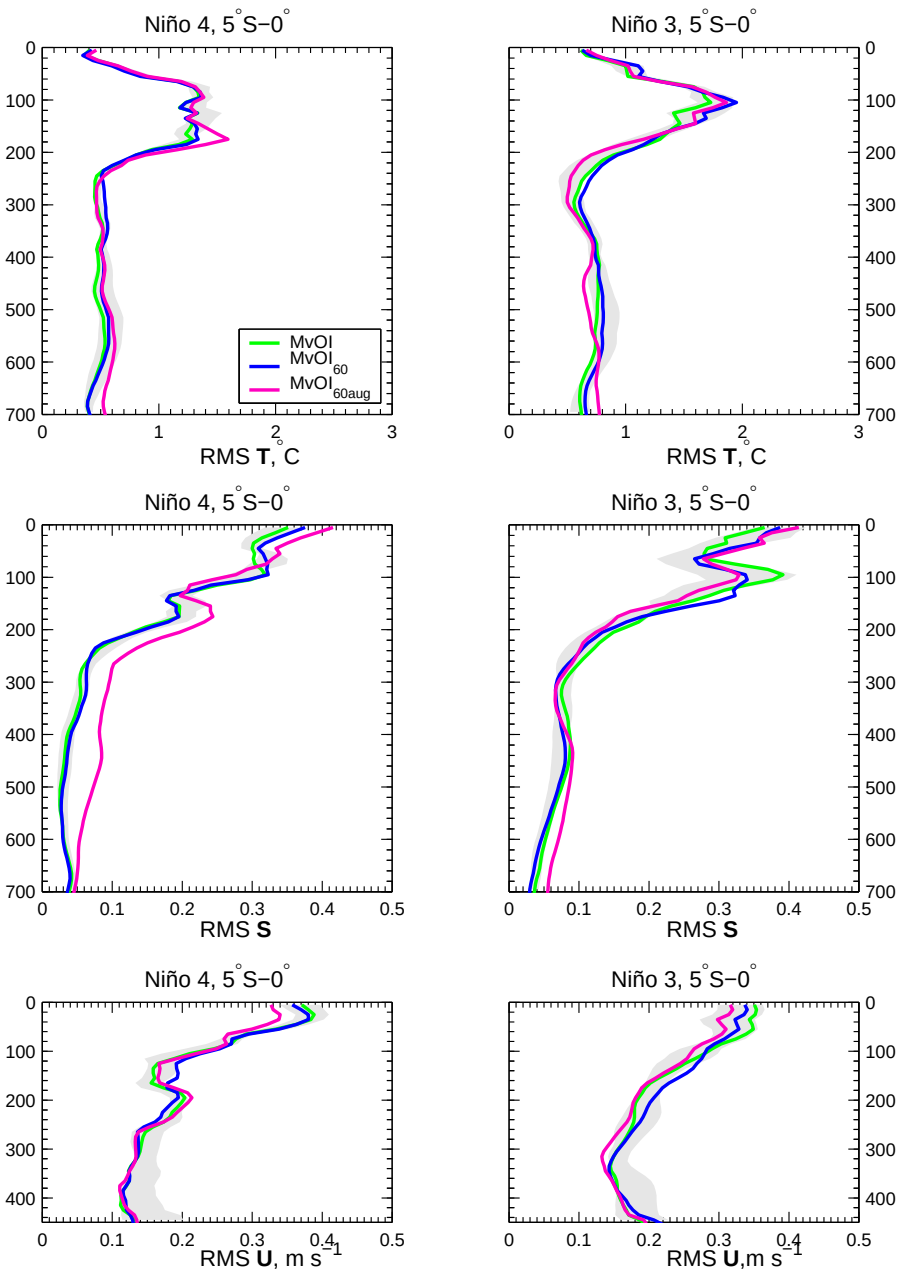

Figure 8.6: Rmsd between MvOI based on leading EOFs augmented with Gaussian local variability model and CTD/ADCP data as a function of depth (m) for the 35 transects. Full MvOI and MvOI based on truncated EOFs set are shown for comparison. The shading shows the spread of the 10 full MvOI experiments with different realizations of the **P** matrix. Statistics are grouped by Niño 4 (160°E-150°W) and Niño 3 (150°W-90°W) regions, and each area is further divided into two halves, south and north of the equator (5°S-0° shown here).

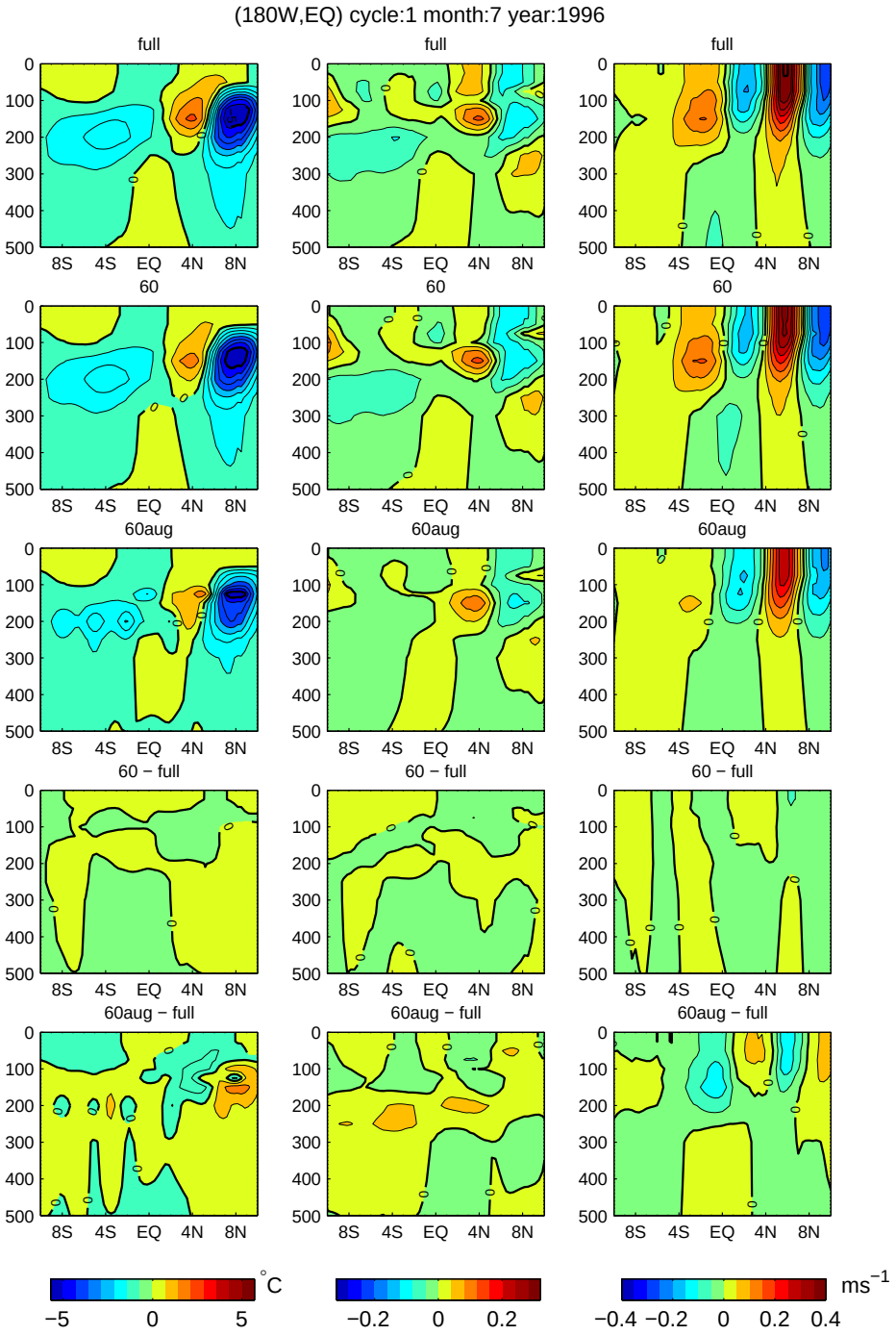

Figure 8.7: Assimilation increment during the first cycle of an experiment. Top row: temperature, salinity and zonal velocity increment for the full MvOI. Second row: same for the MvOI_{60}. Third row for MvOI_{60aug}. Fourth row is the difference between the full MvOI and MvOI_{60}. Fifth row is the difference between the full MvOI and MvOI_{60aug}. The contour interval for temperature is 0.8°C, for salinity is 0.04, for zonal velocity is 0.05 ms^{-1}.

this case the underestimation of negative and positive maxima south of the equator.

The discussion of an assimilation scheme wouldn't be complete without a look at the resulting ocean states. As in Section 5.5, several meridional cross-sections (Figures A.1-A.4, A.5-A.8 and A.9-A.12 in the appendix) are considered. The experiment with the truncated set of EOFs augmented by the Gaussian model of small-scale variability is labeled MvOI_{60aug}. Upon comparing it to the MvOI with the full EOF set (labeled MvOI_T) one can see that the temperature structure is quite similar. In salinity MvOI_{60aug} captures the extension of the saline water at the equator near the surface at 167°E and 180°W, but creates an artificial maximum at 5°S near 150 m. At 156°W MvOI_{60aug} gives a better estimate of the amplitude of the saline extension from south towards the equator (MvOI_T slightly overestimates it), but the salinity near the surface south of the equator is too high in MvOI_{60aug}. At 125°W the shape and amplitude of the salinity extension from MvOI_{60aug} is very good, but near the surface on the equator the field is too fresh. Zonal current structures in the two experiments are similar. At 125°W MvOI_{60aug} gives a better estimate of the location of the equatorial undercurrent.

In conclusion, the contribution of the trailing EOFs to the forecast error covariance, while small, is not trivial. Simply discarding a significant number of EOFs worsens the assimilation results, especially affecting the temperature profiles. The salinity and zonal velocity do not consistently degrade with fewer EOFs, occasionally even benefiting from the smoother smaller correction generated from leading EOFs. A use of a simple Gaussian model of local error variance designed to make up for the loss of variance and the small scales accounted for by the trailing EOFs produced mixed results: the temperature field in general was as good as the temperature field produced by the full MvOI, the zonal velocity improved upon the full MvOI, but the salinity field degraded in some regions while being as good as full MvOI in others.

Chapter 9

Simultaneous temperature and salinity assimilation

9.1 Synthetic salinity data

In addition to making corrections to unobserved parts of the state vector, a multivariate forecast error model allows simultaneously processing of observations of different types. During the period of interest, 1996-1998, there were virtually no salinity observations. Thus a set of synthetic salinity observations is used to test the impact of the MvOI scheme to analyze the two data types at the same time. A salinity profile was created for each temperature observation based on the T-S relationship in the Levitus climatology (Levitus and Boyle 1994). To get a sense of how these profiles relate to nature they are compared to the CTD data in the same fashion as the temperature profiles were analyzed in Section 5.2. There is an apparent non-zero mean difference between the two data sets in the upper 200 m, but the standard deviation amplitude is comparable to the rms difference between the control or any of the assimilation analyses and CTD data (see, for example, figure 5.2).

From such a synthesized data set one cannot expect a realistic reproduction of the synoptic variability. The interannual variability of the salinity field cannot be captured either. Yet it may help correct systematic errors that are present in the model. To allow for such correction, and at the same time to lessen the effect on the time-dependent variability, the observational error standard deviation for the synthetic salinity data is set to a high value of 0.1.

9.2 Assimilation experiments

Two experiments have been conducted: one with both TAO temperature and synthetic salinity at TAO locations being assimilated (labeled MvOI_{TS}) and one with just salinity data being included (MVOI_{S}). The second experiment cannot be expected to produce a very realistic

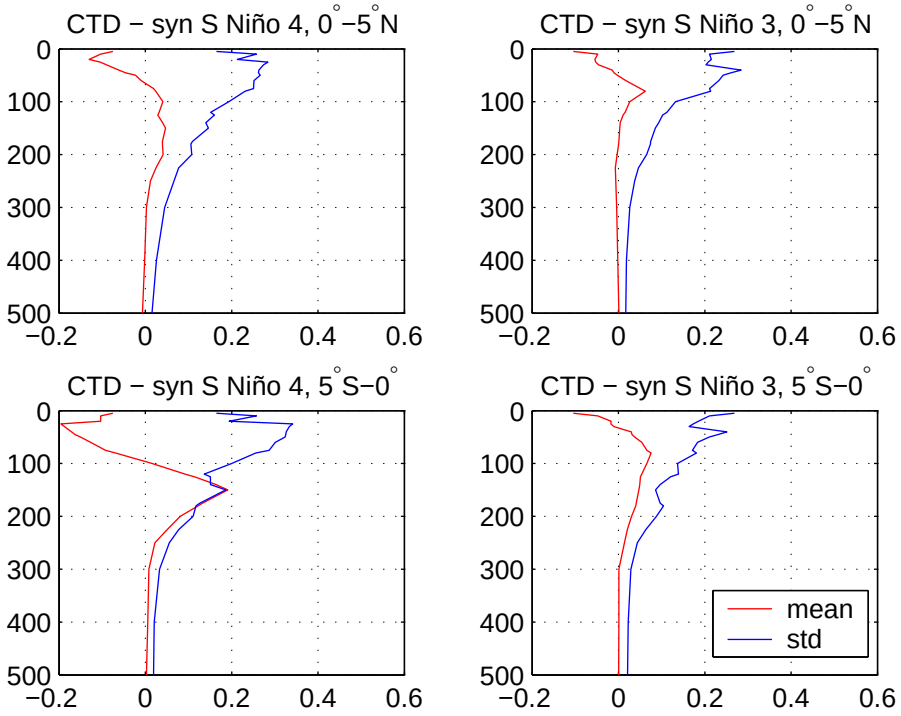

Figure 9.1: Mean difference and standard deviation of $S_{CTD} - S_{syn}$ grouped by Niño 4 (160°E-150°W) and Niño 3 (150°W-90°W) regions south and north of the equator.

ocean state, but it will serve as a "sanity" check for assimilation algorithm implementation. As in Chapters 5, 6 and 8, a rms difference from the independent CTD/ADCP data set is calculated (Figures 9.2 and 9.3) and the meridional sections are shown in the appendix. The MvOI$_S$ sections are not shown, since this study was not expected to produce an improved subsurface temperature structure. The MvOI with the full EOF set assimilating temperature is labeled MvOI$_T$ (repeated from Figures 5.1, 5.2, 8.5 and 8.6). The control statistics are also repeated for easy reference. As expected MvOI$_S$ overall performance is poor; however it is able to correct salinity bias near the surface in the Niño 4 regions north and south of the equator and south of the equator in the Niño 3 region. MvOI$_{TS}$ is able to combine the best features of MvOI$_S$ and MvOI$_T$: its rmsd with CTD is nearly identical to that of MvOI$_T$ in temperature and consistently smaller in salinity. The rmsd from ADCP in zonal currents from MvOI$_{TS}$ is also as good or better than that from MvOI$_T$.

Meridional temperature sections confirm that MvOI$_{TS}$ fields are very similar to MvOI$_T$. The salinity section at 167°E (Figure A.6) shows that MvOI$_{TS}$ estimates the amplitude of the

saline maxima at 150 m south of the equator and at approximately 4°N better than MvOI_T (or any other run). At 180°W the amplitude and equatorward extension of the saline maximum is better in MvOI_{TS}, but it is not deep enough at 8°S. Both MvOI_{TS} and MvOI_T underestimate salinity near the surface at the equator. In the east, the salinity structures are very similar in MvOI_{TS} and MvOI_T, but again MvOI_{TS} gives better amplitude of the salinity maxima, while MvOI_T tends to overestimate it. Zonal velocity structures are very similar in the two experiments.

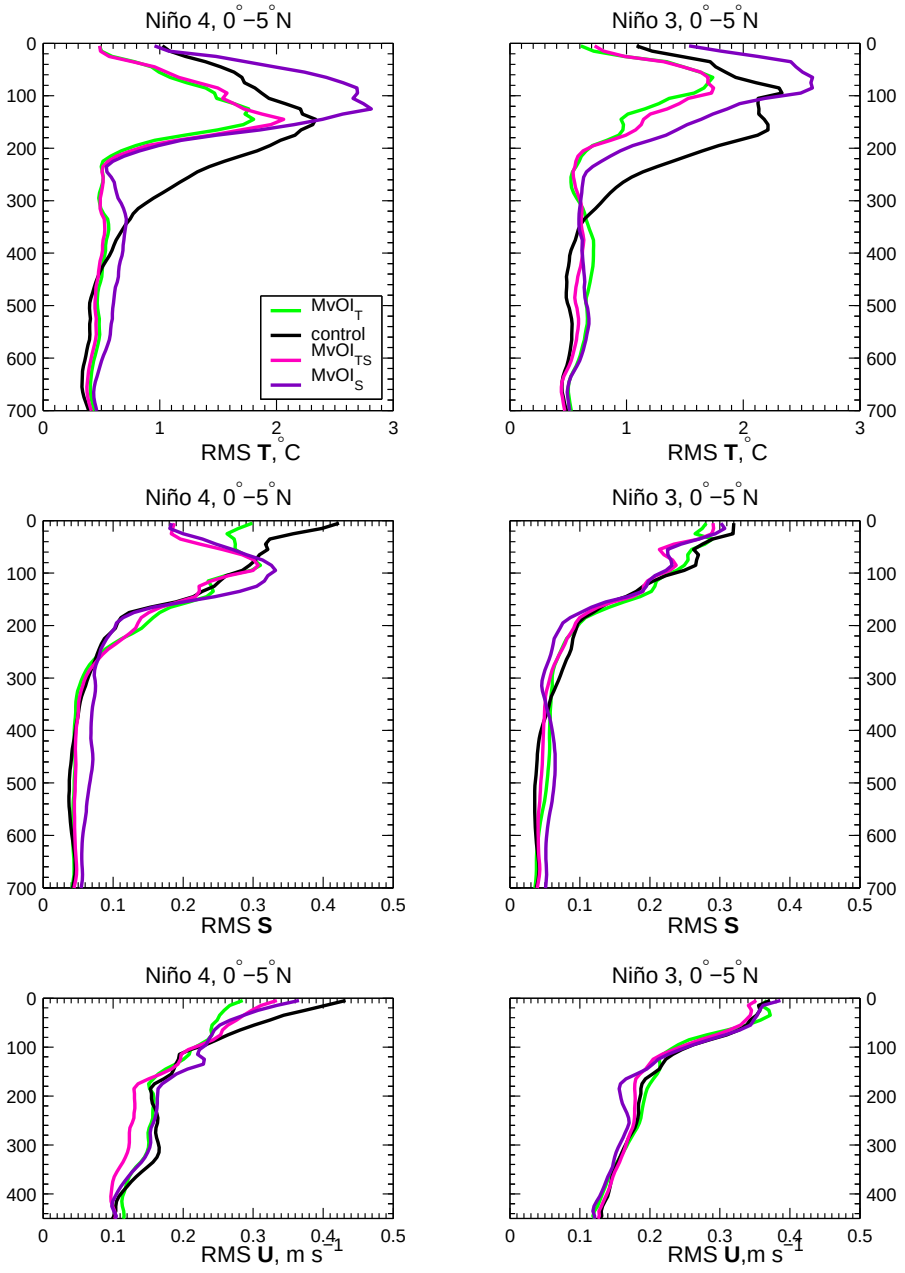

Figure 9.2: Rmsd between the four model runs (MvOI_T, MvOI_{TS}, MvOI_S and control) and the observations as a function of depth (m) for the 35 transects. Statistics are grouped by Niño 4 (160°E-150°W) and Niño 3 (150°W-90°W) regions, and each area is further divided into two halves, south and north of the equator (0°-5°N shown here).

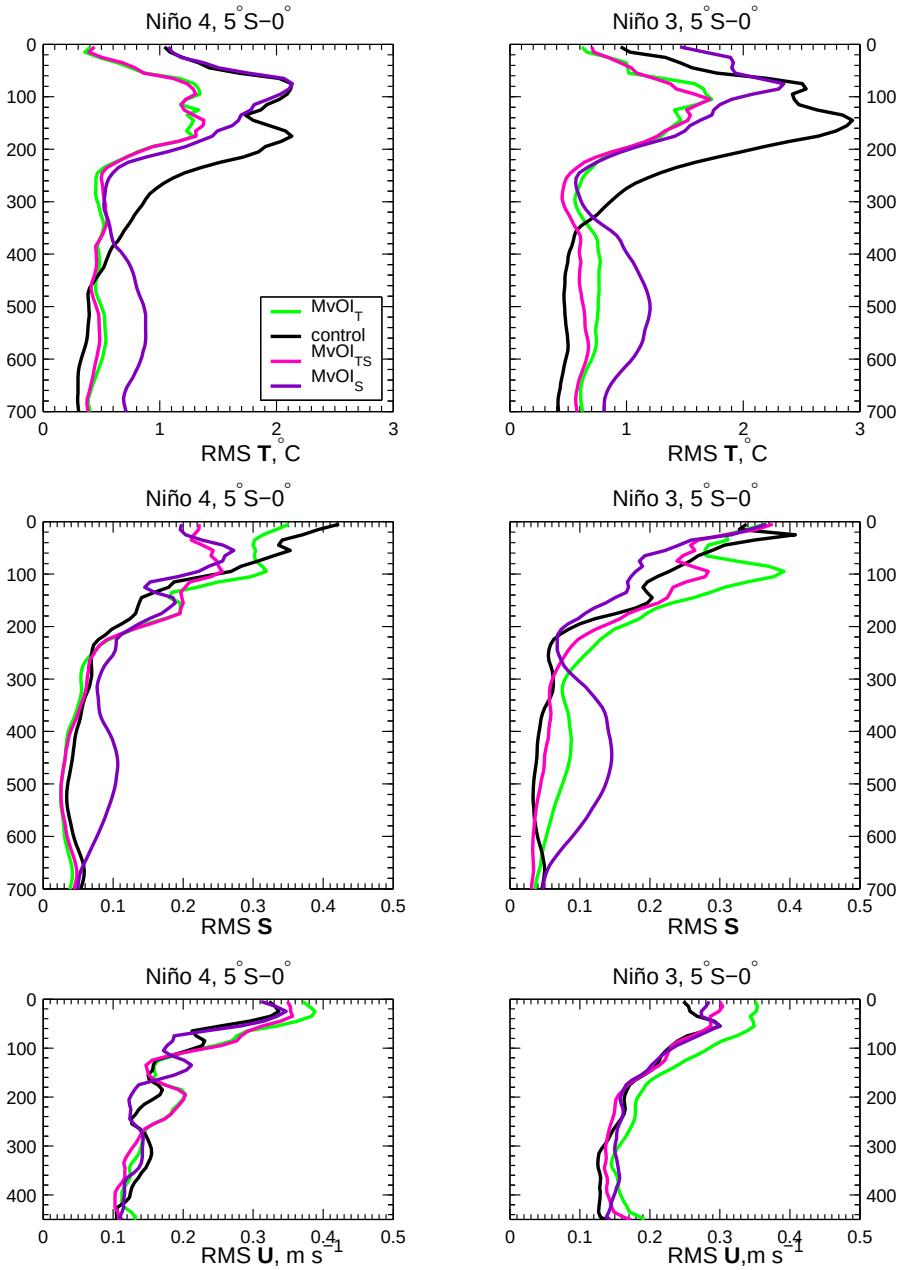

Figure 9.3: Rmsd between the four model runs (MvOI_T, MvOI_{TS}, MvOI_S and control) and the observations as a function of depth (m) for the 35 transects. Statistics are grouped by Niño 4 (160°E-150°W) and Niño 3 (150°W-90°W) regions, and each area is further divided into two halves, south and north of the equator (5°S-0° shown here).

Chapter 10

Conclusions

Two conceptually different forecast error covariance models and their variations were considered in the context of an optimal interpolation data assimilation. One is the univariate model of the temperature error which uses a Gaussian spatial covariance function with different scales in the zonal, meridional and vertical directions. The second is the multivariate error covariance estimated in the dominant error subspace of empirical orthogonal functions (EOFs) generated from Monte Carlo simulations. The latter provides an empirical estimate of the covariance of the errors in temperature, salinity and current fields and spatial structure consistent with the governing dynamics. Thus during an assimilation cycle not only the temperature field, but also the entire ocean state vector can be updated.

The univariate assimilation scheme brought the temperature field close to observations, yet the structure of the unobserved fields (salinity and currents) deteriorated quickly, precluding long-term integration. Most of the problems with the univariate OI analyses (no salty tongue in the south and deep penetration of salinity in the south, undercurrent that is too deep) are due to neglect of the correlation between temperature and salinity when assimilating temperature alone. The disruption of the density structure tends to cause spurious convective overturning.

This scheme can be improved by performing a salinity adjustment based on the temperature correction and the model's local temperature-salinity relationship. While improving the salinity structure, this method has limitations. It relies on the good representation of salinity by the model and is limited to temperature observations.

The multivariate scheme generally more successfully corrects the salinity and currents as verified by independent observations. The empirical error covariance model presented in this thesis is an initial estimate of the forecast error covariance, and is used throughout the assimilation under the assumption that the forecast error statistics do not change significantly in time or after prior

assimilation. The robustness of such an estimate was investigated and it was found that it does not exhibit significant seasonal or interannual variability, although there are not enough simulation years to distinguish among statistics during El Niño, La Niña and normal years.

A modification of the multivariate error covariance was considered to make it more computationally efficient. The leading empirical orthogonal functions were kept unchanged while those describing the small-scale noise-like variability were replaced by a simple functional model. Analyses from the modified scheme compared well with the full multivariate assimilation, although the accuracy of the analysis, as estimated from independent T, S and U data, varied across the equatorial waveguide and with variable. Thus the trade-off between efficiency and accuracy of assimilation has to be evaluated carefully for each application.

The empirical multivariate forecast error covariance model provides important information regarding the error statistics of all the model fields, prognostic or diagnostic. This gives a natural, consistent way to include observations of different types into the state estimation. Data of two different kinds, temperature and salinity, were assimilated simultaneously to demonstrate this unique capability of multivariate assimilation producing the best estimates of the ocean state.

The experience gained with the multivariate error covariance model underscores the importance of the procedure used to generate the ensemble of states from which the error is estimated. The spread of the ensemble should be assessed carefully to ensure that the ensemble variance has saturated. In further work, other sources of error in addition to the uncertainty in the forcing may be considered, such as the uncertainty in the model parameters. The future directions of research include assimilation of the real salinity data and developing the multivariate error covariance model for the global ocean model.

Appendix A

Temperature, salinity and zonal velocity Meridional profiles

Here sample meridional sections are displayed. These are included in the rmsd statistics shown in figures 5.1 and 5.2, figures 8.5 and 8.6, figures 9.2 and 9.3.

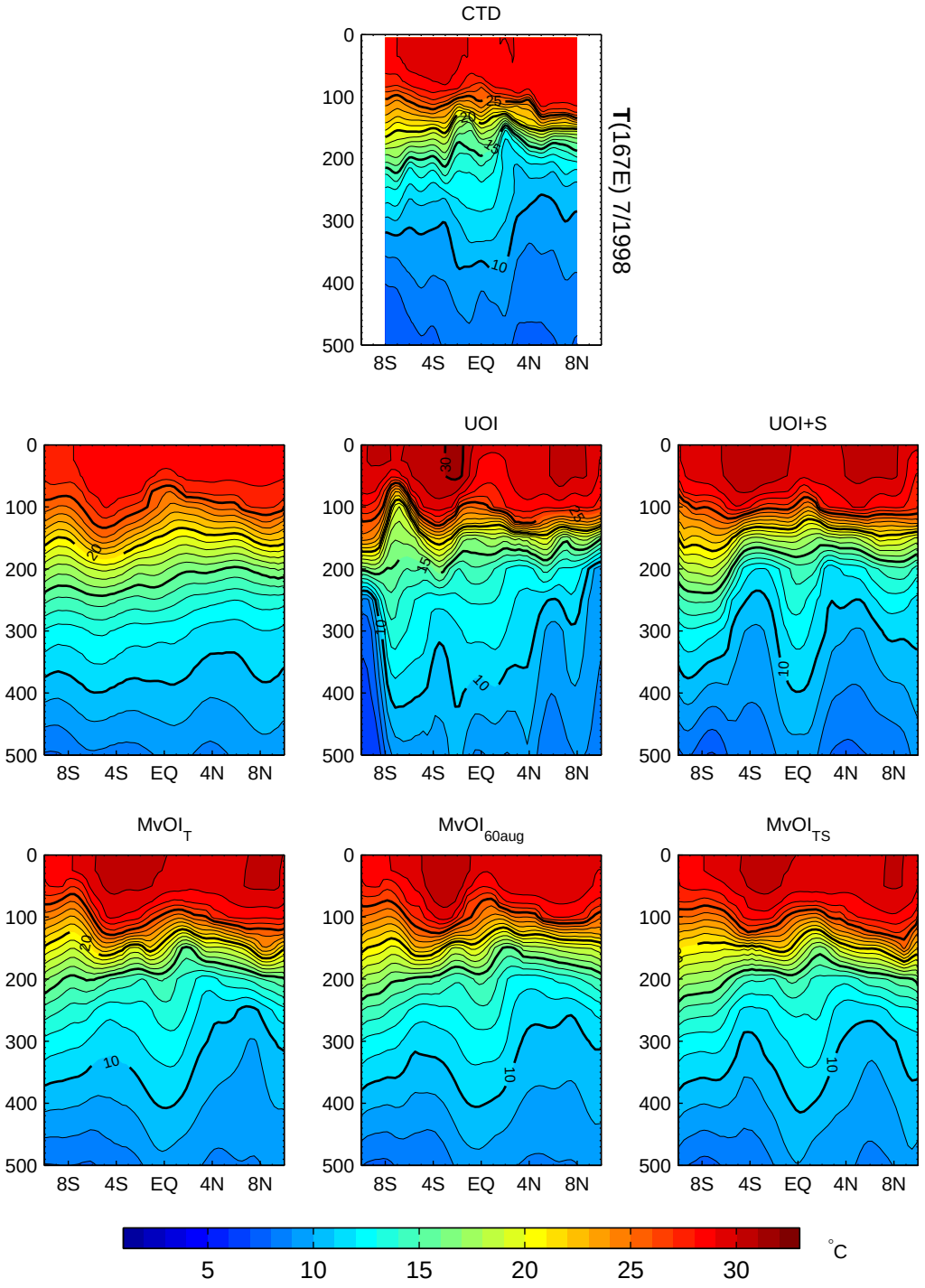

Figure A.1: Meridional vertical sections at 167°E of the model and observed temperature for July 1998. Model fields are averaged over one month, whereas the observations are from individual quasi-synoptic CTD/ADCP sections (following Johnson et al. 2000). Contour interval is 1°C.

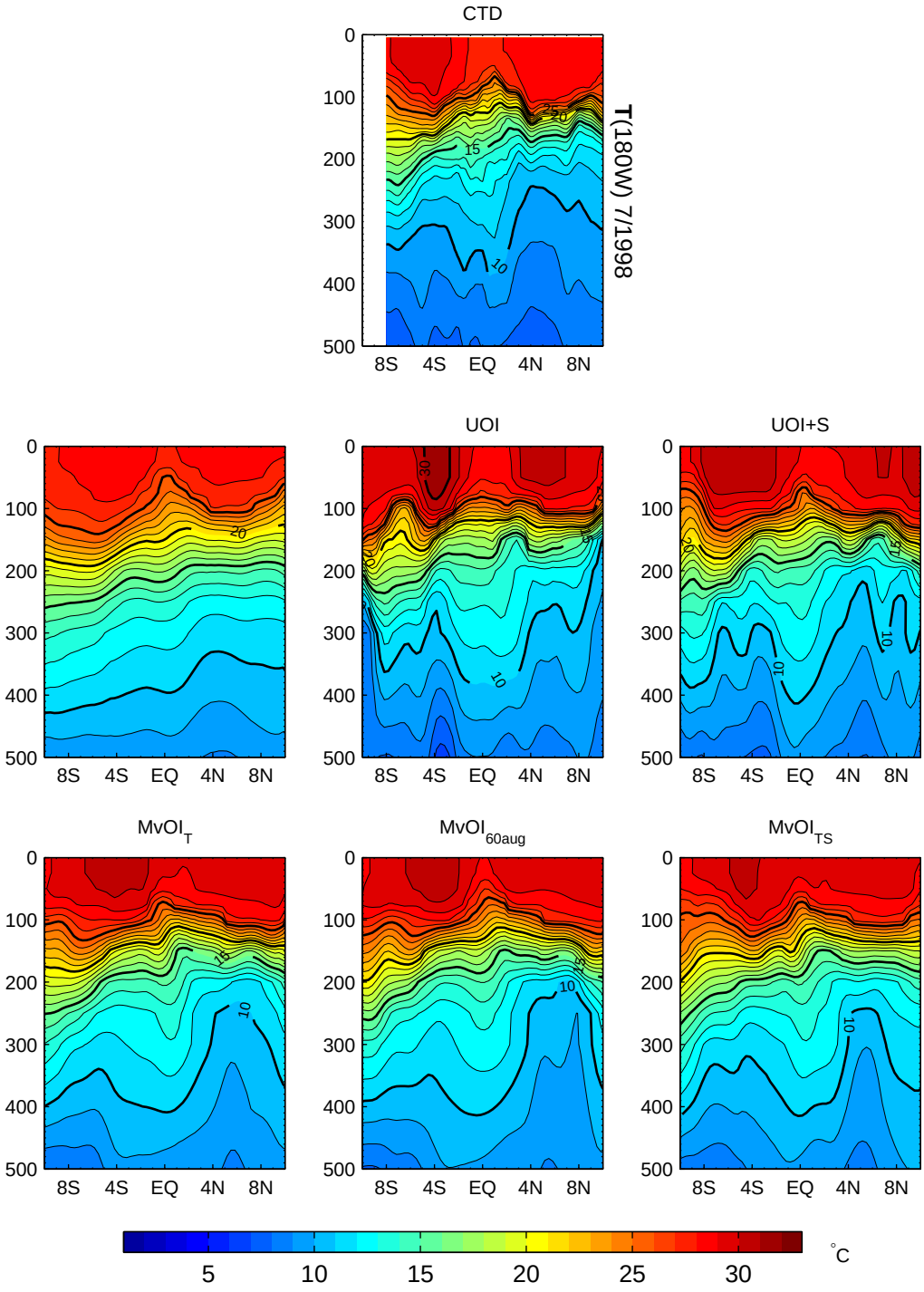

Figure A.2: Meridional vertical sections at 180°W of the model and observed temperature for July 1998. Model fields are averaged over one month, whereas the observations are from individual quasi-synoptic CTD/ADCP sections (following Johnson et al. 2000). Contour interval is 1°C.

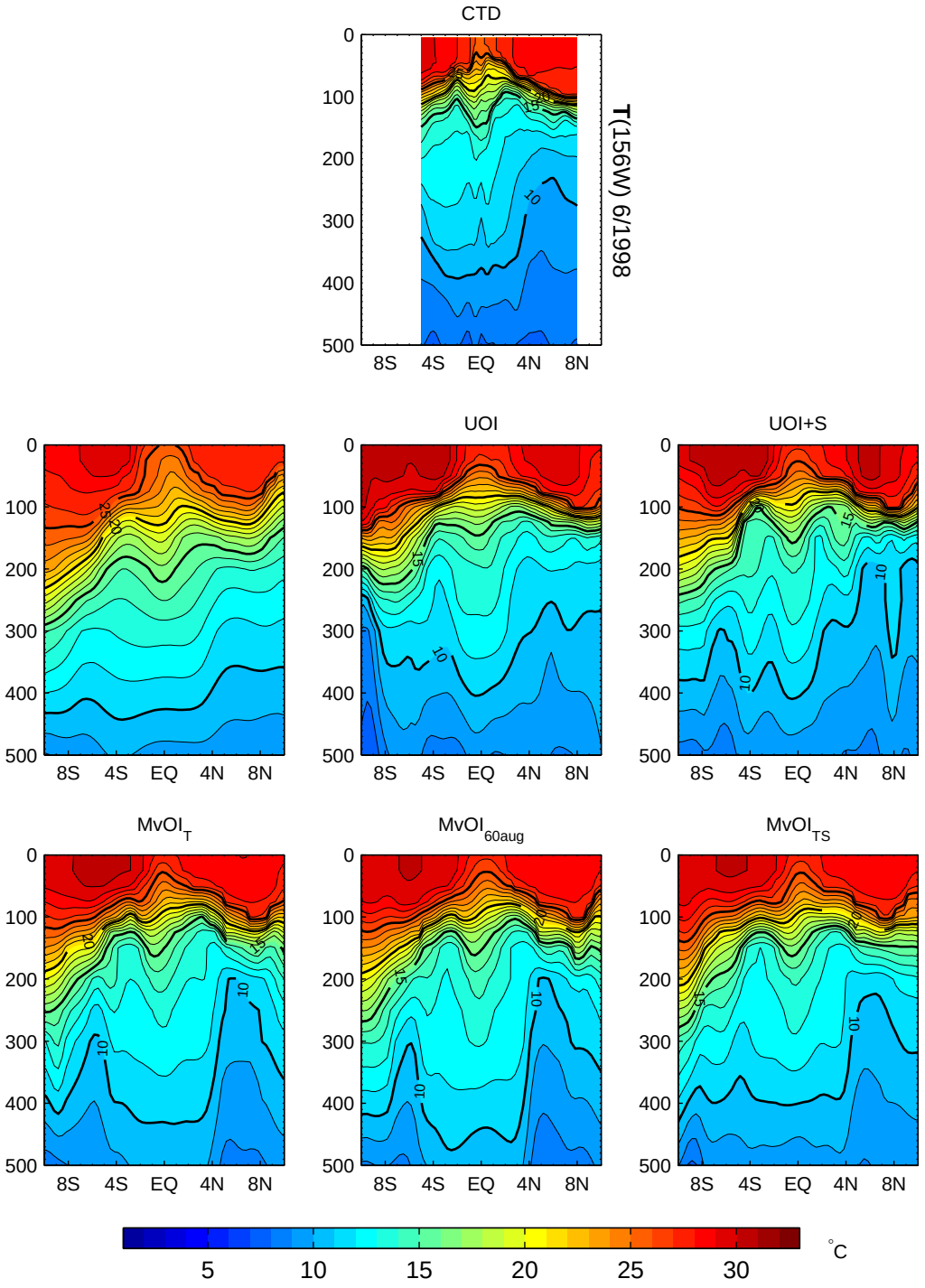

Figure A.3: Meridional vertical sections at 156°W of the model and observed temperature for June 1998. Model fields are averaged over one month, whereas the observations are from individual quasi-synoptic CTD/ADCP sections (following Johnson et al. 2000). Contour interval is 1°C.

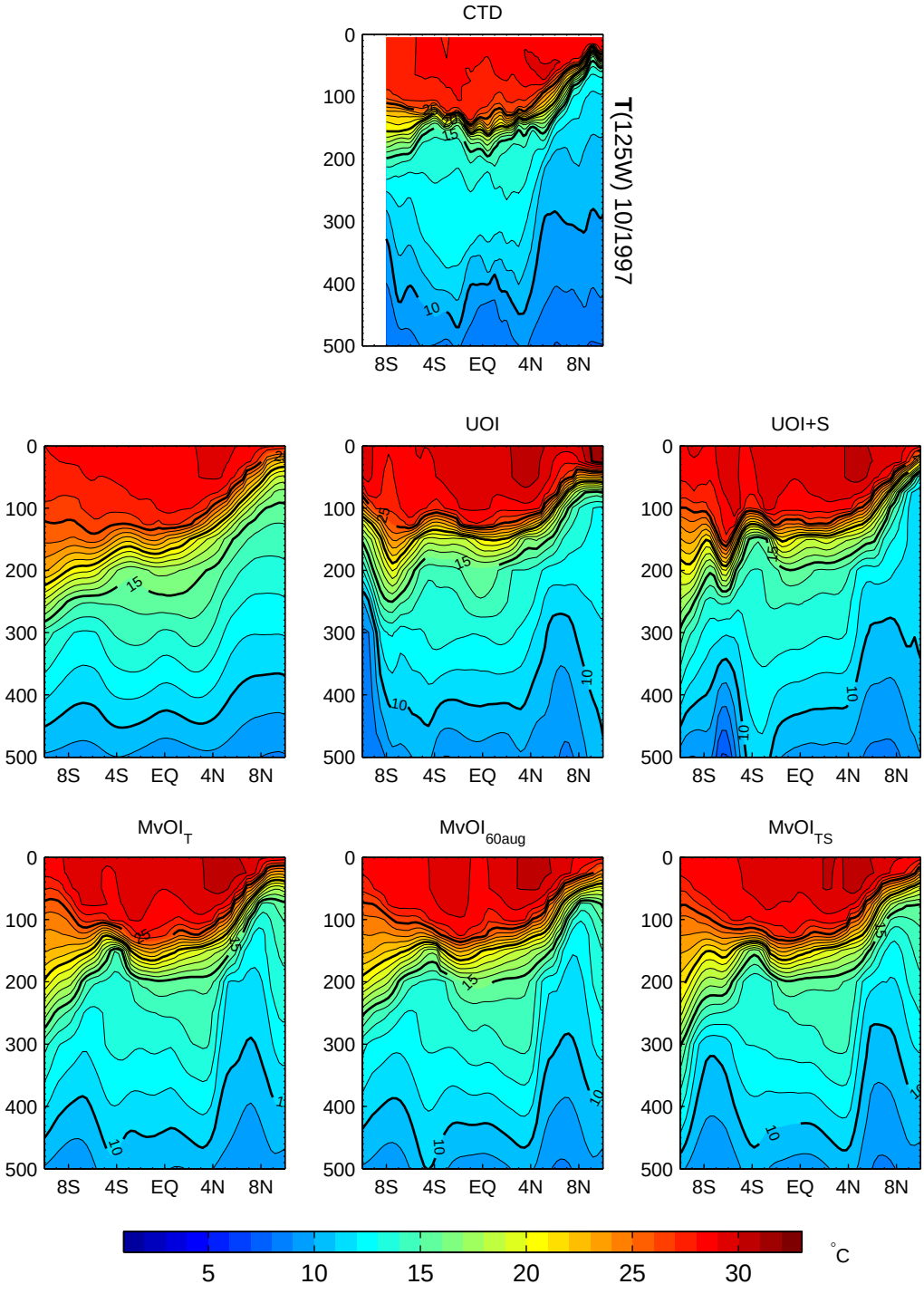

Figure A.4: Meridional vertical sections at 125°W of the model and observed temperature for October 1997. Model fields are averaged over one month, whereas the observations are from individual quasi-synoptic CTD/ADCP sections (following Johnson et al. 2000). Contour interval is 1°C.

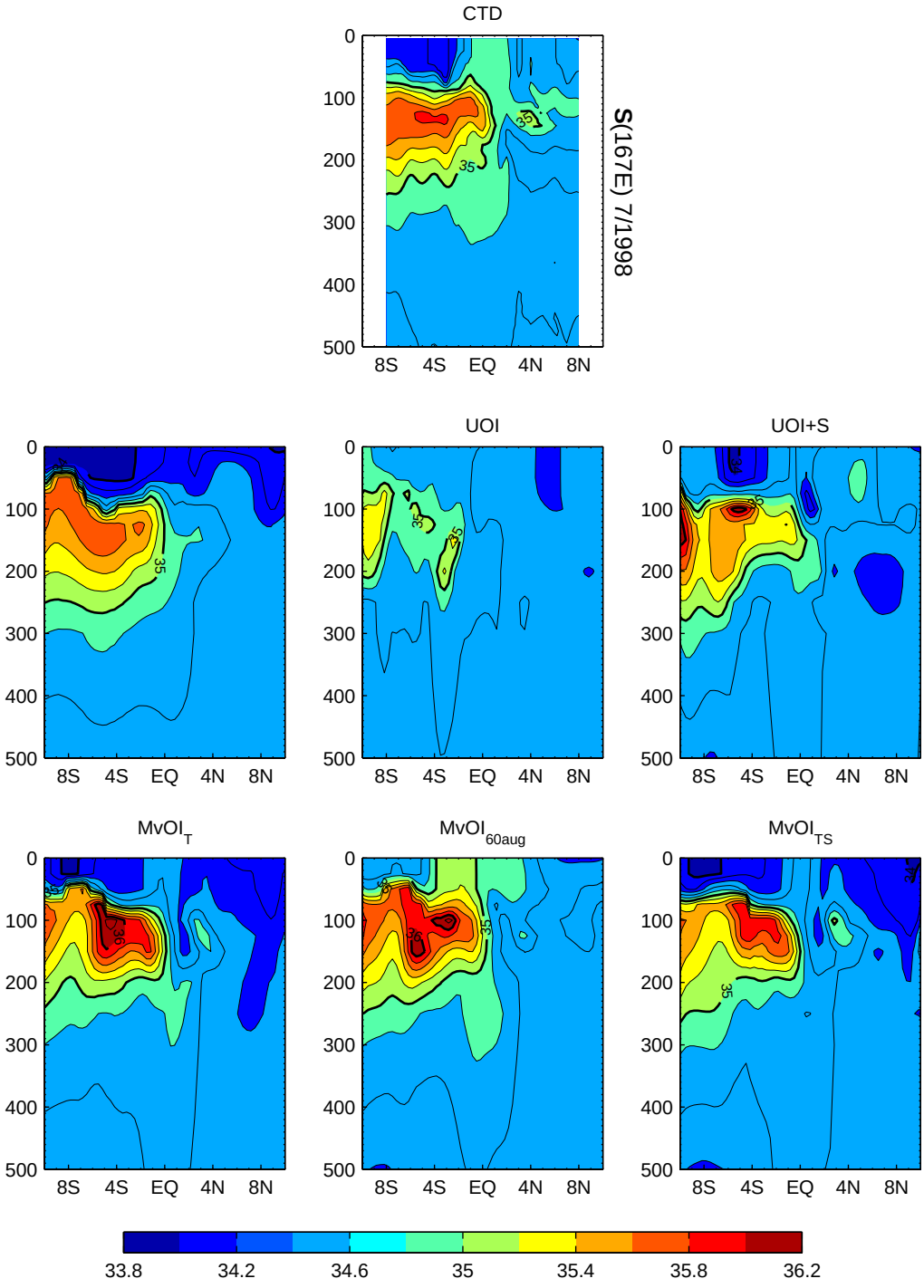

Figure A.5: Meridional vertical sections at 167°E of the model and observed salinity for July 1998. Model fields are averaged over one month, whereas the observations are from individual quasi-synoptic CTD/ADCP sections (following Johnson et al. 2000). Contour interval is 0.2.

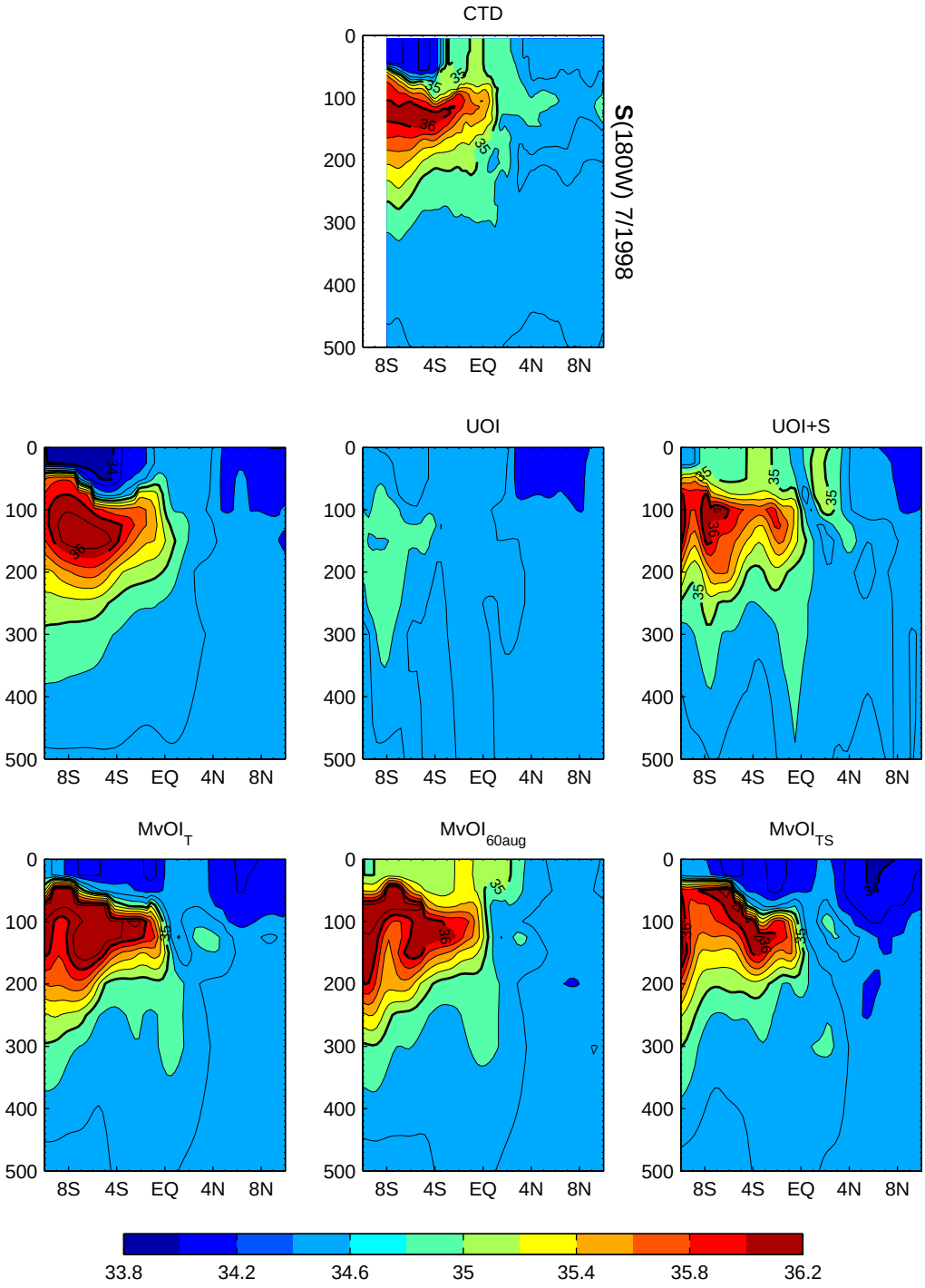

Figure A.6: Meridional vertical sections at 180°W of the model and observed salinity for July 1998. Model fields are averaged over one month, whereas the observations are from individual quasi-synoptic CTD/ADCP sections (following Johnson et al. 2000). Contour interval is 0.2.

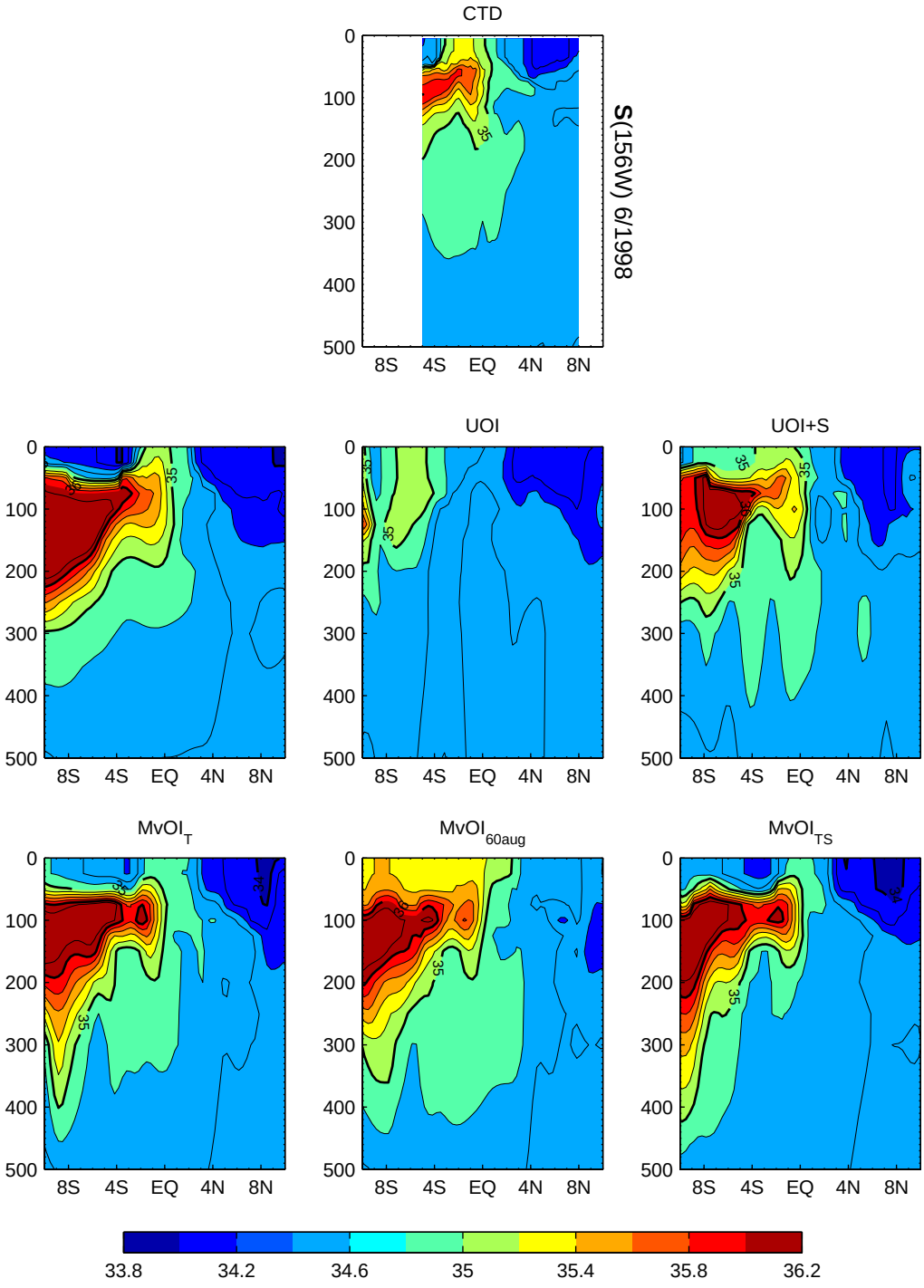

Figure A.7: Meridional vertical sections at 156°W of the model and observed salinity for June 1998. Model fields are averaged over one month, whereas the observations are from individual quasi-synoptic CTD/ADCP sections (following Johnson et al. 2000). Contour interval is 0.2.

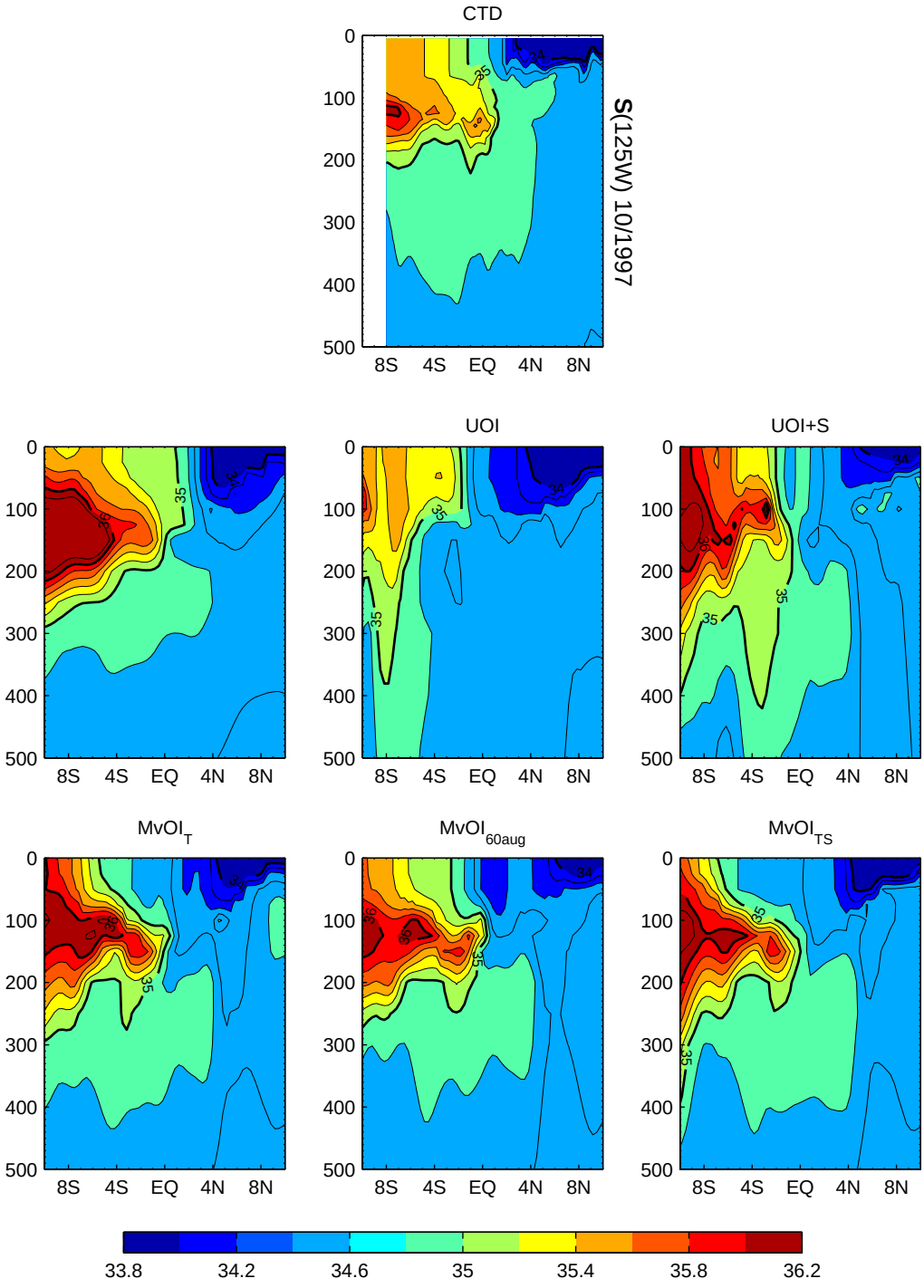

Figure A.8: Meridional vertical sections at 125°W of the model and observed salinity for October 1997. Model fields are averaged over one month, whereas the observations are from individual quasi-synoptic CTD/ADCP sections (following Johnson et al. 2000). Contour interval is 0.2.

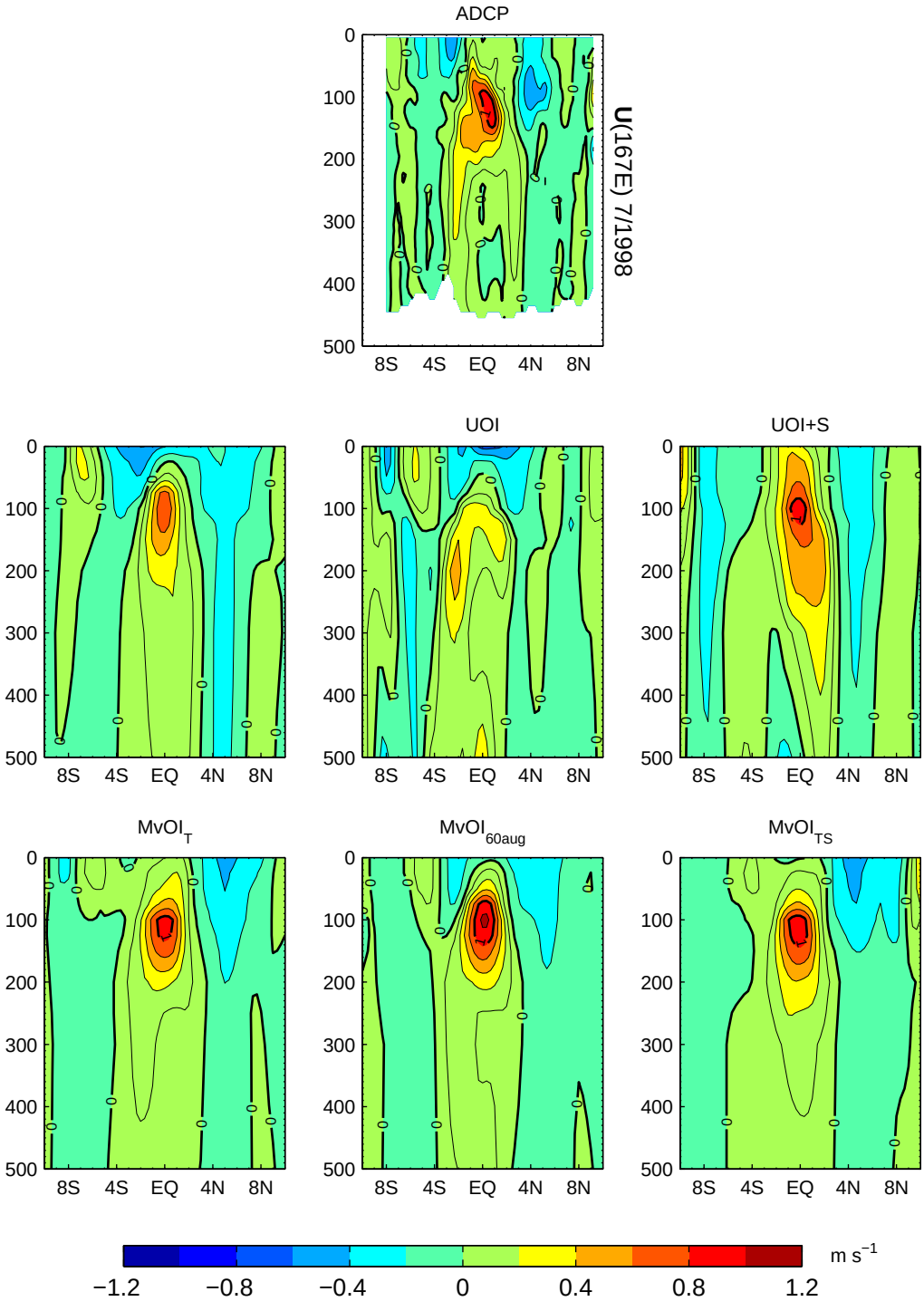

Figure A.9: Meridional vertical sections at 167°E of the model and observed zonal velocity for July 1998. Model fields are averaged over one month, whereas the observations are from individual quasi-synoptic CTD/ADCP sections (following Johnson et al. 2000). Contour interval is 0.2 ms^{-1}.

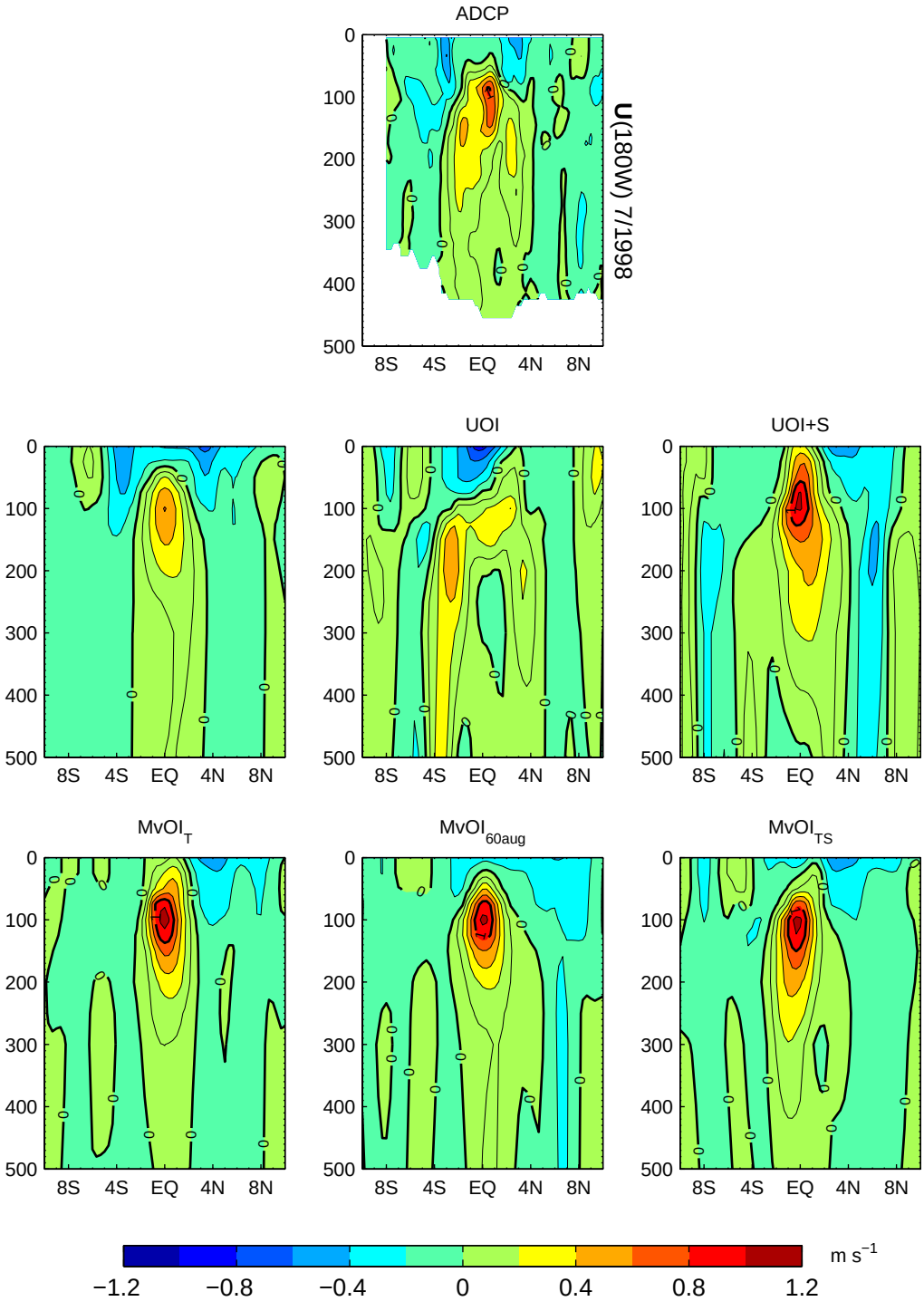

Figure A.10: Meridional vertical sections at 180°W of the model and observed zonal velocity for July 1998. Model fields are averaged over one month, whereas the observations are from individual quasi-synoptic CTD/ADCP sections (following Johnson et al. 2000). Contour interval is 0.2 ms^{-1}.

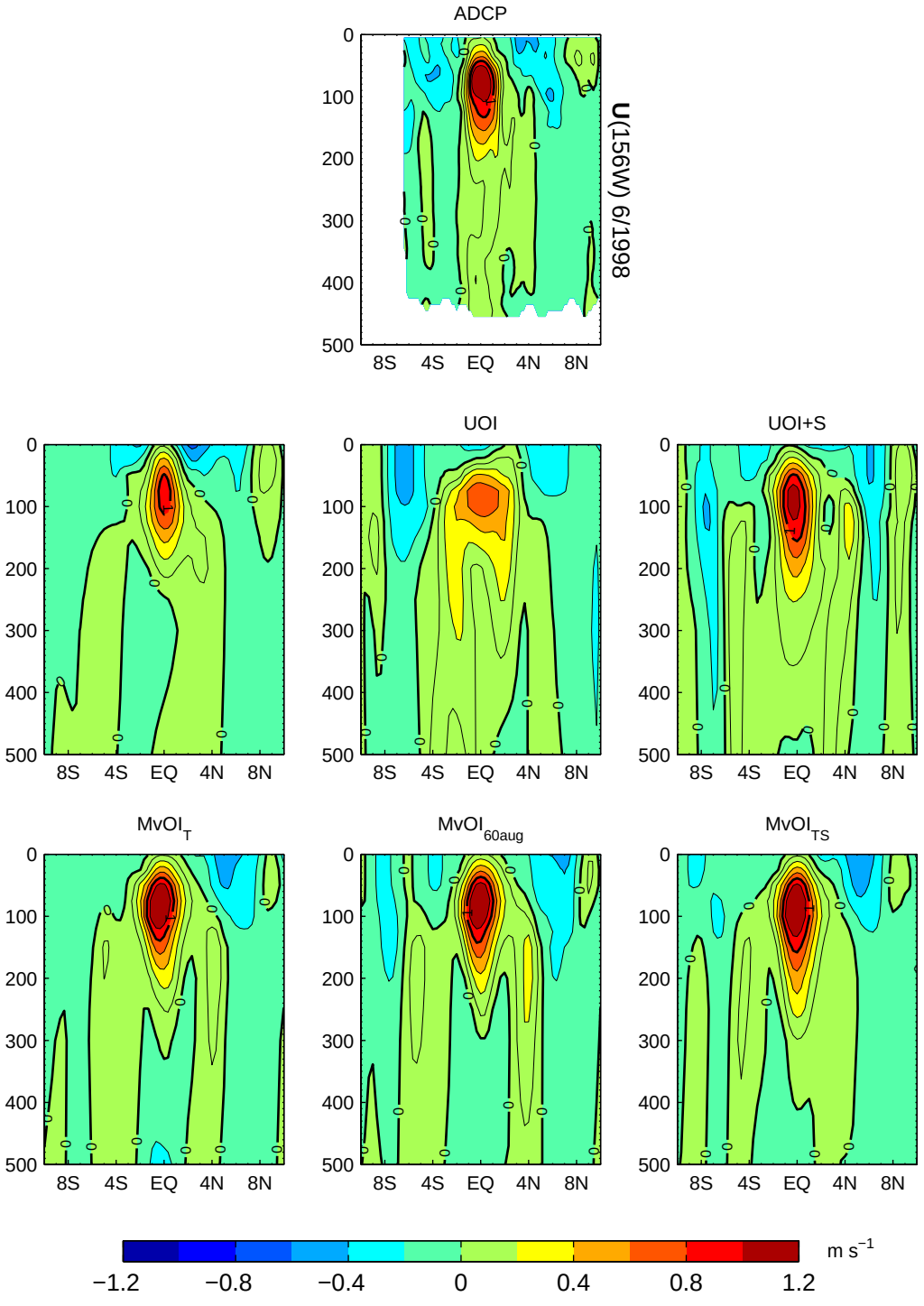

Figure A.11: Meridional vertical sections at 156°W of the model and observed zonal velocity for June 1998. Model fields are averaged over one month, whereas the observations are from individual quasi-synoptic CTD/ADCP sections (following Johnson et al. 2000). Contour interval is 0.2 ms^{-1}.

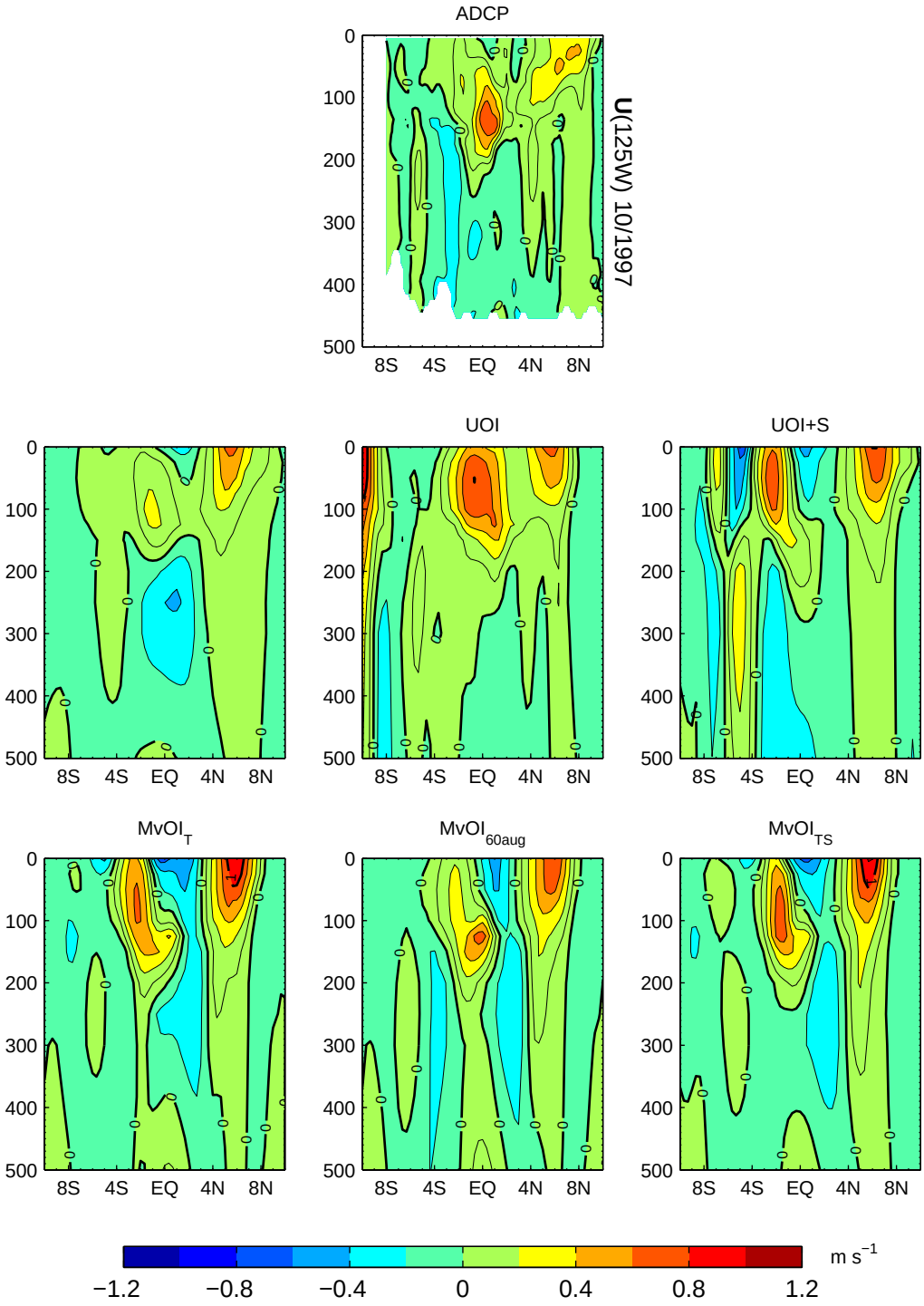

Figure A.12: Meridional vertical sections at 125°W of the model and observed zonal velocity for October 1997. Model fields are averaged over one month, whereas the observations are from individual quasi-synoptic CTD/ADCP sections (following Johnson et al. 2000). Contour interval is 0.2 ms^{-1}.

BIBLIOGRAPHY

[1] Atlas R., S. C. Bloom, R. N. Hoffman, J. V. Ardizzone, and G. Brin, 1991: Space-based surface wind vectors to aid understanding of air-sea interactions. *Eos, Transactions, Amer. Geophys. U.*, **72**, 201,204,205 and 208.

[2] Bloom S. C., L. L. Takacs, A. M. da Silva, and D. Ledvina, 1996: Data assimilation using incremental analysis updates. *Mon. Wea. Rev.*, **124**, 1256–1271.

[3] Borovikov A., M. M. Rienecker, and P. S. Schopf, 2001: Surface heat balance in the equatorial Pacific Ocean: Climatology and the warming event of 1994-95. *Journal of Climate*, **14**, 2624–2641.

[4] Buehner M., 2005: Ensemble-derived stationary and flow-dependent background error covariances: Evaluation in a quasi-operational NWP setting. Accepted for publication in *Q. J. R. Meteorol. Soc.*

[5] Burgers G., P. J. van Leeuwen, and G. Evensen, 1998: Analysis scheme in the Ensemble Kalman Filter. *Mon. Wea. Rev.*, **126**, 1719–1724.

[6] Cane M. A., A. Kaplan, R. N. Miller, B. Tang, E. C. Hackert, and A. J. Busalacchi, 1996: Mapping tropical Pacific sea level: Data assimilation via a reduced state Kalman filter. *J. of Geophys. Res.*, **101(C10)**, 22599–22617.

[7] Carton J. A. and E. C. Hackert, 1990: Data assimilation applied to the temperature and circulation in the tropical Atlantic, 1983-1984. *J. of Phys. Oceanogr.*, **20(8)**, 1150–1165.

[8] Cohn S. E., 1997: An introduction to estimation theory. *Journal of the Meteorological Society of Japan*, **75**, 257–288. Special issue dedicated to "Data Assimilation in Meteorology and Oceanography: Theory and Practice".

[9] Daley R., 1991: *Atmospheric Data Analysis*. Cambridge University Press, 457 pp.

[10] Derber J. C., D. F. Parrish, and S. J. Lord, 1991: The new global operational analysis system at the National Meteorological Center. *Wea. and Forecast*, **6**, 538–547.

[11] Evensen G., 1994: Sequential data assimilation with a nonlinear quasi-geostrophic model using Monte Carlo methods to forecast error statistics. *J. Geophys. Res.*, **C99**, 10143–10162.

[12] Fisher M., and E. Andersson, 2001: Developments in 4D-Var and Kalman filtering. Technical Memorandum 347, ECMWF, 36 pp.

[13] Freitag H. P., Y. Feng, L. J. Mangum, M. P. McPhaden, J. Neander, and L. D. Stratton, 1994: Calibration procedures and instrumental accuracy estimates of TAO temperature, relative humidity and radiation measurements. ERL PMEL-104, NOAA.

[14] Fukumori I., J. Benveniste, C. Wunch, and D. B. Haidvogel, 1993: Assimilation of sea surface topography into an ocean circulation model using a steady-state smoother. *J. of Phys. Oceanography*, **23**, 1831–1855.

[15] Gaspari G., and S. E. Cohn, 1999: Contruction of correlation functions in two and three dimensions. *Quart. J. Roy. Meteorol. Soc.*, **125**, 723–757.

[16] Ghil M., and P. Malanotte-Rizzoli, 1991: Data assimilation in meteorology and oceanography. *Advances in Geophysics*, **33**, 141–266.

[17] Golub G. H., C. F. Van Loan, 1996: *Matrix computation.* The Johns Hopkins University Press, 694 pp.

[18] Harrison D. E., E. F. P. Minnis, B. Barkstrom, and G. Gibson, 1993: Radiation budget at the top of the atmosphere. *Atlas of Satellite Observations Related to Global Change,* R. J. Gurney, J. L. Foster, and C. L. Parkinson, Eds., Cambridge University Press, 19–38.

[19] Houtekamer P. L., L. Lefaivre, J. Derome, H. Ritchie, and H. L. Mitchell, 1996: A system simulation approach to ensemble prediction. *Mon. Wea. Rev.*, **124**, 1225–1242.

[20] _____, and H. Mitchell, 1998: Data assimilation using an ensemble Kalman filter technique. *Mon. Wea. Rev.*, **126**, 796–811.

[21] _____, and H. Mitchell, 2001: A sequential ensemble Kalman filter for atmospheric data assimilation. *Mon. Wea. Rev.*, **129**, 123–137.

[22] Ji M., A. Leetmaa, and J. Derber, 1995: An ocean analysis system for seasonal to interannual climate studies. *Mon. Wea. Rev.*, **123**, 460–481.

[23] Johnson G. C., M. J. McPhaden, G. D. Rowe, and K. E. McTaggart, 2000: Upper equatorial Pacific Ocean current and salinity variability during the 1996-1998 El Niño-La Niña cycle. *J. of Geophys. Res.*, **105**, 1037–1053.

[24] _____, B. M. Sloyan, W. S. Kessler, and K. E. McTaggart, 2002: Direct measurements of upper ocean currents and water properties across the tropical Pacific during the 1990s. *Progress in Oceanography*, **52**, 31–61.

[25] Kalman R., 1960: A new approach to linear filtering and prediction problems. *J. Basic Eng.*, **D82**, 35–45.

[26] Kalnay E., and coauthors, 1996: The NCEP/NCAR 40-year reanalysis project. *Bulletin of the Amer. Meteorol. Soc.*, **77**, 437–471.

[27] Kaplan A., Y. Kushnir, M. A. Cane, and M. B. Blumenthal, 1997: Reduced space optimal analysis for historical data sets: 136 years of Atlantic sea surface temperature. *J. of Geophys. Res.*, **102**, 27835–27860.

[28] Keppenne C. L., and M. M. Rienecker, 2002: Initial testing of a massively parallel ensemble Kalman filter with the Poseidon isopycnal ocean general circulation model. *Mon. Wea. Rev.*, **130**, 2951–2965.

[29] _____, and M. M. Rienecker, 2003: Assimilation of temperature into an isopycnal ocean general circulation model using a parallel Ensemble Kalman Filter. *J. Mar. Sys.*, **40-41**, 363–380.

[30] Kraus E. B., and J. S. Turner, 1967: A one-dimensional model of the seasonal thermocline: II. The general theory and its consequences. *Tellus*, **19**, 98–109.

[31] Large W. G., and S. Pond, 1982: Open ocean momentum flux measurements in moderate to strong winds. *J. Phys. Oceanogr.*, **11**, 324–336.

[32] Levitus S., and T. P. Boyer, 1994: Temperature. Vol. 4, *World Ocean Atlas 1994*, NOAA Atlas NESDIS, 117 pp.

[33] Lorenc A. C., 1986: Analysis methods for numerical weather prediction. *Quart. J. R. Met. Soc.*, **112**, 1177–1194.

[34] McPhaden M. J., and coauthors, 1998: The tropical ocean global atmosphere observing system: A decade of progress. *J. of Geophys. Res.*, **103**, 14169–14240.

[35] Oke P. R., J. S. Allen, R. N. Miller, G. D. Egbert, and P. M. Kosro, 2002: Assimilation of surface velocity data into a primitive equation coastal ocean model. *J. of Gephys . Res.*, **107(C9)**, 5–1–5–25.

[36] Pacanowski R. and S. G. H. Philander, 1981: Parametrization of vertical mixing in numerical models of tropical oceans. *J. Phys. Oceanogr.*, **11**, 1443–1451.

[37] Philander S. G , 1990: *El Niño, La Niña, and the Southern Oscillation.* Academic Press, 239 pp.

[38] Preisendorfer R. W., 1988: *Principal component analysis in meteorology and oceanography.* Elsevier, 425 pp.

[39] Rienecker M. M., and R. N. Miller, 1991: Ocean data assimilation using optimal interpolation with a quasi-geostrophic model. *Journal of Geophysical Research*, **96(C8)**, 15093–15103.

[40] Rosati A., R. Gudgel, and K. Miyakoda, 1996: Global ocean data assimilation system. *Modern Approaches to Data Assimilation in Ocean Modeling*, Elsevier, 181-203.

[41] _____, K. Miyakoda, and R. Gudgel, 1997: The impact of ocean initial conditions on ENSO forecasting with a coupled model. *Mon. Wea. Rev.*, **125**, 754–772.

[42] Rossow W. B., and R. A. Schiffer, 1991: ISCCP cloud data products. *Bull. Am. Met. Soc.*, **72**, 2–20.

[43] Schopf P. S., and A. Loughe, 1995: A reduced-gravity isopycnal ocean model - hindcasts of El Niño. *Mon. Wea. Rev.*, **123**, 2839–2863.

[44] Seager R., M. B. Blumenthal, and Y. Kushnir, 1994: An advective atmospheric mixed layer model for ocean modeling purposes: Global simulation of surface heat fluxes. *J. Clim.*, **8**, 1951–1964.

[45] Shapiro R., 1970: Smoothing, filtering and boundary effects. *Rev. of Geophys. Space Phys.*, **8**, 359–387.

[46] Suarez M. J., and L. L. Takacs, 1995: Documentation of the Aries/GEOS dynamical core Version 2. Technical memorandum 104606, **5**, NASA, 44 pp.

[47] Troccoli A., and K. Haines, 1999: Use of the temperature-salinity relation in a data assimilation context. *J. Atmos. Oceanic Technol.*, **16**, 2011–2025.

[48] _____, M. A. Balmaseda, J. Segschneider, J. Vialard, D. L. T. Anderson, K. Heines, T. Stockdale, F. Vitart, and A. D. Fox, 2002: Salinity adjustments in the presence of temperature data assimilation. *Mon. Wea. Rev.*, **130**, 89–102.

[49] _____, M. M. Rienecker, C. L. Keppenne, and G. C. Johnson, 2003: Temperature data assimilation with salinity corrections: Validation in the tropical Pacific Ocean, 1993-1998. Technical Report 104606, **24**, NASA GSFC, 23 pp.

[50] Wilson S., 2000: Launching the Argo armada. *Oceanus*, **42**, 17–19.

[51] Xie P. P., and P. Arkin, 1997: Global precipitation: A 17-year monthly analysis based on gauge observations, satellite estimates, and numerical model outputs. *Bull. Amer. Meteorol. Soc.*, **11**, 2539–2558.

[52] Yang S., K.-M. Lau, and P. S. Schopf, 1999: Sensitivity of the tropical Pacific Ocean to precipitation-induced freshwater flux. *Climate Dynamics*, **15**, 737–750.

[53] Zhang S., and J. L. Anderson, 2003: Impact of spatially and temporally varying estimates of error covariance on assimilation in a simple atmospheric model. *Tellus*, **55A**, 126–147.